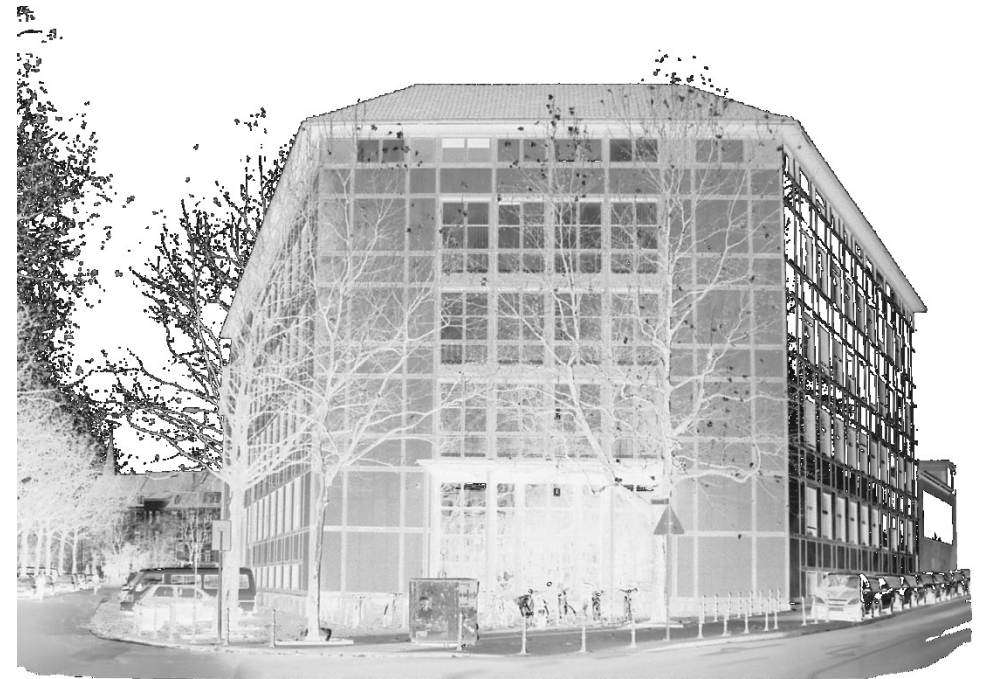


A cost-efficient process route for the mass production of thin-walled structural aluminum body castings

Mohamed Youssef Ahmed Youssef



978-3-944601-17-5 (E-Book)

Band 28



RWTHAACHEN
UNIVERSITY

Ergebnisse aus Forschung und
Entwicklung
Herausgeber:
Prof. Dr.-Ing. A. Bührig-Polaczek

„A cost-efficient process route for the mass production of thin-walled structural aluminium body castings “

Von der Fakultät für Georessourcen und Materialtechnik der
Rheinisch -Westfälischen Technischen Hochschule Aachen

zur Erlangung des akademischen Grades eines

Doktors der Ingenieurwissenschaften

genehmigte Dissertation

vorgelegt von

Mohamed Youssef Ahmed Youssef, M.Sc.

aus Kairo, Ägypten

Berichter: Herr Univ.-Prof. Dr.-Ing. Andreas Bührig-Polaczek
Herr Univ.-Prof. Dr.-Ing. Gerhard Hirt

Tag der mündlichen Prüfung: 25.03.2021

Diese Dissertation ist auf den Internetseiten der Universitätsbibliothek online verfügbar

Titel: *A cost-efficient process route for the mass production of thin-walled structural aluminium body castings*

Autor: Mohamed Youssef Ahmed Youssef

Reihe: Ergebnisse aus Forschung und Entwicklung, Band 28 (2021)

Gießerei-Institut der RWTH Aachen
Intzestr. 5

D-52072 Aachen

Tel.: +49 (0)241 8095880

Fax.: +49 (0)241 8092276

E-Mail: sekretariat@gi.rwth-aachen.de

<http://www.gi.rwth-aachen.de>

ISBN: 978-3-944601-17-5 (E-Book)

Volltext verfügbar: 10.18154/RWTH-2021-03555



Dieses Werk bzw. Inhalt steht unter einer Creative Commons Namensnennung-Keine Bearbeitung 3.0 Unported Lizenz ([Creative Commons Attribution-NonCommercial 3.0 Unported License](https://creativecommons.org/licenses/by-nc/3.0/))

D82 (Diss. RWTH Aachen University, 2021)

Publikationsserver
Universitätsbibliothek
RWTH Aachen University
Templergraben 61
52062 Aachen
www.ub.rwth-aachen.de



Acknowledgments

The presented work in this thesis was done during my appointment as a Research Engineer at *Ford Werke GmbH*. The partner in this work was the *Foundry Institute (GI) of the RWTH Aachen University*.

I would first love to thank Univ.-Prof. Dr.-Ing. Andreas Bührig-Polaczek for making this thesis possible, for his enormous support, for his outstanding supervision and for his constructive feedbacks that I always learned from. I would also like to thank him for allowing the use of the *Foundry Institute (GI)* facilities throughout the duration of this thesis. In addition, I would like to thank Univ.-Prof. Dr.-Ing. Gerhard Hirt for his interest in supervising this thesis and for his remarks.

I am also very grateful to my colleagues at *Ford Research and innovation center in Aachen*, especially Dr.-Ing. Maik Broda, Dipl.-Ing. Matthias Warkentin and Dr.-Ing. Ulrich Weiss. I would love to thank them and the rest of the team, which includes Dr.-Ing. Clemens Verpoort, Dipl.-Ing. Michael Ölcher, M.Sc. Pascal Rebmann, Dipl.-Ing. Aleksandar Bach, M.Sc. Marcus Schopen, M.Sc. Ilya Popov, M.Sc. Ferat Özkan, Dr.-Ing. Niels Pasligh, Dr.-Ing. Omar Ghouati, M.Sc. Raphael Koch and M.Sc. Lars Bognar, for their continuous motivation and remarkable support.

I am also very thankful to Dipl.-Ing. Jochen Schenk and the rest of the team at Ford Werke GmbH's Central lab in Cologne for their support and for facilitating the use of the material testing facilities.

Lastly, I would love to thank my family, especially my parents and sister, and my friends for always motivating me to reach my goals and for providing the right atmosphere for me to excel.

Table of Contents

Table of Contents

0	Short version	i
0.1	Cost calculation study.....	i
0.2	Defining the suitable test alloys.....	ii
0.3	The production of the plates and the parts.....	iii
0.4	The evaluation criteria.....	vi
0.5	The high pressure die casting trials.....	viii
0.6	The RheoMetal™ casting trials.....	xi
1	Introduction and motivation	1
1.1	Background information.....	1
1.2	Aim of the thesis.....	3
1.3	Research approach.....	3
2	Theoretical background and state of the art	4
2.1	Automotive Casting parts.....	4
2.2	Casting methods.....	5
2.3	High pressure die casting.....	6
2.3.1	The process flow.....	6
2.3.2	The influence of the process parameters.....	9
2.3.3	The influence of the casting part's wall thickness.....	11
2.3.4	The typical defects.....	11
2.4	Semi-solid casting.....	14
2.4.1	Thixocasting.....	16
2.4.2	Rheocasting.....	18
2.4.3	The RheoMetal™ process.....	20
2.5	The aluminium alloys for structural automotive castings.....	28
2.6	Heat treatments.....	31
3	Cost calculation study	32
3.1	Cost estimation of the parts produced using the HPDC process.....	32
3.2	Cost estimation for the parts produced using the RheoMetal™ process.....	46
4	Experimental approach	49
4.1	Defining the suitable test alloys.....	50
4.2	The production of the test plates using the HPDC process.....	52

Table of Contents

4.3	The production of the test plates using the RheoMetal™ process.....	55
4.4	The production of the parts.....	59
4.4.1	New alloy for an enhanced feeding efficiency and rheocastability.....	61
4.5	The characterization of the material properties and the process parameters	66
4.5.1	Uniaxial tensile test	66
4.5.2	3-point bending test	70
4.5.3	Density measurement	72
4.5.4	Self-piercing riveting.....	74
4.5.5	Evaluation of the results	78
4.5.6	Microstructural analysis	78
4.5.7	SEM-EDS Analysis	79
4.5.8	Optical Emission spectroscopy.....	80
4.6	Guidelines for testing.....	80
4.6.1	The best location within the plates	81
4.6.2	The symmetry of the plates	82
4.6.3	The relevant tensile test sample.....	83
4.6.4	The suitable orientation of the samples.....	84
4.6.5	The consistency of the casting process.....	86
5	The investigations regarding the high pressure die casting process.....	88
5.1	The optimum HPDC process parameters.....	89
5.1.1	The optimum HPDC process parameters to produce the plates at supplier 1	89
5.1.2	The optimum HPDC process parameters to produce the parts at supplier 3	94
5.2	Characterization of the different HPDC alloys and alloy-heat treatment combinations.....	95
5.2.1	Characterization of the HPDC alloys and alloy-heat treatment combinations that were used at the suppliers 1 and 2.....	96
5.2.2	Characterization of the HPDC alloys that were used at supplier 3	103
5.3	The impacts of the HPDC alloys and alloy-heat treatment combinations on the crash resistance potential of the casting	106
5.3.1	The impacts of the HPDC alloys and alloy-heat treatment combinations on the crash resistance potentials of the plates from the suppliers 1 and 2.....	107
5.3.2	The impacts of the HPDC alloys on the crash resistance potentials of the parts from supplier 3	112
5.4	The rivetability of the HPDC alloys and alloy-heat treatment combinations.....	113

Table of Contents

5.4.1	The rivetability of the HPDC alloys and alloy-heat treatment combinations that were utilized at the suppliers 1 and 2	114
5.4.2	The rivetability of the HPDC alloys that were utilized at supplier 3	118
6	The investigations regarding the RheoMetal™ process	120
6.1	The optimum RheoMetal™ process parameters	121
6.1.1	The optimum RheoMetal™ process parameters to produce the plates at supplier 1	121
6.1.2	The optimum RheoMetal™ process parameters to produce the parts at supplier 3	129
6.2	Characterization of the different RheoMetal™ alloys	129
6.2.1	Characterization of the RheoMetal™ alloys that were used at supplier 1	130
6.2.2	Characterization of the RheoMetal™ alloys that were used at supplier 3	134
6.3	The impacts of the RheoMetal™ alloys on the crash resistance potential of the casting	137
6.3.1	The impacts of the RheoMetal™ alloys on the crash resistance potential of the plates from supplier 1	138
6.3.2	The impacts of the RheoMetal™ alloys on the crash resistance potential of the parts from supplier 3	139
6.4	The rivetability of the RheoMetal™ alloys	141
6.4.1	The rivetability of the RheoMetal™ alloys that were used at supplier 1	142
6.4.2	The rivetability of the RheoMetal™ alloys that were used at supplier 3	144
6.5	The optimization potential of the testing outcomes from the RheoMetal™ process trials at supplier 3	145
6.5.1	The optimum melt superheat	146
6.5.2	The optimum %EEM	147
6.5.3	The optimum rotation speed of the EEM	148
7	Discussion and conclusion	150
7.1	The HPDC trials	150
7.1.1	The correlation between the different outcomes	152
7.2	The RheoMetal™ casting trials	157
7.2.1	The correlation between the different outcomes	159
7.3	The comparison between the outcomes of the HPDC and the RheoMetal™ casting trials	160
7.4	Conclusion	161
8	Summary and outlook	163

Table of Contents

8.1	Summary.....	163
8.2	Outlook	164
9	List of symbols	166
10	References	167
11	Curriculum Vitae.....	175
12	Patent applications	176

0 Short version

In order to meet the continuous demand for lower CO₂ emissions, several approaches have been and still are extensively researched. One of the adopted approaches by the automotive sector, which aims towards an improved fuel efficiency, is the reduction in the weight of the vehicles by replacing their heavy steel sheets with lighter and more functionally integrated aluminium castings. Implementing this approach for the mass production of thin walled structural body castings can be, however, less economical due to its impact on raising the parts' costs, mainly due to the use of the more expensive raw materials (aluminium alloys). Therefore, within this thesis, it was considered important to investigate the possible means for executing this proposition in a cost-efficient way. For this purpose, a cost calculation study was initially implemented to determine the main cost drivers for the production of a 2020 Ford explorer shock tower. This was followed by an extensive investigation to the findings of this study.

0.1 Cost calculation study

As mentioned in the previous section, a cost calculation study was conducted to test the influence of several factors on the cost of the 2020 Ford explorer shock tower. The considered factors and their respective levels are represented in *Table 0.1* as follows.

Table 0.1: The investigated factors in the cost calculation study and their respective levels.

Factor	levels
(a) The type of the high pressure die casting machine	Single tool
	Double tool
(b) The alloy and, if any, the needed heat treatment process to reach the desired mechanical properties of the casting	AlSi10MnMg-T7
	AlSi9MnMoZr
(c) The application of the vacuum condition	Applied
	Not applied
(d) The die life	80000 shots
	100000 shots
	130000 shots
(e) The casting process	High pressure die casting (HPDC)
	RheoMetal™

As seen in *Table 0.1*, a minimum of two levels were chosen to test the impact of each of the considered factors on the overall cost of the cast part.

By combining the different levels that belong to the factors (a)-(d) in *Table 0.1*, 24 different shock tower's production scenarios by the HPDC process were made. A cost analysis was then conducted for each scenario using a calculation tool, which have been upgraded and enhanced

0. Short version

after being obtained from the company *Bühler AG*. The influence of each factor on the cost was then determined after comparing between the cost analysis' outcomes of the relevant scenarios. The main finding of this study was that the heat treatment has the greatest impact on the cost of the structural body part. Therefore, choosing an alloy that can fulfill its mechanical and joining requirements in the as-cast state would lead to a high cost efficiency.

Unlike the other factors, the influence of the casting process, factor (*e*) in *Table 0.1*, on the cost was determined after comparing between a single RheoMetal™ process' scenario and a reference HPDC scenario. This comparison had revealed that, based on the considered process variables, the RheoMetal™ process would lead to a higher cost reduction than the HPDC process, mainly due to its positive impact on the die life.

0.2 Defining the suitable test alloys

As the choice of the alloy had the largest impact on the cost of the cast part, it was important to define the alloys that can be investigated during the scope of this thesis. The purpose of this step was to determine the most suitable alloy that can meet the mechanical and joining requirements of the considered structural body casting, in this case the 2020 Ford explorer shock tower, without the need for a further heat treatment process.

In addition, due to the influence of the casting process on the cost of the cast part, the suitability of the defined alloys to the casting process was, as shown in *Table 0.2*, another aspect that had to be taken into consideration.

Table 0.2: A representation of the investigated alloy families, the chosen alloys and alloy-heat treatment combinations and the implemented casting processes.

Alloy family	Alloy or Alloy-heat treatment combination	Casting process
Al-Si	AlSi10MnMg	HPDC
	AlSi10MnMg-T5	
	AlSi10MnMg-T7	
	AlSi7MnMg	
	AlSi7MnMg-T5	
	AlSi7Mg0.3	
Al-Mg-Si	EN AB-42000	HPDC & RheoMetal™
	AlMg5Si2Mn	
	AlMg6Si2MnZr	
Al-Mg-Fe	AlMg4Fe2	
	MYFORD	

As seen in *Table 0.2*, the alloys and alloy-heat treatment combinations that were chosen for the casting trials belonged to three different alloy families.

0. Short version

Although most of the combinations in *Table 0.2* involved no heat treatment process, some of the plates that were produced using the AlSi10MnMg and AlSi7MnMg alloys were subjected to heat treatment. These alloys, which are currently being used by several automotive companies to produce the structural body castings, might not lead to the realization of the thesis' aim, as they typically need an expensive heat treatment process to fulfill the required mechanical properties of the 2020 Ford explorer shock tower ($Rp0.2 > 120$ MPa, $Rm > 180$ MPa and total elongation $> 10\%$) (1). Nevertheless, it was still important to investigate the different combinations of those alloys, especially AlSi10MnMg-T7, for the sake of providing a reference to the outcomes of the other as-cast alloying systems.

The main reason beyond investigating the remaining alloys in *Table 0.2*, beside their ability to meet the shock tower's mechanical requirements without heat treatment (2) (3), was their anticipated suitability to the RheoMetal™ process.

The need for an improvement in the feeding efficiency and the rheocastability of the standard AlMg4Fe2 alloy has led to the development of the MYFORD alloy during this thesis. This alloy, with the lower iron content of 0.5%, had, according to the Scheil-Gulliver equation based JMatPro® simulations in *Figure 0.1*, which were carried out by the company RheoMetal AB in Stockholm city, a different solidification sequence to the AlMg4FeX alloy, with an iron content (X) $\geq 1.3\%$, that involves the primary solidification of the α -Al phase.

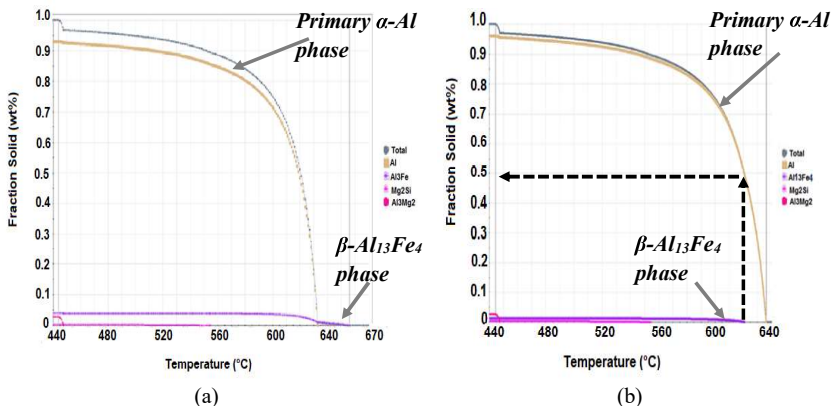





Figure 0.1: The JMatPro® simulations of the AlMg4FeX alloy with (a) X = 1.3% Fe and (b) X = 0.5% Fe (MYFORD).

0.3 The production of the plates and the parts

Using the defined alloys in the previous section, several test geometries were then produced at the different suppliers, as shown in *Table 0.3*, by the HPDC and the RheoMetal™ processes.

0. Short version

Table 0.3: The products of the casting trials.

Alloy or Alloy-heat treatment combination	Supplier	Geometry
AlSi7Mg0.3	Supplier 1: <i>The Foundry Institute (GI) of the RWTH Aachen University</i>	 <p>197 mm 237 mm Thickness = 3.1 mm</p>
AlMg5Si2Mn		
AlMg6Si2MnZr		
AlMg4Fe2		
AlSi10MnMg	Supplier 2: <i>Magna BDW technologies Soest GmbH</i>	 <p>30 cm 107 mm Thickness = 2.5 mm</p>
AlSi10MnMg-T5		
AlSi10MnMg-T7		
AlSi7MnMg		
AlSi7MnMg-T5		
EN AB-42000	Supplier 3: <i>Comptech AB</i>	 <p>464.98 mm Thickness = 1.01 mm (top), 2mm (bottom) and 2.1-2.68 mm (side)</p>
AlMg4Fe2		
MYFORD		

At supplier 1, HPDC and manual RheoMetal™ casting trials were conducted for four different alloys to produce the 3.1 mm thick plates. Each of the casting processes was conducted using a different gate design to enable the retrieval of the best possible outcome. For the HPDC trials a smaller and a narrower gate was used to produce an atomized jet flow. On the other hand, a wider and a larger gate design was implemented in the RheoMetal™ casting trials for the sake of ensuring a smooth and a non-restricted flow of the thixotropic slurry.

At supplier 2, smaller and thinner plates of the AlSi7MnMg and the AlSi10MnMg alloys were produced by HPDC and heat treated by the T5 and the T7 heat treatment processes.

0. Short version

At supplier 3, HPDC and automated RheoMetal™ casting trials were also conducted for three different alloys. However, unlike supplier 1, a much larger and a more complex geometry was casted for the purpose of obtaining results that can better resemble the possible testing outcomes of the 2020 Ford explorer shock tower in *Figure 0.2*.

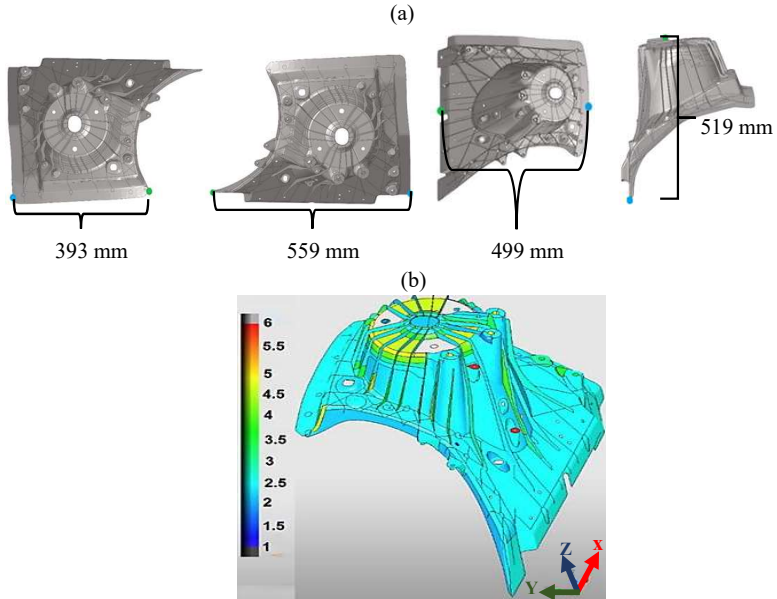


Figure 0.2: (a) The geometrical dimensions and (b) the thickness distribution (mm) of the 2020 Ford explorer aluminium shock tower.

In order to accurately compare between the testing outcomes from the different suppliers, the following approaches had to be taken into consideration to eliminate the influences of the thickness and the geometry of the cast part:

- i. Using a similar alloy for the casting trials at different suppliers.

By analyzing the AlMg4Fe2 alloy's test results and using it as a reference for the comparison with the other alloys, it was possible to correlate between the test outcomes from the suppliers 1 and 3.

- ii. Conducting simulations to predict the test outcomes at different thicknesses.


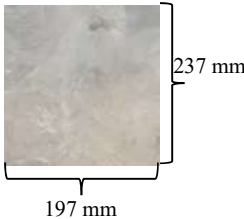
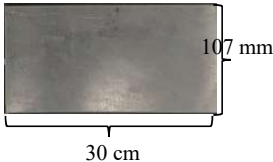
0. Short version

This was done, with the help of the Altair RADIOSS™ software by the Vehicle Systems Engineering and Technologies department of *Ford Werke GmbH* in Aachen city, mainly to offer a precise correlation between the impacts of the different alloys that were used at the suppliers 1 and 2 on the crash resistance potentials of the castings.

0.4 The evaluation criteria

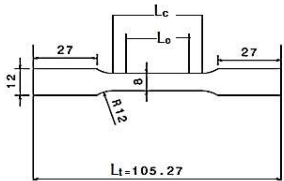
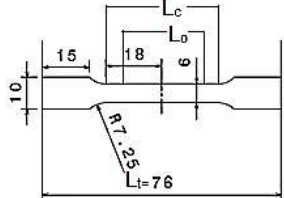
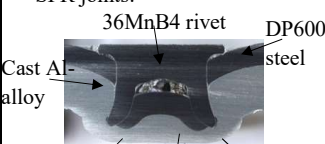
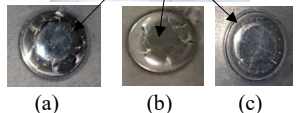

Thorough evaluation of the defined alloys and the casting processes was an important step towards achieving the thesis' aim. This evaluation involved performing several mechanical tests and analysis on the different alloys and alloy-heat treatment combinations that were used for the HPDC and the RheoMetal™ casting trials. A summary of all the conducted investigations, the test samples used, and the investigations' purposes are shown in *Table 0.4*.

Table 0.4: A detailed summary of the conducted investigations.

Investigation	Test sample	Aim of the investigation
(a) Microstructural and SEM-EDS analysis		<ul style="list-style-type: none"> • To identify the microstructural defects and the different phases within the studied alloy-heat treatment-casting process combinations • To assist in deriving the optimum process parameters for the RheoMetal™ casting trials at the suppliers 1 and 3
(b) Density measurements of the whole supplier 1 plates with the help of Archimedes' principle		<ul style="list-style-type: none"> • To assist in deriving the optimum process parameters for the HPDC and the RheoMetal™ casting trials at supplier 1
(c) Bending tests according to the VDA 238 -100 standard (4)		<ul style="list-style-type: none"> • To determine the influences of the studied alloy-heat treatment-casting process combinations on the crash resistance potentials of the castings

0. Short version

Table 0.4 (continued.)

<p>(d) Tensile tests according to method B of the ISO 6892-1 standard (5)</p>	<p>(a)</p>  <p>(b)</p>  <p>The geometrical dimensions in mm of (a) the Type E sample (6) and (b) the mini sample</p>	<ul style="list-style-type: none"> • To determine whether the studied alloy-heat treatment-casting process combinations could meet the mechanical requirements of the 2020 Ford explorer shock tower • To assist in deriving the optimum process parameters for the HPDC trials and the RheoMetal™ casting trials at supplier 1
<p>(e) Analysis of the self-piercing riveting (SPR) joints by checking for and analyzing the severity of the cracks on their outer surfaces and by conducting lap shear tests</p>	<ul style="list-style-type: none"> • SPR joints:   <p>Possible unacceptable outer joint surface cracks such as (a) the circumferential cracks and (b) the deep radial cracks, and borderline cracks such as (c) the light radial cracks</p> <ul style="list-style-type: none"> • Lap shear test samples:  <p>Cast Al-alloy SPR joint DP600</p>	<ul style="list-style-type: none"> • To determine the rivetability of the studied alloy-heat treatment-casting process combinations • To determine the strengths of the best SPR joints.

0. Short version

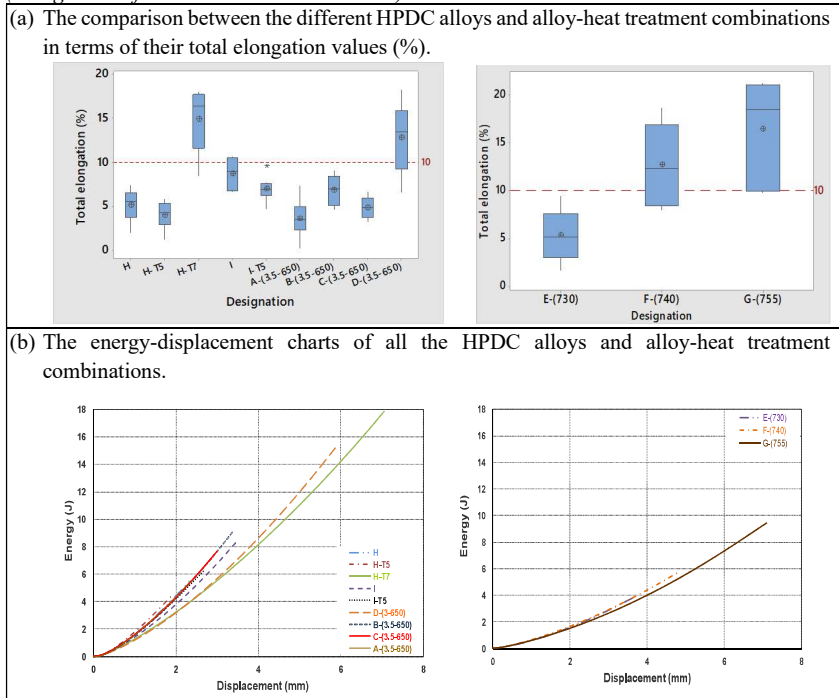
0.5 The high pressure die casting trials

Before conducting the HPDC trials at the different suppliers and to make sure that the qualities of the casted plates and parts were going be adequate, it was important to derive the optimum HPDC process parameters, such as the intensification pressure and the melt flow velocity.

For the trials at supplier 1 and as shown in *Table 0.4*, this step was done by analyzing the densities and the tensile tests' outcomes of the plates that were initially produced using different process parameters. However, for the trials at supplier 3, no detailed investigation was conducted, and the optimum process parameters were mainly derived based on information from the literature and on the supplier's recommendations. Contrary to the trials at supplier 1 and 3, no optimum process parameters for the trials at supplier 2 were derived, as the cast plates were received directly from the supplier.

The analysis of *Table 0.4*'s investigations, which were performed on the casted plates and parts, was then done leading to the findings in *Table 0.5*.

























Table 0.5: The main findings of the conducted investigations on the HPDC plates and parts. (*Designations from Table 4.3 and Table 4.9*)



0. Short version













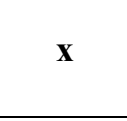











Table 0.5 (continued.)

(c) The evaluation of the SPR joints between the high pressure die castings and the DP steel sheets, where (√) is acceptable, (x) is unacceptable and (o) is borderline.

Designation	Rivet-die combinations from <i>Table 4.11</i>			
	1 st combination BG0542EHL0- EHG13209	2 nd combination BG0542EHL0- EHG13210	3 rd combination BG0542EHL0- EHG14034	4 th combination BG0E44EHL0- EHG14033
H	X 	X 	X 	X 
H-T5	X 	X 	X 	o 
H-T7	X 	√ 	√ 	√ 
I	X 	X 	o 	√ 
I-T5	X 	X 	o 	√ 
A-(2.5-650)	X 	X 	X 	o 

0. Short version

Table 0.5 (continued.)

B-(2.5-650)	X 	X 	0 	√ 
C-(2.5-650)	X 	X 	X 	X 
D-(3-650)	X 	√ 	√ 	√ 
E-(730)	X 	X 	X 	0 
F-(740)	X 	X 	√ 	√ 
G-(755)	X 	√ 	√ 	√ 

As shown in *Table 0.5*, AlMg4Fe2 (D-(3-650) & F-(740)), MYFORD (G-(755)) and AlSi10MnMg-T7 were respectively the HPDC alloys and alloy-heat treatment combination with the ability to fulfill the mechanical requirements of the 2020 Ford explorer shock tower. In addition, they led to the highest crash resistance potentials and showed the best rivetability.

0. Short version

As a result of these findings and since AlSi10MnMg-T7 is the currently implemented alloy-heat treatment combination in the production of the investigated shock tower, it is acceptable to consider AlMg4Fe2 and MYFORD as proper candidates for the cost-efficient mass production of the thin walled structural body castings. Between these two combinations, MYFORD is considered to be the better candidate for serving the thesis' aim, due to its better performance in each of the conducted investigations.

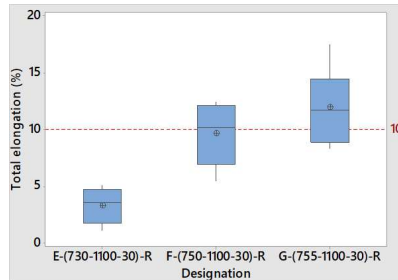
0.6 The RheoMetal™ casting trials

Unlike the HPDC trials and due to the inefficiency of the manual RheoMetal™ casting trials at supplier 1, acceptable conclusions were only drawn from the conducted investigations on the supplier 3's RheoMetal™ casted parts.

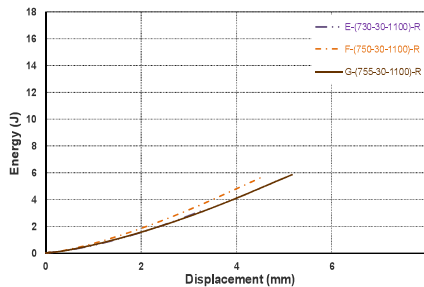
Although the optimum process parameters were derived, they were not applied in the RheoMetal™ casting trials at supplier 3. This was due to the dependence of supplier 3 on *RheoMetal AB's* recommended process parameters values.

Table 0.6: The main findings of the conducted investigations on the RheoMetal™ casted parts. (*Designations from Table 4.9*)

(a) The comparison between the different RheoMetal™ alloys in terms of their total elongation values (%).













(b) The energy-displacement chart of the RheoMetal™ alloys



0. Short version

Table 0.6 (continued.)

(c) The evaluation of the SPR joints between the RheoMetal™ castings and the DP steel sheets, where (√) is acceptable, (x) is unacceptable and (o) is borderline.

Designation	Rivet-die combinations from Table 4.11			
	1 st combination BG0542EHL0- EHG13209	2 nd combination BG0542EHL0- EHG13210	3 rd combination BG0542EHL0- EHG14034	4 th combination BG0E44EHL0- EHG14033
E-(730-30-1100)-R	X	X 	X 	O 
F-(750-30-1100)-R	X	X 	√ 	√ 
G-(755-30-1100)-R	X 	√ 	√ 	√ 

As seen in *Table 0.6*, MYFORD (G-(755-30-1100)-R) was able to deliver better performance than the other alloys that were used for the RheoMetal™ casting trials. This finding, which is similar to the main HPDC trials' outcome in *section 0.5*, can be traced back to the microstructural architecture of this alloy that offers less restriction to the dislocation movement and therefore maximizes the suitability of implementing it in the cost-efficient mass production of the thin walled structural body castings.

However, by comparing between the energy-displacement charts in *Table 0.5* and *Table 0.6*, it is obvious that the RheoMetal™ process led to cast parts with lower crash resistance potentials than those produced using the HPDC process. This outcome can be contributed to the less restricted flow of the liquid melt, in comparison to the RheoMetal™ process' thixotropic slurry, in the low thickness casted parts. Therefore, implementing the RheoMetal™ process in the production of thicker and smaller cast parts can be a recommendation that improves its projected outcomes.

1. Introduction and motivation

1 Introduction and motivation

1.1 Background information

The car emissions, especially the CO₂ emission, contribute greatly to global warming. Therefore, in order to help tackle this problem, which can lead to an increase in the climate change and to long term negative health impacts (7), many countries continue to set rules and emission targets, as illustrated in *Figure 1.1*.

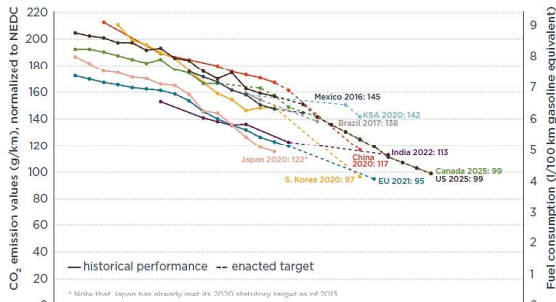


Figure 1.1: The current and future CO₂ emission requirements for passenger cars (8).

The aim of reaching a future emission target of 95g CO₂/km by the year 2021 in Europe requires an overall reduction in the body-in-white's weight. This is because lighter vehicles generally consume less fuel in comparison to their heavier counterparts, and therefore produce lower CO₂ emissions. One of the means that can assist in decreasing the weight of the vehicles is to replace the heavy materials in their vehicle body structures (e.g. steel) with lighter materials, such as aluminium. This statement is confirmed by *Figure 1.2*, which shows the increased tendency in the last 40 years towards integrating more aluminium in the vehicles' structures.

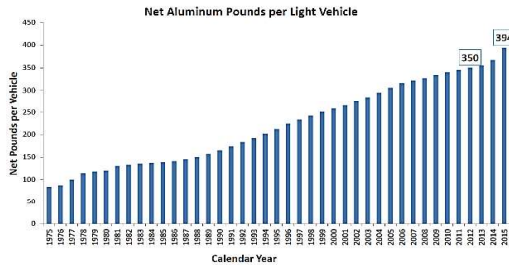


Figure 1.2: The increase in the aluminium weight per vehicle over a 40 years span in the North American market (9).

1. Introduction and motivation

Aluminium can be introduced into the vehicles' structures in a number of different forms. As shown in *Figure 1.3*, sheets, extrusions and vacuum die castings are considered to be among the different forms that assist in the overall reduction in the fuel consumption and the CO₂ emissions (9). In comparison to the other two forms, castings offer additional weight saving potential and less assembly steps due to their better functional integration (10) (11).

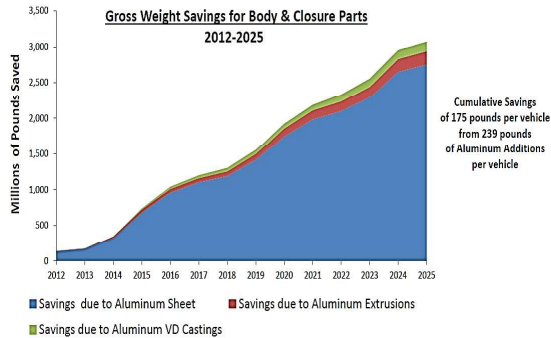


Figure 1.3: The total weight saving over a 13 years span, due to the integration of aluminium sheets, extrusions and vacuum die castings (VD) into the car body and closure parts (9).

Figure 1.4 provides an overview about the different body-in-white (BIW) sections, which were considered as lightweight metal candidates within the multi material lightweight vehicle project (MMLV). From this study, it was evident that shock towers, rear rails, torque boxes and hinge pillar reinforcements can serve as good aluminium die casting candidates.

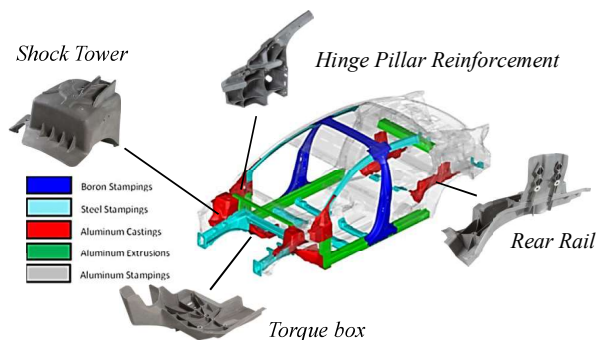


Figure 1.4: MMLV BIW design (12).

1. Introduction and motivation

1.2 Aim of the thesis

This thesis was conducted with the main aim of developing a cost-efficient process route for the mass production (1,000,000 - 2,000,000 parts) of thin-walled structural aluminium body castings. The reason beyond choosing this aim is the higher costs of the structural body parts, which are made up from aluminium castings instead of steel sheets. These higher costs can be mainly contributed to the more expensive raw materials that make up the aluminium castings.

1.3 Research approach

For the sake of achieving the goal of this thesis, the milestones in *Figure 1.5* were considered and implemented.

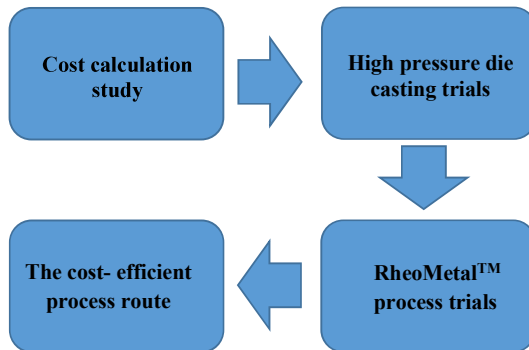


Figure 1.5: The thesis milestones.

As shown in the above sequence, the first step involved conducting a cost calculation study for the purpose of identifying the factors with the highest influence on the cost of a thin-walled structural aluminium body casting (2020 Ford explorer's shock tower). A complete description of this study and its outcomes is represented in chapter 3.

The second and third steps involved performing the high pressure die casting (HPDC) trials and the RheoMetal™ casting trials on the basis of the cost calculation study's findings. The outcomes of those trials are illustrated respectively in chapters 5 and 6.

In the last step, which is demonstrated in chapter 7, comparisons between the outcomes of the HPDC trials and the RheoMetal™ casting trials were done to determine the cost-efficient process route for the mass production of the investigated thin-walled structural aluminium body casting (2020 Ford explorer's shock tower).

2. Theoretical background and state of the art

2 Theoretical background and state of the art

2.1 Automotive Casting parts

Several automotive companies (OEMs) have already introduced the aluminium castings into their product portfolio in the form of structural body parts. An overview about such parts, which are produced using the standard Al-Si casting alloys, was provided by *Magna BDW technologies Soest GmbH* and is shown below:

Weight: 7.6 Kg
Size: 1150 * 850 * 400 mm³
Alloy: AlSi7MnMg
Heat treatment: T5
Yield strength: 145 MPa
Ultimate tensile strength: 240 MPa
Elongation > 8 %
Volume of production per year ~
72000 parts



Figure 2.1: Porsche 911- rear Longitudinal rail (*Magna BDW technologies Soest GmbH*).

Size: 330 *400 * 380 mm³
Alloy: AlSi10MnMg
Heat treatment: T7
Yield strength: 120 MPa
Ultimate tensile strength: 180 MPa
Elongation > 10 %
Volume of production per year ~
600000 parts



Figure 2.2: Jaguar XE/XF- Front shock tower (*Magna BDW technologies Soest GmbH*).

Weight: 8.9 Kg
Size: 1500* 500 * 400 mm³
Alloy: AlSi10MnMg
Heat treatment: T7
Yield strength: 120 MPa
Ultimate tensile strength: 180 MPa
Elongation > 10 %
Volume of production per year ~
400000 parts



Figure 2.3: Range rover- rear longitudinal frame (*Magna BDW technologies Soest GmbH*).

2. Theoretical background and state of the art

2.2 Casting methods

The automotive casting processes can be classified, as shown in *Figure 2.4*, according to the mold filling technique (A) or to the type of the mold/die used (B) (13).

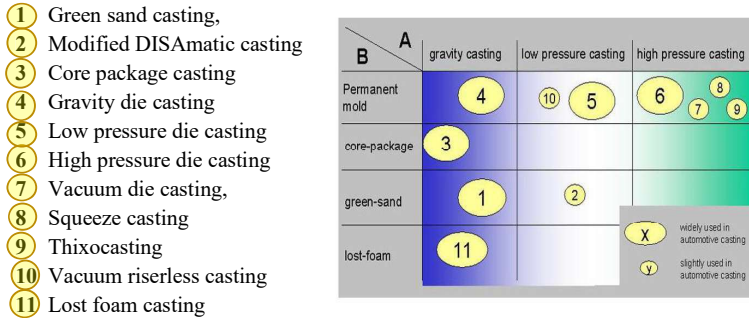


Figure 2.4: The casting processes and the extent of their implementation in the automotive industry (13).

From *Figure 2.4*, it is clear that processes such as high pressure die casting, gravity die casting, low pressure die casting and green sand casting are widely used in the automotive industry. Other processes such as thixocasting, modified DISAmatic casting and vacuum riserless casting are used slightly in the production of automotive parts.

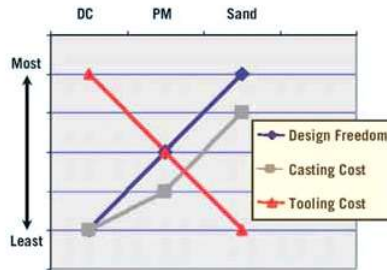


Figure 2.5: The properties of the different casting methods (14).

As shown in *Figure 2.5*, and although die-casting (DC) involves a higher tooling cost than other permanent mold (PM) and sand casting (sand) processes, it is still considered, due to its lower casting cost, to be a more cost-efficient process for the mass production of aluminium castings (14).

2. Theoretical background and state of the art

2.3 High pressure die casting

Die casting is classified into several different processes as shown in *Figure 2.6*.

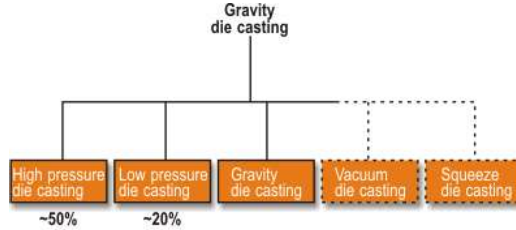



Figure 2.6: The different die-casting processes (15).

The most often-used die casting process is high pressure die casting (HPDC), which accounts for approximately half of the overall light metal casting production (15). This, together with its short cycle time, makes it a more attractive die casting process for the large volume production of automotive body parts.

2.3.1 The process flow





In order to estimate the main cost drivers of the HPDC process, it is very important to have a complete and a thorough understanding of its various stages and of the process flow. The twelve successive steps, according to *TRIMET Aluminium SE*, which are required for the production of structural aluminium car body parts using HPDC, fall under the three major stages in *Table 2.1* as follows.

Table 2.1: The process flow and the major stages for the production of the structural aluminium car body parts by HPDC. Pictures are provided by *TRIMET Aluminium SE*.

Stages	Process flow	Setup
(a) Melting and transferring the feedstock	1. Melting of the feedstock (ingots) in a gas fired or an induction furnace.	 <p>Melting furnace.</p>







2. Theoretical background and state of the art

Table 2.1 (continued).

	<p>2. The melt is then transferred to the holding electric resistance furnace in the HPDC cell.</p>	 <p>Holding furnace.</p>
<p>(b) Production of the semi-finished cast parts in the HPDC cell</p>	<p>3. Feeding of the melt from the holding furnace into the shot sleeve of the HPDC machine, with the help of a ladle attached to a robot arm, is done at this step.</p>	 <p>Plunger Ladle</p> <p>Feeding of the melt into the die and pressing it to produce the part(s).</p>
	<p>4. Each part is then produced after pressing the melt into the die with a plunger at a certain velocity, followed by subjecting the melt to an intensification pressure.</p>	<p>Feeding of the melt into the die and pressing it to produce the part(s).</p>
	<p>5. After the solidification phase, the die is then opened for the following two reasons:</p> <ol style="list-style-type: none"> To remove the part(s). To be cooled, cleaned and lubricated by spraying. 	 <p>Removal of the part(s) and the die spraying.</p>
	<p>6. The gating system is then disengaged from each part with the help of a trimming machine.</p>	 <p>Trimming machine.</p>

2. Theoretical background and state of the art

Table 2.1 (continued).

(c) Machining and further processing to produce the finished cast parts	7. Deburring of the part's rough edges is done at this stage either manually or with the help of a special machine.	 Deburring machine.
	8. At this point, heat treatment is done if needed to achieve the required mechanical properties.	 Heat treatment furnace.
	9. Mechanical adjustments to each part are then applied to reach the aimed geometry.	 Mechanical adjustments machine.
	10. Mechanical working with the help of a CNC machine is then performed at this step.	 CNC machine for mechanical working.
	11. Surface treatment, e.g. coating is implemented.	 Surface treatment station.
	12. The last stage involves packaging and storing the parts in the warehouse prior to their delivery to the customers.	 Storage of the packaged parts.

2. Theoretical background and state of the art

2.3.2 The influence of the process parameters

➤ Melt flow velocity

The melt flow velocity, which can be represented in terms of the piston or the gate velocities, is considered as one of the main parameters that can influence the outcome of the HPDC process. This velocity is not constant throughout the different phases of the casting process. In other words and based on information about the changeover point (16), a lower melt flow velocity is needed during the movement inside the shot sleeve (first phase) to account for a better gathering of the melt without air entrapment. However, a higher velocity is needed during die filling (second phase) to prevent the premature solidification of the melt that can negatively impact the quality of the casting.

The magnitude of the melt flow velocity, especially during the die filling phase, and its effect on the mechanical properties of the cast part was an interesting topic of investigation throughout the years. Old studies such as the ones mentioned in Robert Karban's literature review did not show a consistent influence of the melt flow velocity on the mechanical properties (17). However, a more recent study showed that by increasing the melt flow velocity during the die filling phase, it is possible to increase the spraying of the melt and the turbulence of the flow (18). These effects cause the formation of smaller α -Al particles due to the increase in the shear rate at the gate, and additionally results in better feeding, finer pores and fragmented inclusions. All these outcomes contribute eventually to better mechanical properties as shown in *Figure 2.7*.

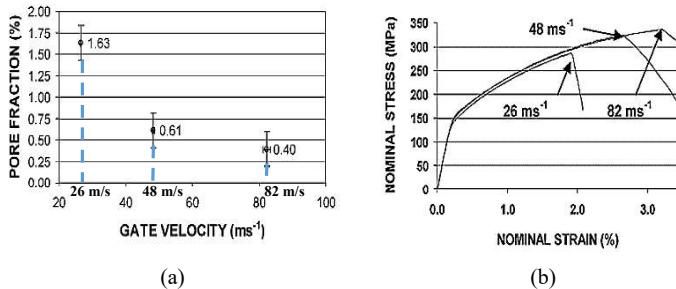


Figure 2.7: (a) The effect of the gate velocity on the pore fraction and on (b) the mechanical properties (modified from (18)).

It has to be noted that very high melt flow velocities might result in die erosion and low surface quality of the parts. Therefore, most of the die casters limit the gate velocity to a maximum of 40 m/s (19).

2. Theoretical background and state of the art

➤ Intensification pressure

Intensification pressure (IP) refers to the pressure that is applied after the die is completely filled to improve the mechanical properties and the soundness of the casting. This improvement takes place via the reduction of the porosities that develop as a result of the gas evolution, the solidification shrinkage near the gate and the entrapped air (20).

There is a direct correlation between the reduction in the porosity content, as a result of higher intensification pressure, and the increase in the density of the part. This correlation and its subsequent effect on the macrostructure of the part are represented clearly in *Figure 2.8 (b)* as follows.

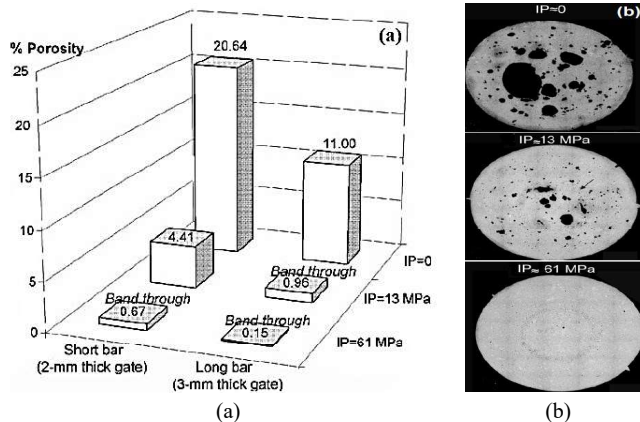


Figure 2.8: The effect of the intensification pressure (IP) on (a) the porosity content and (b) the macrostructures of the high pressure die castings (modified from (21)).

➤ Vacuum

Maintaining a vacuum condition during the high pressure die casting process, as shown in *Figure 2.9*, is considered to have a remarkable influence on the quality and the mechanical properties of the casting. In addition, it is considered to increase the cast part's tolerance to the application of heat treatment.

The above advantages can be contributed to the reduction in the pore content of the cast part, as a result of the vacuum-induced pressure values in the die and the shot sleeve that are lower than the atmospheric pressure (22).

2. Theoretical background and state of the art

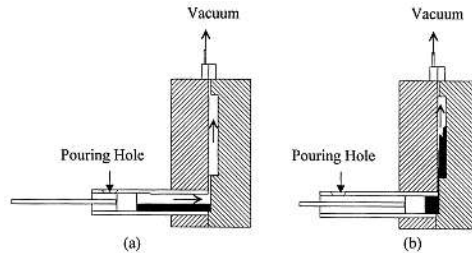


Figure 2.9: The concept of vacuum assisted die casting (22).

As seen in *Figure 2.9 (a)*, the vacuum assisted die casting process proceeds by activating the vacuum valve, at the top of the die, as soon as the piston surpasses the pouring hole of the shot sleeve during injection.

2.3.3 The influence of the casting part's wall thickness

In addition to the process parameters, the microstructure of the casting part has a major influence on its mechanical properties.

One factor that affects the microstructure is the cooling rate during solidification, which is inversely related to the wall thickness of the part. In other terms, increasing the wall thickness results in a slower cooling rate during solidification, and vice versa (23).

The microstructural features that are affected by the cooling rate are the grain size, secondary dendritic arm spacing (SDAS) and, in the case of the Al-Si alloys, the size and shape of the eutectic silicon particles. Increasing the cooling rate, by, e.g. decreasing the wall thickness, results in a decreased SDAS, refined grain size and small eutectic silicon particles (24), which have a similar but not an identical shape to that of the modified eutectic silicon.

The smaller SDAS and the very small eutectic silicon particles, as a result of the faster cooling rates, causes an overall enhancement in the soundness of the cast part by decreasing the amount of shrinkage cavities, porosities, non-metallic inclusions and segregations (25).

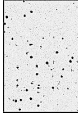




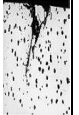
2.3.4 The typical defects

Casting defects might develop in a number of ways during HPDC. These defects play a role in deteriorating the mechanical properties by acting as sites for crack initiation and propagation. Therefore, in order to detect the inefficiencies in the casting process and for the sake of reducing and probably avoiding the formation of such defects, it is very important to clearly distinguish between their different types and to identify the influencing parameters that play a role in their evolution.

2. Theoretical background and state of the art

Some of the typical HPDC's defects are illustrated in *Table 2.2* as follows.

Table 2.2: The typical internal defects in HPDC and their root causes (26) (16) (Mertz.A (1994), as cited in (27)).

Influencing parameters		Defects					
		Gas porosities 	Gas Blisters 	Shrinkage porosities 	Hot tear 	Hard inclusions 	Oxides 
Parameters depending on the die and the gate.	Die temperature	+	+	+	+	-	-
	Type / quantity of the die lubricants	++	++	-	-	+	-
	Die lubricant's mixing ratio	+	+	-	-	+	-
	Gate position	++	+	++	-	-	0
	Gate geometry	+	+	++	-	-	0
	Gate thickness	++	+	++	-	-	-
	Die ventilation / cross section of the part	++	++	-	-	-	-
Die cooling / temperature and cooling rate of the die cooling lubricants	+	+	+	+	-	-	
Parameters depending on the melt	Melt temperature	-	-	0	+	+	+
	Alloy composition	+	-	+	+	+	+
	Melt cleanliness	+	+	-	-	+	+
Parameters depending on the HPDC machine	Piston velocity (1 st phase)	+	+	-	-	-	0
	Melt's velocity in the gate (2 nd phase)	+	+	-	-	-	-

2. Theoretical background and state of the art

Table 2.2 (continued).

	Transition point between the 1 st and 2 nd phase (changeover point)	+	+	-	-	-	-
	Increase in the pressure till the 3 rd phase	+	+	+	-	-	-
	Intensification pressure during the 3 rd phase	++	+	+	-	-	-
	Cycle time	0	+	-	+	-	-
Parameters depending on the shot sleeve	Shot sleeve geometry/ fill degree	+	+	-	-	-	-
	Piston lubricants	+	+	-	-	+	+

++ Resembles a very large influence, + resembles a large influence, 0 resembles a small influence and - resembles no known influence.

Other casting defects that can also evolve during the HPDC process include:

- Cold flakes, which are defects that occur during the early stages of die casting as a result of the breakdown and the redistribution of the shot sleeve's initially solidified layers of melt (28).

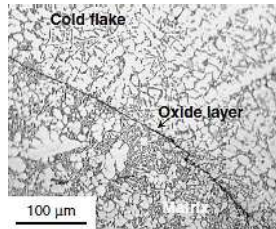


Figure 2.10: The structure of the cold flake and its accompanying oxide layer (28).

As shown in Figure 2.10, each cold flake is characterized by being accompanied by an oxide layer, which acts as a source of crack initiation and propagation due to its brittle nature and porous structure (29).

- Dilatant shear bands, which are defect bands that develop under shear due to the strain localization in lower solid fraction (f_s) regions. The condition for such shear bands to

2. Theoretical background and state of the art

develop is $f_s > f_s^{coh}$, where f_s is the solid fraction of the melt and f_s^{coh} is the dendrite coherency solid fraction (30) (21).

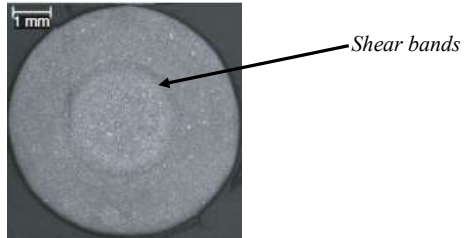


Figure 2.11: Shear bands in a HPDC test bar of an AlSi7Mg0.3 alloy (30).

- Microsegregation, which occurs during solidification due to the enrichment of the interdendritic liquid phase with the solid phase's rejected solutes. Although this defect leads to the development of undesirable constituents that can deteriorate the mechanical properties, it can however be eliminated by the application of further heat treatment and hot working processes (31).

2.4 Semi-solid casting

Semi-solid casting is an enhanced form of die casting in which the input material is a viscous slurry consisting of around 25-50% solid and 50-75% liquid (32). This method was implemented to help tackle the issue of the gas porosities, which are usually developed in the standard liquid die castings because of the turbulent flow of the melt into the die. These gas porosities reduce the mechanical properties of the castings by acting as sites for crack initiation and propagation. They also hinder the ability of the casting to be subjected to heat treatment, as they may develop into blisters at elevated temperatures.

In addition to the input material, other differences between the semi-solid and the liquid die casting processes include the feeding velocity into the die as well as the final microstructure of the cast part. These differences are thoroughly clarified in the following bullet points:

- The typical gate velocity of the melt in the liquid die casting process is, as mentioned earlier in section 2.3.2 ≤ 40 m/s. On the other hand, a much slower gate velocity is needed in the case of semi-solid casting to maintain a laminar flow into the die. According to an earlier study by S.P.Midson, this gate velocity was found to be in the range of 0.63-5 m/s for a 9 mm thick gate (33). Although this gate velocity is seemingly low, it still exceeds the liquid die casting's limit of 0.5m/s for a laminar flow (34).
- Unlike the dendritic structure that is formed by the conventional liquid die casting process, the morphology of the primary α -Al phase is, as seen in *Figure 2.12*, globular in the case of

2. Theoretical background and state of the art

semi-solid casting. This difference in the morphology of the primary α -Al phase is what gives the semi-solid slurry its thixotropic behaviour, as it offers less restriction to the flow of the liquid phase under the application of a shear force (35) (36). In addition, decreasing the size of the primary globular α -Al phase can assist in improving the mechanical properties of the cast part by enhancing the feeding capability of the melt and by resulting in a finer distribution of the micro porosities and the intermetallic phases (37). The different mechanisms governing the formation of these finely dispersed globular grains are explained in the upcoming sections.

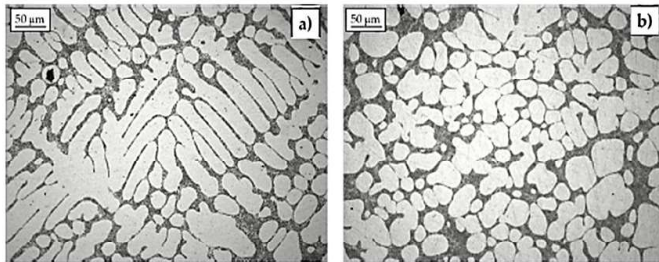


Figure 2.12: The typical die casting microstructures of the AlSi7 alloy that are formed using (a) the conventional liquid die casting process and (b) the semi-solid casting process (38).

The volume fraction of the globular particles (solid fraction), the shear rate and time are the main factors affecting the viscosity of the slurry (39). The higher the viscosity, the easier it is to control the flow into the die without splashing or turbulence (32), and the lower the chance for the subsequent entrapment of unwanted gas porosities.

Additional advantages of semi-solid casting in comparison to conventional liquid die casting include (39):

- i. The higher suitability of their cast parts, with lower entrapped gas content, to welding and heat treatment.
- ii. Longer tool life and less die soldering due to the lower temperature of the slurry (~ 100 °C).
- iii. As a result of the high solid fraction in the viscous slurry ($\sim 40\%$), less volume contraction occurs during the solidification of the melt, which leads to less shrinkage porosities in the final cast structure.

On the other hand, and based on information from the company *RheoMetal AB*, the semi-solid casting processes have some disadvantages such as:

- i. Small solidification range alloys are not suitable.
- ii. Temperature control is needed for most processes.

2. Theoretical background and state of the art

- iii. Thicker gates, which must be later cut or sawn, are needed to support the flow of the viscous slurry into the die.

The semi-solid casting processes can be classified, based on their process flow, into the two main branches of thixocasting and rheocasting. An overview of the different processes that fall under each branch is presented in *Figure 2.13* as follows.

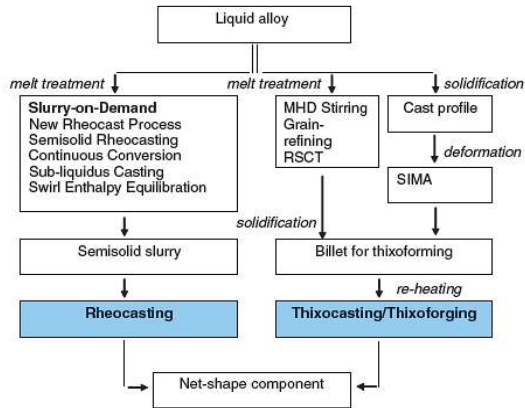


Figure 2.13: Different technologies for the semi-solid casting of the metallic alloys (modified from (40)).

2.4.1 Thixocasting

Thixocasting is considered to be the first implemented semi-solid casting process. It is made up of three main stages, as shown in *Figure 2.14*.

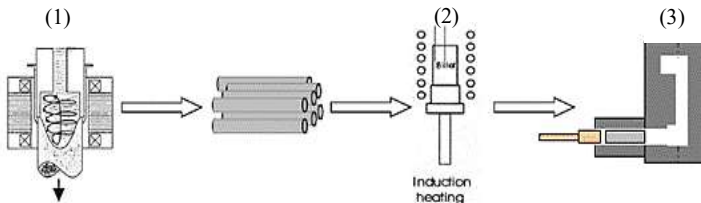


Figure 2.14: The main stages in thixocasting (41).

2. Theoretical background and state of the art

A detailed description of the different stages in *Figure 2.14* is shown below (39):

- (1). The first stage involves the production of special billets with globular microstructures. These billets, which are needed for the successive stages, can be produced, as shown in *Figure 2.15*, by direct chill casting that is accompanied by a stirring action. This stirring action affects the solidification of the billet by hindering the dendrites' development.

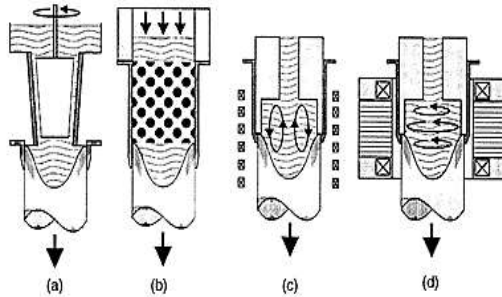


Figure 2.15: Different techniques of melt stirring: (a) mechanical stirring, (b) passive stirring, (c) electromagnetic vertical stirring, (d) electromagnetic horizontal stirring (39).

- (2). The second stage in thixocasting involves reheating the billets into the semi-solid range by placing them into an induction furnace.
- (3). The third and last stage involves inserting each of the reheated billets into the shot sleeve of a high pressure die casting machine, where it is then pressed into the final desired shape.

The advantages of thixocasting include (32):

- i. The ability to be produce high quality parts with advanced mechanical properties.
- ii. The process is consistent in the sense of its ability to produce precast billets with very similar microstructures and chemistries.

However, the main disadvantages of this process include (42):

- i. The process is expensive due to the cost of producing the special thixofomed billets, which should have a solid fraction between 50% to 60% to be able to support its own weight (43), and the cost of running the induction furnace.
- ii. The scrap cannot be remelted in house and must be sent back to the billet suppliers.
- iii. As shown in *Figure 2.16*, the typical thixocasting microstructure consists of regions of entrapped liquid within the primary globular particles. These entrapped liquid negatively affect the flow and increase the viscosity of the semi-solid slurry by causing a reduction in the overall liquid fraction surrounding the particles (39).

2. Theoretical background and state of the art

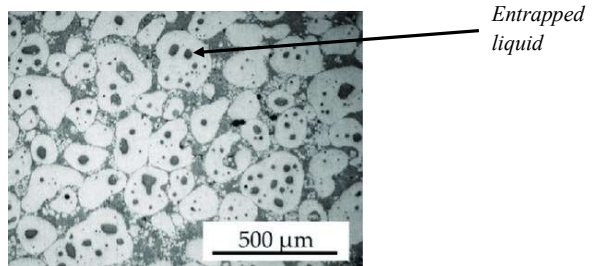


Figure 2.16: A typical thixocasting microstructure of the A356 alloy with regions of entrapped liquid (44).

2.4.2 Rheocasting

This process can overcome the disadvantages of thixocasting by directly producing the semi-solid slurry from the liquid melt.

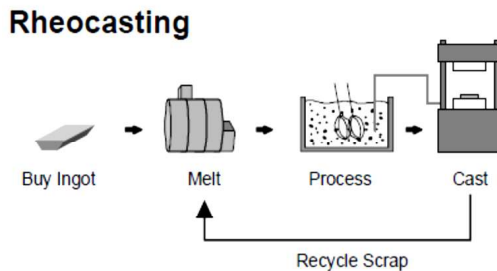


Figure 2.17: Illustration of the process steps in rheocasting (45).

As shown in *Figure 2.17*, the viscous slurry can be generated by cooling the melt into the semi-solid range and simultaneously stirring it to achieve the required globular microstructure. The semi-solid slurry is then poured into the shot sleeve of the high pressure die casting machine, before being injected into the die in a similar manner to that in thixocasting (32).

Some of the advantages of rheocasting in comparison to thixocasting include (45):

- i. No need for special billets.
- ii. The ability to recycle the scrap and perform modifications to the alloy in-house.
- iii. The solid fraction can be adjusted according to the aimed application.
- iv. No limitation of the shot size.
- v. No regions of entrapped liquid are found within the primary globular particles.

2. Theoretical background and state of the art

As shown above, this process can overcome the main disadvantages of thixocasting. However, it still has a major concern regarding the consistency of the product, as it produces the part from a single dose of melt. This approach makes it difficult for the rheocasting process to attain the same thixocasting's levels of melt cleanliness, as the feeding material for the thixocasting billets are usually produced in 50,000 lbs batches (Jorstad (2000) as cited in (32)).

In the case of rheocasting, several approaches can be used to generate the globular microstructure of the semi-solid slurry. These approaches include (46):

- i. Stirring the melt as it cools down by any of the techniques in *Figure 2.15*.
- ii. Subjecting the semi-solid slurry after cooling to turbulent shakes. This is needed to cause the breakdown of the dendrites into small solid particles, which later develops into the globular microstructure.
- iii. The formation of a large number of solidification nuclei by subjecting the liquid melt, which is slightly above its liquidus temperature, to rapid cooling.

As shown in *Table 2.3*, many rheocasting processes have been developed with each adopting one or more of the above-mentioned agitation approaches for the generation of the globular microstructure.

Table 2.3: Different rheocasting processes with their respective agitation techniques (46).

Process	Agitation technique for slurry making
SEED	Stirring
Rheo - Die casting	Dendrite fragmentation/ stirring
Honda	Stirring
ATM	Pressure waves
Sub-liquidus casting	Numerous nuclei
Direct thermal method	Numerous nuclei
Buhler	Numerous nuclei
Hitachi	Stirring
New Rheocasting	Numerous nuclei
Gibbs	Stirring
Slurry on demand	Stirring
Semi-Solid Rheocasting	Stirring + Numerous nuclei
Continuous Rheoconversion process	Dendrite fragmentation
Induction heating/stirring	Stirring
Controlled diffusion solidification	Numerous nuclei

Most of the processes in *Table 2.3* require an external temperature control to achieve the aimed viscous state of the semi-solid slurry.

2. Theoretical background and state of the art

2.4.3 The RheoMetal™ process

According to (47), the following criteria should be taken into consideration in order to favor a certain rheocasting process:

- i. The ability of the process to improve the quality of the metallic slurry by producing fine and uniform globular microstructures.
- ii. The ability of the rheocasting process to produce the products at a faster pace. This can lead to a corresponding decrease in the production costs and an increase in the productivity.

The above criteria were fulfilled by the development of the RheoMetal™ process, which, unlike most of the other processes in *Table 2.3* and as seen in *Figure 2.18*, depends on enthalpy exchange and not on temperature control to create the semi-solid slurry.

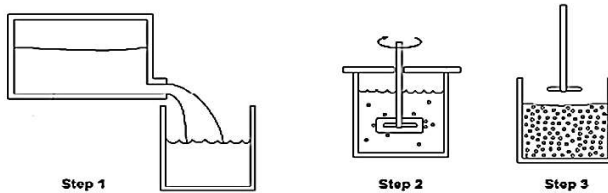


Figure 2.18: The slurry preparation in the RheoMetal™ process: Step 1) pouring the melt into the ladle, Step 2) inserting the rotating enthalpy exchange material (EEM) into the melt, step 3) the semi-solid slurry is formed (48).

The setup in *Figure 2.18* is very similar to the one used for the Semi-Solid Rheocasting process (S.S.R.™). However, in the case of S.S.R.™ and as shown in *Figure 2.19*, a rotating copper rod is inserted into the melt instead of the EEM to cause a sudden decrease in the temperature and to initiate solidification (41).

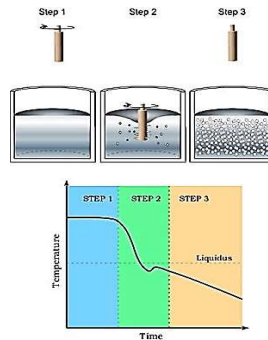


Figure 2.19: An illustration of the Semi-Solid Rheocasting process (S.S.R.™) (41).

2. Theoretical background and state of the art

Due to its dependence on enthalpy exchange, the RheoMetal™ process offers a number of additional advantages in comparison to the conventional rheocasting processes that depend on temperature control. These advantages include:

- i. Being the faster process as the slurry formation takes place due to the convective heat transfer between the superheated melt and the EEM.
- ii. The viscous slurry is more stable because the solid fraction is formed by the melting of the EEM as well as the nucleation of the superheated melt (49).
- iii. Its lower cost since external temperature control is not needed to achieve the required solid fraction.

2.4.3.1 The process flow and the typical products

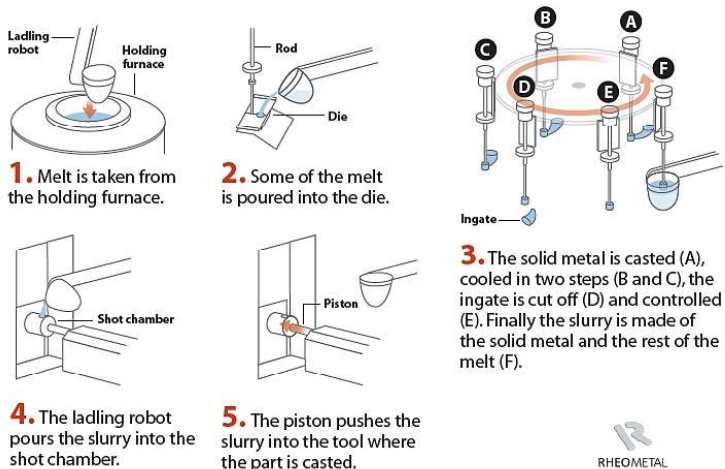


Figure 2.20: A schematic diagram of the RheoMetal™ process (source: RheoMetal AB).

The above diagram illustrates the five consecutive steps that are used for the industrial implementation of the RheoMetal™ process. The first two steps are designed for the production of the EEM. The third step is where the viscous slurry is produced by inserting the EEM into a ladle filled with a certain volume of the liquid melt. The feeding of the slurry into the shot sleeve, with the help of the ladling robot, and into the die to form the cast part take place in the last two steps.

The remaining steps in the process flow, which are needed for reaching the end product, are exactly similar to steps 4 to 12 in *Table 2.1*.

2. Theoretical background and state of the art

An example of the products that are produced by the RheoMetal™ process are represented in *Figure 2.21* as follows (source: *RheoMetal AB*):



Figure 2.21: (a) Dock cleat (b) LED housing and (c) Brackets for the telecom industry.

As seen in *Figure 2.21*, the RheoMetal™ process can produce relatively thick products, which require high quality standards, for the telecom and the ship building industries.

The structural car body parts, on the other hand, are not included in the product portfolio of the RheoMetal™ process. This can be mainly contributed to the large dimensions and the low thicknesses of those parts.

2.4.3.2 The influence of the process parameters

➤ *Melt flow velocity*

Unlike in HPDC, higher melt flow velocity in the RheoMetal™ process results in an overall deterioration in the mechanical properties of the cast part due to its influence on the subsequent increase in the amount and the scattering of the pores within the melt. This increase in the pore content is mainly attributed to the higher volume of entrapped air and the increased shrinkage during die filling (50).

One of the main aspects that influences the choice of the appropriate melt flow velocity is the gate thickness, as an increase in this thickness would require a slower velocity to avoid the turbulent flow of the melt into the die (51). Based on these remarks, it is safe to say that defining a suitable melt flow velocity is critical for the success of the RheoMetal™ operation.

Similar to HPDC, the melt flow velocity in the RheoMetal™ process can be represented in terms of either the gate velocity or the piston velocity. A representation of the maximum gate velocity in the 2nd phase (die filling) for each gate thickness is shown in *Table 2.4*.

2. Theoretical background and state of the art

Table 2.4 : The gate thickness-gate velocity correlation for the RheoMetal™ process (source: RheoMetal AB).

Gate thickness (mm)	Maximum gate velocity (m/s)
2	9
4	5
6	4
8	3.5
10	3
>10	2

The piston velocity can be derived from the gate velocity based on the following formulas:

$$\text{Piston to gate ratio} = \frac{\text{Cross sectional area of the piston}}{\text{Cross sectional area of the gate}} \quad (2.1)$$

$$\text{Cross sectional area of the gate} = \text{Width}_{\text{gate}} * \text{Thickness}_{\text{gate}} \quad (2.2)$$

$$\text{Cross sectional area of the piston} = \pi^2_{\text{piston}} \quad (2.3)$$

$$\text{The Piston speed} = \frac{\text{Max gate speed}}{\text{piston to gate ratio}} \quad (2.4)$$

➤ Intensification pressure

Due to the laminar flow of the slurry, the significance of the intensification pressure for the RheoMetal™ process is considered to be lower than for the HPDC process.

Regardless of the above statement and to ensure consistently low porosity contents, a similar value of the intensification pressure was still assigned in this thesis for the HPDC trials and the RheoMetal™ trials, which were conducted at the same supplier.

2.4.3.3 Factors affecting the RheoMetal™ process

In addition to the RheoMetal™ process' parameters, there are a number of other factors that can affect the mechanical properties of the cast part by varying the size and the fraction of the primary globular α -Al phase (α_1 -Al phase) that develops during the semi-solid slurry making process.

The main factors, which were found to be effective for the A356 (AlSi7Mg0.3) alloy are (52):

2. Theoretical background and state of the art

- The rotation speed of the EEM

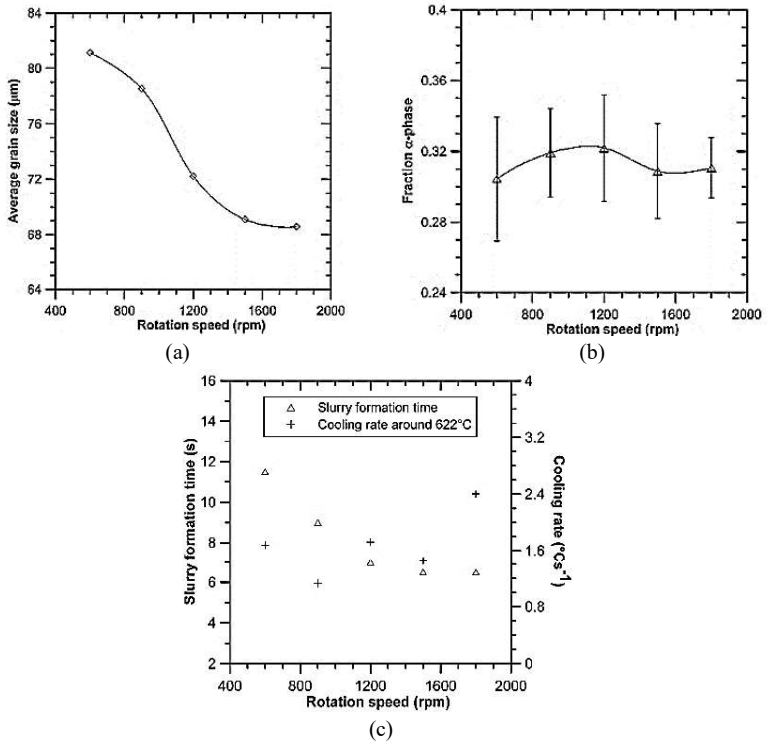


Figure 2.22: The influence of the rotation speed on the (a) average size of the α_1 -Al phase, (b) the fraction of the α_1 -Al phase, (c) the slurry formation time and the cooling rate.

As shown in *Figure 2.22*, there is an inverse relation between the rotation speed of the EEM and the size of the α_1 -Al phase. Similarly, the slurry formation time is found to decrease with increasing the rotation speed. This later observation can be linked to the faster dissolution of the EEM and the increased convection between the superheated melt and the EEM.

Unlike the above observations, no significant effect on the fraction of the α_1 -Al phase is experienced by varying the rotation speed. In addition, there is no detected correlation between the rotation speed and the cooling rate.

2. Theoretical background and state of the art

➤ The melt superheat

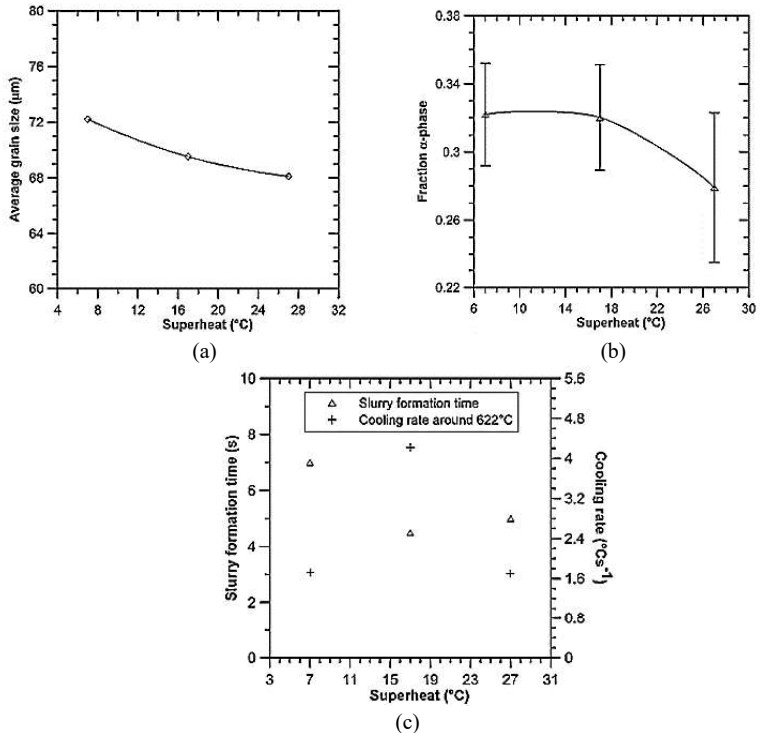


Figure 2.23: The influence of the melt superheat on the (a) average size of the α_1 -Al phase, (b) the fraction of the α_1 -Al phase, (c) the slurry formation time and the cooling rate.

Increasing the melt superheat, which is the difference between the temperature of the melt before inserting the EEM and the liquidus temperature, is found to cause a reduction in the fraction of the α_1 -Al phase due to the rise in the steady state temperature of the melt. In addition, a reduction in the average size of the α_1 -Al phase is also experienced with increasing the melt superheat.

On the contrary to the above outcomes, no correlation between the superheat, the slurry formation time and the cooling rate could be obtained.

2. Theoretical background and state of the art

- The combined effects of the added EEM amount (%EEM) and the melt superheat

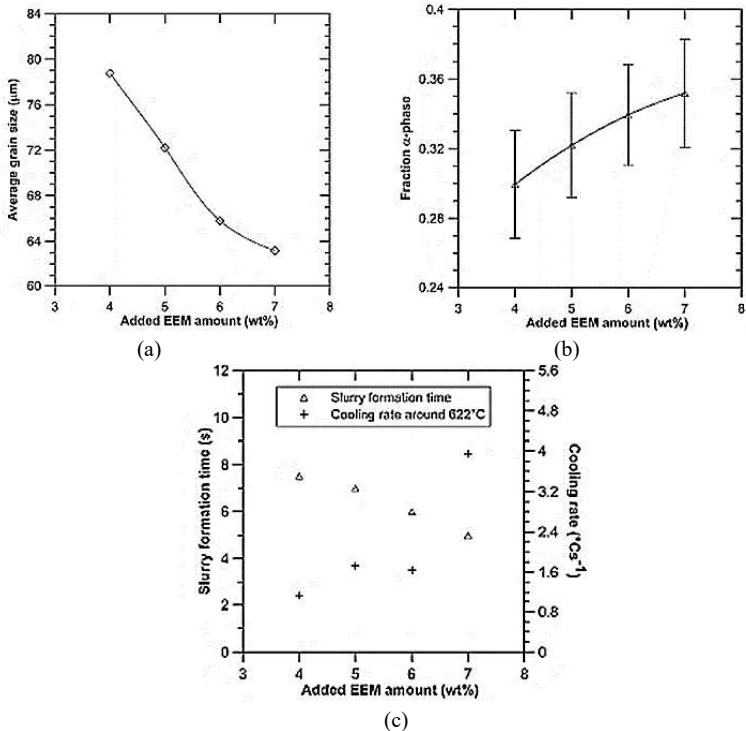


Figure 2.24: The combined influence of the melt superheat and the EEM amount on (a) the average size of the α_1 -Al phase, (b) the fraction of the α_1 -Al phase, (c) the slurry formation time and the cooling rate.

The largest beneficial influence on the mechanical properties is found to be caused by the combined effects of increasing the %EEM and the melt superheat due to the following reasons:

- Increasing both factors is found to cause a reduction in the slurry formation times. This outcome might be due to the faster dissolution of the EEM, as a result of the large superheat, in addition to the increase in the cooling effect as a result of the bigger EEM.

2. Theoretical background and state of the art

- Although increasing the superheat alone is expected to decrease the fraction of the α_1 -Al phase, a contradicting outcome is obtained by coupling this increase in the superheat with an increase in the %EEM.
- A reduction of the average grain size is detected by using this combination.

2.4.3.4 The typical defects

In comparison to HPDC, RheoMetalTM has a number of differences in terms of the possible casting defects. This can be contributed to several reasons such as the melt's behaviour, the applied process parameters and the casting conditions.

The main defect in the RheoMetalTM process is Macrosegregation. This defect can be divided into (49):

- Transverse segregation, which can evolve from the localized shear bands (53), in the form of porosity bands or eutectic rich bands (positive macrosegregation) as seen in *Figure 2.25*. The amount of the alloying elements and the feeding ability of the remaining liquid phase into the shear bands are the two main factors that play a role in the development of either the porosity bands or the eutectic rich bands.

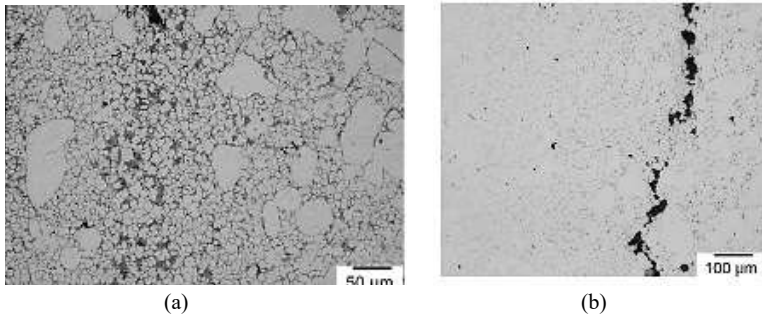


Figure 2.25: (a) Eutectic rich bands and (b) porosity bands that can develop in Rheocast parts (54).

- Longitudinal segregation, which evolves due the development of solute lean (α_1 -Al) and solute rich (α_2 -Al) phases at different regions of the microstructure. This defect causes an increase in the inhomogeneity and can lead to different mechanical properties and thermal conductivity responses at different regions of the cast part.

An example of this defect is shown in *Figure 2.26*, where the larger α_1 -Al particles, which are formed during the slurry making process, are concentrated in the area near the gate. On the contrary, the smaller and more solute rich α_2 -Al particles, that are formed as a result of

2. Theoretical background and state of the art

the very fast cooling rate of the enriched liquid phase in the die, are concentrated in the area near the vent.

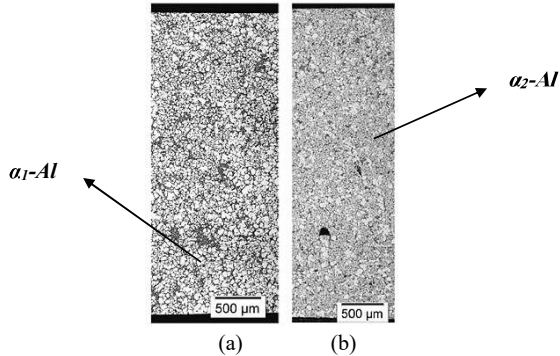


Figure 2.26: The microstructure of a rheocast radio filter (a) near the gate and (b) near the vent (49).

In comparison to HPDC, RheoMetal™ results in:

- Less gas porosities due to the laminar flow of the semi-solid slurry.
- Less microsegregation due to the homogenisation of the α_1-Al particles that takes place during the slurry making process (49).

2.5 The aluminium alloys for structural automotive castings

Although pure aluminium has excellent corrosion resistance and superior electrical conductivity, it does not acquire enough strength to be used for structural applications. Therefore, depending on the required properties, a combination of different alloying elements should be incorporated into the aluminium composition to increase its strength and to facilitate its use in different applications.

The suitable aluminium alloys for the structural automotive castings can be divided into two main groups. The alloying elements involved and the main properties of each of those groups are represented in *Table 2.5* as follows.

Table 2.5: The main aluminium alloy families for structural automotive castings (26).

Alloy family	Properties
Al-Si (Al+4-12%Si+0-0.6%Mg+Mn+Fe)	<ul style="list-style-type: none">• Properties can be enhanced via heat treatment.• Characterized by having excellent castability.• Leads to a long die life in the range of 80000 to 100000 shots.

2. Theoretical background and state of the art

Table 2.5 (continued.)

<p>Al-Mg-Si (Al+2-5.5%Mg+1.5-3%Si)</p>	<ul style="list-style-type: none"> • More difficult to cast due to the lower Si content. • Leads to a much shorter die life (40000 shots) due to the increased die soldering. • Properties are extremely dependant on the wall thickness. • Susceptible to hot tears and stress corrosion cracking (SCC).
---	---

A third group of alloys have been recently developed, but still not extensively used in the automotive industry. This group of alloys is the **Al-Mg-Fe alloy family**, which offers excellent as-cast mechanical properties, and which can, due to its negligible silicon content, facilitate the dyeing of the cast part via the anodization process (55). However, the alloys that belong to this family are more difficult to cast and experience higher shrinkage values, due to the small volume fractions of their eutectic.

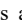
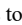
















The main alloying elements in *Table 2.5* have different impacts on the strength and the ductility of the aluminium castings. These impacts are shown in *Table 2.6*, where  refers to an enhancement in the property and  refers to its depreciation.

Table 2.6: The effects of the different alloying elements on the strength and the ductility of the high-integrity aluminium castings (24) (37) (56) (57) (58) (59) (60).

Alloying element	Strength	Ductility
Si		
Mg		
Mn	 *	 *
Cu		
Fe		
Ti		
Sr		
Zr		

* only for Mn/Fe ratio of ~ 1.2

Other than their impacts on the mechanical properties, the alloying elements affect the casting behaviours of the different aluminium alloys by influencing their solidification intervals, fluidity/castability and their resistance against die soldering.

For the different aluminium casting alloy families, the two main alloying elements that contribute to the resistance against die soldering are Fe and Mn (26).

2. Theoretical background and state of the art

On the other hand, and as shown below, different alloying elements are needed to impact the solidification interval and the fluidity of each family of alloys.

➤ For the Al-Si alloy family:

- The solidification interval of the hypoeutectic Al-Si alloys is affected by varying the Si content. As shown in *Figure 2.27*, increasing the Si content leads to a reduction in the solidification interval.

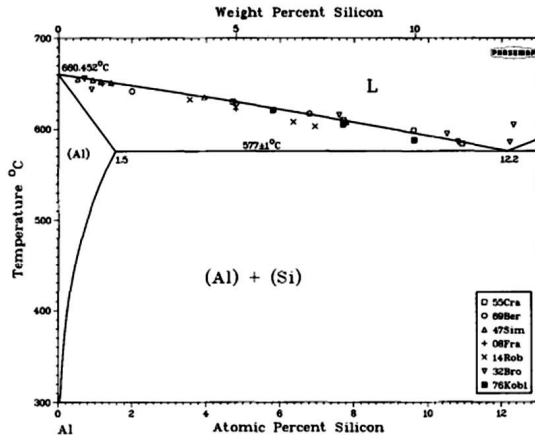


Figure 2.27: The hypoeutectic Al-Si phase diagram (61).

- As stated in Table 2.5, the fluidity of any alloy within this group improves by increasing the Si content. This statement can be, as seen in *Figure 2.27*, linked to the reduction in the liquidus temperature at larger Si contents.

In addition, and according to (62), the fluidity of the Al-Si alloys can be further enhanced by decreasing the Fe and Sr contents. This can be traced back to the decrease in the Fe intermetallics and the Cu containing phases that hinder the flow by filling the interdendritic pathways.

➤ For the Al-Mg-Si alloy family:

- Similar to the Al-Si alloys, increasing the Si content of the Al-Mg-Si alloys leads to a reduction in the solidification interval (57).
- According to (57), the fluidity of the Al-Mg-Si alloys are enhanced by increasing the Si and the Mg contents due to their role in decreasing the liquidus temperature.

2. Theoretical background and state of the art

Choosing an alloy, from each of the above-mentioned families, shall take into consideration the solidification interval requirement of each casting process. In the case of HPDC, an alloy with a narrow solidification interval is needed for an increased fluidity and thus an increased productivity of thin walled and complex shaped castings (49) (57) (63). Whereas a larger solidification interval is needed for the RheoMetal™ process to enable the production of a stable semi-solid slurry from the liquid melt (49). According to the company *RheoMetal AB*, the ideal solidification interval for the RheoMetal™ casting process lies in the range of 35-50 K.

2.6 Heat treatments

Heat treatment is the process of subjecting the cast part to a series of temperature fluctuations for the aim of achieving further enhancements to its mechanical properties.

T5, T6 and T7 are typical heat treatment processes that can lead to different impacts on the mechanical properties of the aluminium castings by causing distinct changes to the alloys' microstructures (64) (65) (66). These heat treatments are made up of several stages as shown in *Figure 2.28*.

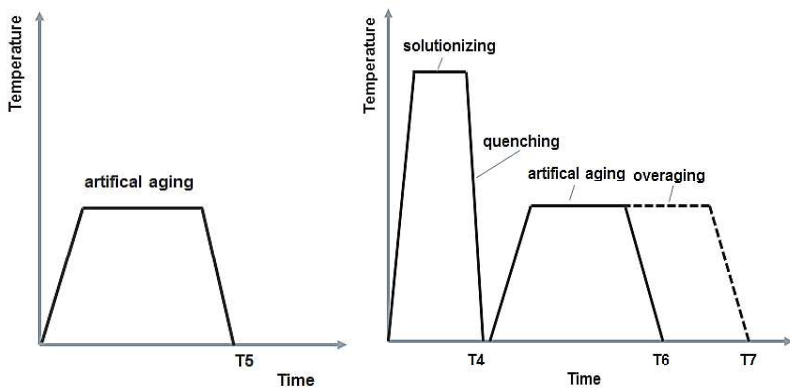


Figure 2.28 : The time - temperature graphs of the different heat treatments.

As seen in *Figure 2.28*, T5 requires cooling the part after casting, followed by an aging treatment. T6 on the other hand, requires the extra step of solution heat treatment to be done prior to the quenching and aging steps. Similarly, T7 involves a solution heat treatment step. However, it differs from the T6 heat treatment in terms of the duration and/or the temperature upon which the aging treatment is done.

3. Cost calculation study

3 Cost calculation study

In order to fulfil the aim of reaching a cost-efficient process route for the mass production of thin walled structural aluminium body castings, it was important to determine the impacts of several factors such as the type of the HPDC machine, the alloy and its required heat treatment process, the application of the vacuum condition, the die life and the casting process on the cost of such castings. The significance of this step, which was carried out, as illustrated in this chapter, via a cost calculation study, lied in its ability to direct the research, during the scope of this thesis, towards the factors with the largest cost reduction potentials.

As seen in *section 2.1*, there are a number of different aluminium castings that can be integrated in the car body structures. In this thesis, the 2020 Ford explorer aluminium shock tower in *Figure 3.1*, with the total weight of 4 Kg, was the one chosen for the cost analysis.

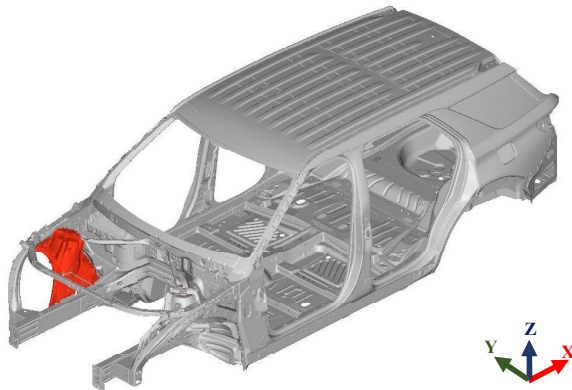


Figure 3.1: An aluminium shock tower (red) in the 2020 Ford explorer's body.

For the cost calculation study, only one HPDC machine was assumed to produce the total required stock of 1,320,000 parts. In addition, the labor costs were in alliance with the standard wages in Germany.

3.1 Cost estimation of the parts produced using the HPDC process

As mentioned earlier, different factors were considered for the cost calculation study. Varying those factors has led to 24 different scenarios for the production of the 2020 Ford explorer aluminium shock tower by the HPDC process, as seen in *Table 3.1*.

3. Cost calculation study

Table 3.1: The cost calculation scenarios

Scenario	Type of machine	Alloy	Vacuum	Heat treatment	Die life (shots)
1 st	Single tool	AlSi10MnMg	Not applied	T7	80000
2 nd	HPDC		Applied		
3 rd	Double tool		Not applied		
4 th	HPDC		Applied		
5 th	Single tool		Not applied		100000
6 th	HPDC		Applied		
7 th	Double tool		Not applied		
8 th	HPDC		Applied		
9 th	Single tool		Not applied		130000
10 th	HPDC		Applied		
11 th	Double tool		Not applied		
12 th	HPDC		Applied		
13 th	Single tool	AlSi9MnMoZr	Not applied	- (As-cast (F))	80000
14 th	HPDC		Applied		
15 th	Double tool		Not applied		
16 th	HPDC		Applied		
17 th	Single tool		Not applied		100000
18 th	HPDC		Applied		
19 th	Double tool		Not applied		
20 th	HPDC		Applied		
21 st	Single tool		Not applied		130000
22 nd	HPDC		Applied		
23 rd	Double tool		Not applied		
24 th	HPDC		Applied		

The cost analysis was then conducted for each of the above-mentioned scenarios using a cost calculation tool. The derived outcomes were then compared together to give an indication about the influence of each of the considered factors on the cost of the shock tower.

The calculation tool

This tool was originally obtained from the Swiss high pressure die casting machines' supplier *Bühler AG*, to help carry out the aimed cost study.

The expenses of investment, capacity of installation and exploitation costs of installation are the three main sections of this tool.

3. Cost calculation study

Each of these sections consists of a number of aspects that had to be accurately chosen, according to the relevant scenario, in order to precisely estimate the cost of the shock tower.

➤ Expenses of investment

This section is mainly concerned with the costs of the machines and the different units and equipment that are required for the high pressure die casting (HPDC) process.

Expenses of investment

Type of machine	C 220 DL	▼	
Type of installation	Standard cell	▼	
Dosing	BuhlLadle 2/23	▼	
Extraction & handling	BuhlRob 6600	▼	Quantity 1 ▼
Thermoregulation	Tooltemp 380 1K	▼	Quantity 4 ▼
Spraying	BuhlSpray 3 B 8/4	▼	
Trimming	Tecnopres KZP 60	▼	
Cooling	Reis 1500 / 1000 / 1000 (Gr	▼	
Exhausting hood	KMA 8004	▼	
Holding furnace (Al)	Stotek Stotherm 1200	▼	
Duration of depreciation			12 years
Annual interests			5 %

Figure 3.2: The outline of the expenses of investment's section in the calculation tool.

In the case of a single tool HPDC process, the inputs in *Figure 3.2* were defined based on the following reasons:

- The C220DL was chosen, because it is a two-platen machine that can deliver an intensified injection force of approximately 173 tons (67), and therefore is suitable for the production of the 4 kg shock tower.
- For an accurate calculation of the costs, the standard cell was chosen as the type of installation.

3. Cost calculation study

- For dosing, the Buhlladle 2/23, was chosen because of its suitability to the C220DL machine, and because it can handle the weight of the aluminium alloy (67).
- For extraction and handling, a single BuhlRob 6600 was selected from the available choices due to its similarity to the Model 6700F / 205-2.8 (67), which can be used with the C220DL machine.
- For precise thermoregulation, 4 Tooltemp 380 1K tempering units were chosen.
- For spraying and trimming, the Buhlspray 3B 8/4 (67) and the Tecnopress KZP 60 (68) were the suitable choices.
- Reis 1500 /1000 /1000 was the considered cooling bath for quenching and KMA 8004 (69) was the selected exhausting hood.
- For the holding furnace, Stotek stotherm 1200, which corresponds to the STE 1210 model (70), was considered as a suitable furnace choice in this case.
- The duration of depreciation and the annual interests were given the respective values of 12 years and 5 %.

In the case of a double tool HPDC process, most of the above entries were kept the same, except for the following change:

Type of machine:

The V320NL machine was chosen in this case, since its 3200 tons' press can produce two shock towers per shot (67).

➤ **Capacity of installation**

This section is related to the outcome and the capacity of the installed HPDC machine.

- ❖ For the single tool HPDC machine, where no vacuum condition is applied, the following values were defined:

Working days per year	240
Shifts per day	3
Hours per shift	8
Percentage of annual time allocated	100%
Utilization rate	80%

3. Cost calculation study

Number of shots per hour	51
Number of parts per die	1
Reject rate after casting	3.5%
Reject rate after machining	1.5 %

The above input values were defined according to the following criteria:

- The 240 working days per year were based on the assumption that the machine is operated for 5 days a week, and that it is shut down for 4 weeks due to holidays.
- The utilization rate was considered to be equal to 100% - downtime%.
- The percentage of annual time allocated was regarded to be equal to the ratio between the planned productions per year and the total good parts produced per year.
- The number of shots per hour were equal to 51 due to the 70 seconds cycle time.

❖ For the double tool HPDC machine:

Working days per year	240
Shifts per day	3
Hours per shift	8
Percentage of annual time allocated	100%
Utilization rate	76%
Number of shots per hour	46
Number of parts per die	2
Reject rate after casting	4%
Reject rate after machining	1.5%

From the above entries, it is obvious that the inputs for the single tool were kept the same except for the following changes:

- The number of parts per die was changed to 2.
- The utilization rate was decreased due to the larger downtime%.
- The number of shots per hour were equal to 46 due to the slower cycle time (78 seconds).
- The reject rate after casting was increased to 4 %.

3. Cost calculation study

➤ **Exploitation costs of installation**

This section includes other process related costs such as the energy costs, personal costs, maintenance costs, dies and tools costs, metal cost and machining costs.

- ❖ Some of these costs are not dependent on the alloy nor on the HPDC machine. Those costs were always kept constant and were given the following values:

Energy costs

Electrical energy cost per kW/h	0.070 €
Miscellaneous energy cost per utilized hour	8.65 €

Ancillary materials

Cost per net utilized hour	9.55 €
----------------------------	--------

Repair and maintenance

Material and outside services per utilized hour	10.00 €
Inside services per utilized hour	7.98 €

Personnel costs

Operator cost per gross utilized hour	60.00 €
Operators per installation	50 %

Overhead costs per year

Cost per square meter	150 €
Administrative expense portion	200,000 €

- ❖ The costs, which depend on the alloy, are the metal cost, metal in return (waste) cost, peripheral work costs and machining costs. The values given to these costs were derived based on the following points:

- The alloy prices (metal cost) in all the different scenarios were based on *Aluminium Rheinfelden GmbH*'s price list for the month of January 2019.

It must be noted that the alloy prices are continuously fluctuating. This observation is demonstrated clearly in *Figure 3.3*, which illustrates the price of the aluminium alloys in the period from January 2016 to December 2019.

3. Cost calculation study



Figure 3.3: The aluminium alloy prices per ton in \$ from January 2016 till December 2018 according to the *London Metal Exchange* (modified from (71)).

- The weight of the runners and overflows was considered to be equal to $70\% * \text{as-cast weight} * \text{number of parts per die}$. (3.1)
- The price of metal in return was considered to be equal to 95 % of the alloy's price.
- For the peripheral work and machining costs subsections, the estimated values of the inputs, which were obtained from *NewAlu GmbH*, were based on considering the use of automated deburring robots for polishing, grinding and trimming the parts. In addition, a continuous furnace, with a capacity of 9 parts per batch, was considered for heat treatment. Furthermore, the quality assurance was observed by testing three tensile samples per day. Moreover, the additional costs of machining, washing, gauging and straightening the parts were added to this section based on considering the use of machining centers, automated washing machine and an automated straightening line respectively.

3. Cost calculation study

In the case of the AlSi10MnMg-T7 alloy-heat treatment combination, the following values were defined to the above-mentioned costs:

Production costs

Metal cost

Alloy price per kg	2.70 €
Melting cost per kg	0.3 €

Matter return

Price of metal in return (waste)	2.57 €
As-cast weight per casting	4000 g
Weight of runners & overflows	2800 g
Melt losses	6.5 %
Overheads of metal relating to the weight used	2.5 %

Peripheral work

Polishing, trimming, grinding per part	3.59 €
Heat treatment per part	6.35 €
Quality assurance per part	0.20 €
Other secondary operations costs per part	3.32 €

Machining costs

Machining cost per part	5.340 €
-------------------------	---------

3. Cost calculation study

In the case of the AlSi9MnMoZr alloy, where no heat treatment is required, the following values were defined:

Production costs

Metal cost

Alloy price per kg	3.16 €
Melting cost per kg	0.3 €

Matter return

Price of metal in return (waste)	3 €
As-cast weight per casting	4000 g
Weight of runners & overflows	2800 g
Melt losses	6.5 %
Overheads of metal relating to the weight used	2.5 %

Peripheral work

Polishing, trimming, grinding per part	3.59 €
Heat treatment per part	0 €
Quality assurance per part	0.20 €
Other secondary operations costs	3.32 €

Machining costs

Machining cost per part	5.340 €
-------------------------	---------

3. Cost calculation study

- ❖ The costs of the dies and tools depend on the type of the HPDC machine, single tool or double tool, and on the die life.

The values given to all the entries in this section were calculated according to an iterative approach due to the difference between the defined die lives and the required total number of good parts. The inputs for these calculations were obtained from *Heck+Becker GmbH& CO. KG*.

- The first die cost, which is equal to the sum of the die build cost (die cost + cavity replacement cost) and the expenses governing the change of the die after its total wear, was calculated according to the following formula:

$$\text{First die cost} = \text{Die build} + \text{Sampling \& validation} + \text{Die design} + \text{Process development} + \text{Shot sleeve} + \text{Piston} + (\text{Die build} - \text{Cavity replacement}) \quad (3.2)$$

- The replacement die insert cost, which is considered to be equal to the expenses regarding the replacement of the die insert with a new one after it can no longer be used, was calculated according to the following formula:

$$\text{Replacement die insert cost} = \text{Cavity replacement} + \text{Sampling \& validation} + \text{Shot sleeve} + \text{Piston} \quad (3.3)$$

- The lifetimes of the shot sleeve and the piston are independent from that of the die insert and the die. In this cost study, their lifespan was assumed to be 100,000 shots. Therefore, the above formulas were adjusted accordingly for the scenarios with different die lives e.g. $[0.8 * (\text{shot sleeve} + \text{piston})]$ was used for the 80,000 shots' scenarios and $[1.3 * (\text{shot sleeve} + \text{piston})]$ was implemented for the 130,000 shots' scenarios.

- The other entries were calculated according to the upcoming formulas:

$$\text{Die maintenance \& repair per die} = \text{TR\&R} * \text{Die life} \quad (3.4)$$

$$\text{Trimming tool costs} = \text{Trim die build cost} + \text{Trim die design cost} \quad (3.5)$$

$$\text{Scrap} = \text{Total N}^\circ \text{ of shots} * \left(\frac{\text{Reject rate after casting} + \text{Reject rate after machining}}{100} \right) \quad (3.6)$$

$$\text{Total N}^\circ \text{ of good parts} = \text{Total N}^\circ \text{ of produced parts} - \text{Scrap} \quad (3.7)$$

$$\text{Total N}^\circ \text{ of produced parts} = \text{Total N}^\circ \text{ of shots} * \text{N}^\circ \text{ of parts per shot} \quad (3.8)$$

3. Cost calculation study

- The total replacement die inserts cost was calculated automatically by the cost calculation tool according to the following equation:

$$\text{Total replacement die insert cost} = \text{Replacement die insert cost} * \text{N}^{\circ} \text{ of dies} \quad (3.9)$$

The number of dies, from the above formula, were calculated as follows:

$$\text{N}^{\circ} \text{ of dies} = \frac{\text{Total N}^{\circ} \text{ of produced parts}}{\text{Die life}} - \text{N}^{\circ} \text{ of parts produced by the first die} \quad (3.10)$$

In the case of a single tool HPDC machine with a die life of 80,000 shots and where no vacuum condition is applied, the following values were derived:

DIES AND TOOLS

First die cost	535,440 €
Replacement die insert cost	215,440 €
Die maintenance and repair per die	136,000 €
Die life	80,000 Shots
Total good parts per machine through product life cycle	1,320,000 Castings
Trimming tool costs	63,000 €

For the double tool HPDC machine, the same concept and formulas for calculating the costs were used. In the case of a double tool HPDC machine with a die life of 80,000 shots and where no vacuum condition is applied, the following values were derived:

DIES AND TOOLS

First die cost	798,440 €
Replacement die insert cost	368,440 €
Die maintenance and repair per die	168,000 €
Die life	80,000 Shots
Total good parts per machine through product life cycle	1,320,000 Castings
Trimming tool costs	85,000 €

3. Cost calculation study

- ❖ The integration of vacuum in the HPDC process is regarded, as illustrated in the following points, to have an influence on the overall cycle time, as well as on the costs of the dies and the die inserts:
 - The increase in the cycle time, due to the application of the vacuum condition, was thought to be mainly caused by the extra step of evacuating the air from the die. For the conducted calculations, this evacuation time was considered to be in the range of 1.5 – 2.5 s for each cycle (72).
 - The scrap rate (*reject rate after casting + reject rate after machining*) was considered to be reduced by 1 % after applying vacuum.
 - The additional costs of the vacuum system and the venting components had to be integrated into the first die cost and the replacement die insert cost.

Some of the components of the vacuum and venting systems were only integrated once in the costs, as they are not limited to a certain number of shots. These components are referred to as the single-entry items and they are comprised of the costs of the complete vacuum system (e.g. the TopVac 1000_1/2 complete vacuum system), the piston spraying cost, the costs of small parts (e.g. fittings and cables) and the training, service and installation costs.

Other components were considered to have a limited lifetime of 100,000 shots. These components, the replaceable items, include the chill vents, mesh vents, the vacuum shot sleeve and the vacuum piston.

The costs of the single entry and replaceable items were integrated in the first die cost and the replacement die insert cost as follows:

$$\text{First Die cost} = \text{Die build} + \text{Sampling \& validation} + \text{Die design} + \text{Process development} + \text{Total of single entry items} + \text{Total of replaceable items} + (\text{Die build-Cavity replacement}) \quad (3.11)$$

$$\text{Replacement die insert cost} = \text{Cavity replacement} + \text{Sampling \& validation} + \text{Total of replaceable items} \quad (3.12)$$

In the case of different die lives and like the non-vacuum scenarios, the above formulas were also adjusted based on each die life. For the 80,000 shots' scenarios, the *Total of replaceable items* entry was replaced by $[0.8 * (\text{Total of replaceable items})]$. On the other hand, for the 130,000 shots' scenarios, $[1.3 * (\text{Total of replaceable items})]$ was used.

3. Cost calculation study

The best-case and worst-case approaches

The cost per part, calculated using the approaches mentioned in the previous section, resembled the realistic outcome of each scenario.

For a more accurate analysis of the results, best and worst-case versions of each scenario were also developed.

The changes done to the different inputs of the calculation tool, in the case of the best-case and the worst-case versions, are clarified in *Table 3.2* as follows.

Table 3.2: The scenarios' best and worst-case versions.

Worst case version	Best case version
<u>Expenses of investment section:</u> <ul style="list-style-type: none"> • Duration of depreciation = 10 years 	<u>Expenses of investment section:</u> <ul style="list-style-type: none"> • Duration of depreciation = 14 years
<u>Capacity of installation section:</u> <ul style="list-style-type: none"> • Working days per year = 44 weeks * 5 days per week = 240 days. (8 weeks off instead of 4) • Utilization rate = 5 % lower than the realistic version. • Cycle time = 5 seconds more than the realistic version. • Reject rate after casting = 0.5 % more than the realistic version. • Reject rate after machining = 0.5 % more than the realistic version. 	<u>Capacity of installation section:</u> <ul style="list-style-type: none"> • Working days per year = 48 weeks * 6 days per week = 288 days. • Utilization rate = 5 % more than the realistic version. • Cycle time = 5 seconds less than the realistic version. • Reject rate after casting = 0.5 % less than the realistic version. • Reject rate after machining = 0.5 % less than the realistic version.
<u>Exploitation costs of installation section:</u> <ul style="list-style-type: none"> • Operators per installation =100% (One operator per machine) 	<u>Exploitation costs of installation section:</u> <ul style="list-style-type: none"> • Operators per installation =33% (One operator for every three machines)

The outcomes of the cost calculation scenarios in *Table 3.1:* are illustrated in *Table 3.3* as follows.

3. Cost calculation study

Table 3.3: The worst, realistic and best case outcomes of the cost calculation scenarios.

Scenario from <i>Table 3.1</i>	Cost per part (€)		
	Worst case	Realistic case	Best case
1 st	45.57	43.47	42.56
2 nd	45.84	43.72	42.51
3 rd	42.7	41.32	40.44
4 th	42.84	41.44	40.56
5 th	45.11	43.02	41.83
6 th	45.40	43.29	42.08
7 th	42.08	40.70	39.83
8 th	42.22	40.83	40.16
9 th	44.65	42.56	41.38
10 th	44.95	42.84	41.64
11 th	41.92	40.55	39.68
12 th	42.08	40.69	39.81
13 th	41.46	39.36	38.15
14 th	41.73	39.60	38.39
15 th	38.60	37.21	36.32
16 th	38.73	37.33	36.43
17 th	41.01	38.91	37.71
18 th	41.29	39.17	37.96
19 th	37.98	36.59	35.71
20 th	38.11	36.71	35.82
21 st	40.55	38.45	37.25
22 nd	40.84	38.72	37.51
23 rd	37.83	36.44	35.56
24 th	37.98	36.58	35.59

Intermediate conclusions:

A few conclusions were derived after comparing between the outcomes of the different scenarios in *Table 3.3*.

- *The effect of the type of the HPDC machine*

By comparing between the outcomes of the 1st and 3rd scenarios, and between the 17th and 19th scenarios, it was evident that using a double tool HPDC machine instead of a single tool HPDC machine can lead to a lower cost per part. This cost reduction was the second largest and lied in the range of 2 – 3 € per part. Hence, it would be of a great benefit to consider the use of double tool HPDC machines in the production of the shock tower. For this suggestion to be possible, suitable feeding materials and die designs should be used.

3. Cost calculation study

- *The combined effects of the alloy and heat treatment*

By comparing between the 2nd and the 14th scenarios' outcomes and between the 8th and the 20th scenarios' outcomes, a cost reduction in the range of **4.1 - 4.3 €** was observed. This large cost reduction per part was the result of eliminating the heat treatment costs by using the AlSi9MnMoZr alloy, which doesn't require heat treatment to reach the desired mechanical properties of the 2020 Ford explorer shock tower, instead of the AlSi10MnMg alloy that require an expensive T7 heat treatment process (2).

- *The effect of applying vacuum*

From the comparisons between the outcomes of the 5th and 6th scenarios and the 11th and 12th scenarios, it is concluded that applying the vacuum condition in the HPDC process is essential, not only because of its role in enhancing the overall part's quality, but also because it only results in a minor increase in the investment costs, such as the **29 cents** per part in this study.

- *The effect of the die life*

To test the influence of this factor on the shock tower's cost, three different die lives were taken into consideration. By comparing between the outcomes of the different die life's scenarios (e.g. 130000 shots and 80000 shots) and due the recorded difference of **0.86 – 0.89 €**, it is concluded that an increase in the life span of the die can cause a reduction in the cast part's cost.

From the above conclusions and due to the large impact of the heat treatment on the cost reduction potential, determining the suitable alloy or alloys, which can fulfill the required mechanical properties of the structural body parts in the as-cast state, was considered to be vital towards reaching the aim of a cost-efficient process route for the mass production of structural aluminium body castings. In addition, investigating the suitable means that can contribute towards a longer die life, such as the use of the RheoMetal™ process in the production of the desired castings, was regarded as a beneficial step that can help in achieving the thesis' aim.

3.2 Cost estimation for the parts produced using the RheoMetal™ process

Due to the resultant enhanced properties and the numerous advantages of the RheoMetal™ process, it was important to investigate whether or not it can be implemented for the cost-efficient production of the structural body parts. For this purpose, a cost calculation scenario had to be done to estimate the cost of producing the structural body parts, in this case the 2020 Ford explorer shock tower, via the RheoMetal™ process.

3. Cost calculation study

For the sake of obtaining a representable RheoMetal™'s cost calculation scenario, suitable values had to be assigned to the process variables in *Table 3.4*. These values were derived after conducting a comparison, as shown in *Table 3.4*, with the 4th scenario in *Table 3.1*.

Table 3.4: The comparison between the studied HPDC and RheoMetal™ scenarios and their assigned process variables.

Process variables	HPDC		RheoMetal™	
Alloy price (€)	+	2.7	++	3.06
Heat treatment cost (€)	(+)	6.35	(--)	0
Price of metal in return (€)	+	2.57	++	2.91
Melt losses (%)	+	6.5	(-)	3
Utilization rate (%)	+	76	(-)	70
Number of shots per hour	+	45	(-)	42
Reject rate after casting (%)	+	3.5	(-)	1.5
Reject rate after machining (%)	+	1	(-)	0.5
Die life (shots)	+	80000	+++	130000
Weight of runners and overflows (g)	+	5600	(++)	6400

+: Reference value, (-): Lower than, (--): Not applied, (+): Applied, ++: Higher than, +++: Longer than and (++): Larger than.

As shown in *Table 3.4*, each of the investigated casting processes was expected to have a different value for each process variable. The reasons beyond these projected differences are addressed in the following bullet points:

- The AlSi10MnMg alloy, which needs a T7 heat treatment to reach the required mechanical properties of the 2020 Ford explorer shock tower, was the chosen alloy for the HPDC scenario. For the RheoMetal™ scenario on the other hand, the AlMg5Si2Mn alloy, which does not require heat treatment to reach the desired properties, was regarded to be the more suitable alloy. The costs of both alloys per kg were obtained from *Aluminium Rheinfelden GmbH's* price list for the month of January 2019.
- Due to the direct proportionality between the die soldering and the casting temperature (73), a lower percentage of the melt losses was considered for the RheoMetal™ scenario.
- Due to the larger downtime% in the RheoMetal™ process, a lower utilization rate was defined for its cost calculation scenario.
- Less number of shots per hour were defined for the RheoMetal™ scenario. This choice was based on the slower injection velocity in this process, which, as mentioned earlier in *section 2.4*, makes sure that a laminar flow of the melt into the die is achieved.
- For the RheoMetal™ scenario, lower reject rates after casting and machining were taken into consideration due to the laminar flow of the melt in this process.

3. Cost calculation study

- A longer die life was specified for the RheoMetal™ scenario due to the lower temperature of the melt. This lower temperature has a positive impact on the die life as it results in less thermal fatigue cracking (74).
- Larger weights of the runners and the overflows were specified for the RheoMetal™ scenario. This is because of the thicker gates that are needed to allow the unrestricted flow of the thixotropic slurry into the die.

The breakdowns of the cost per part from the RheoMetal™ process scenario and the 4th scenario in *Table 3.3* (reference scenario) are represented in *Figure 3.4* as follows.

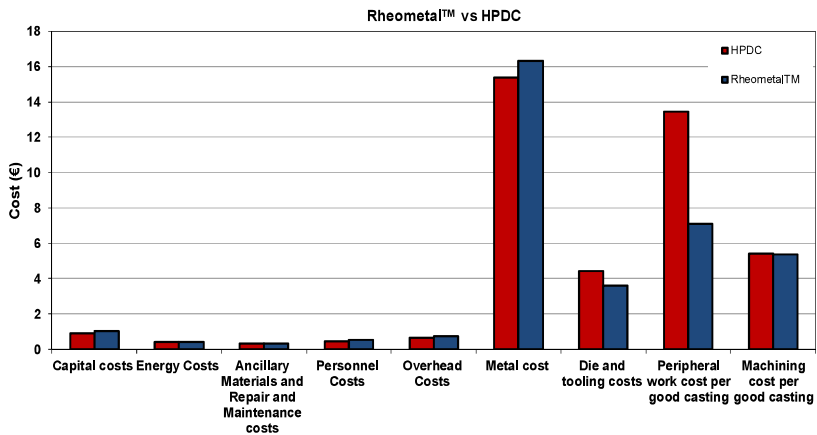


Figure 3.4: The cost per part breakdown chart according to the RheoMetal™ and the HPDC process scenarios.

From the cost per part breakdown chart in *Figure 3.4*, it is evident that the RheoMetal™ scenario had resulted in a more cost-efficient outcome (35.43 €) than the HPDC scenario (41.44 €). This difference in the cost per part can be attributed, as seen in *Figure 3.4*, to the peripheral work cost per good casting that includes, as mentioned earlier in *section 3.1*, the polishing, grinding, trimming, surface treatment, heat treatment, quality assurance and the secondary operations costs.

Intermediate conclusion:

- From the comparison chart in *Figure 3.4* and based on the values that were assigned to the process variables in *Table 3.4*, it is concluded that the RheoMetal™ process can offer a higher cost reduction potential than the HPDC process when used for the production of the structural car body parts.

4. Experimental approach

4 Experimental approach

As shown in *Chapter 3*, the conducted cost calculation study was based on the 2020 Ford explorer shock tower. Therefore, in order to obtain a cost-efficient process route for the mass production of this part (1,000,000-2,000,000 parts), it was vital to take its design and assembly requirements into consideration during the design of the experiments. In other terms and due to the difficulty of casting the investigated shock tower during the duration of this thesis, it was important to perform the different experimental trials on suitable alternatives, such as cast plates and parts, with similar thicknesses and preferably similar geometrical dimensions to those illustrated in *Figure 4.1*. In addition, and as the 2020 Ford explorer shock tower is assembled in the car body structure by self-piercing riveting, it was essential to test the response of the cast plates and parts to this joining mechanism and not to other joining mechanisms such as welding or adhesion.

Other quality and lifetime aspects of the shock tower such as its susceptibility to corrosion, the influence of the mold release agents on its KTL coating, the influence of the die soldering on its surface quality and its fatigue life were not investigated during the thesis.

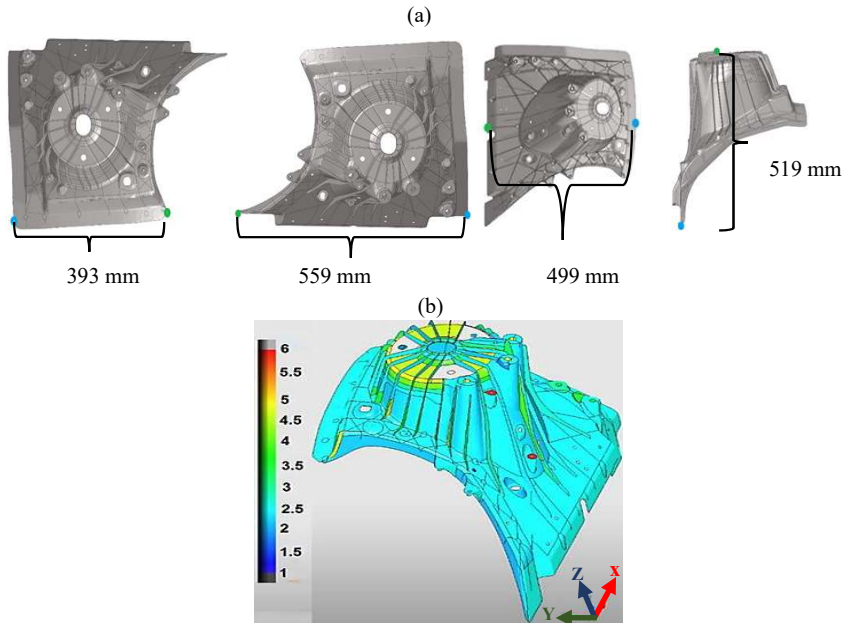


Figure 4.1: (a) The geometrical dimensions and (b) the thickness distribution (mm) of the 2020 Ford explorer aluminium shock tower.

4. Experimental approach

Based on the above considerations and by taking into account the other aspects that influence the cost efficiency of this part such as the choice of the alloy and the casting process, the experimental approach was defined as follows:

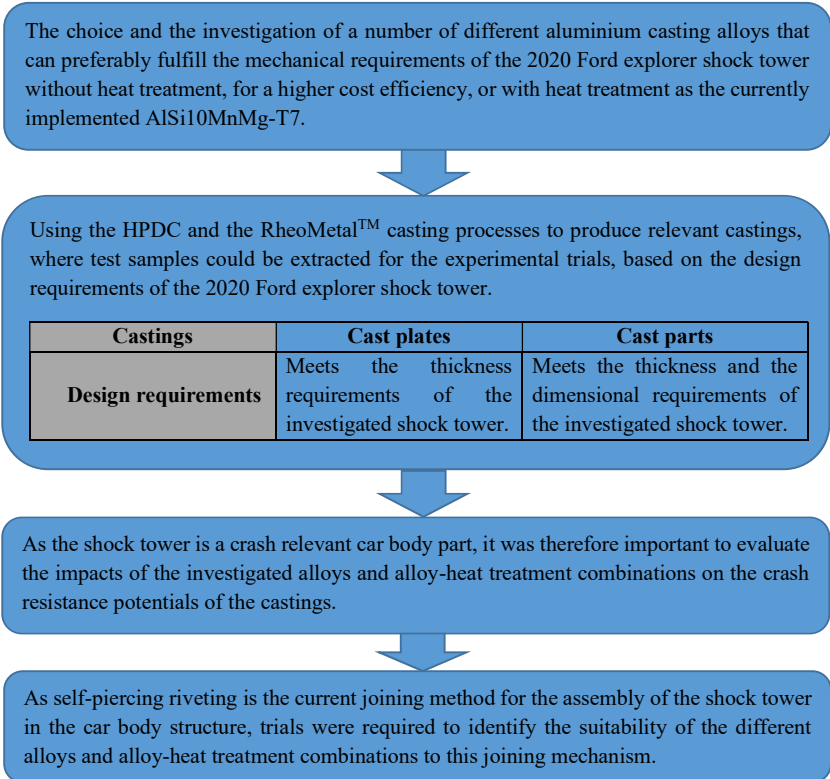


Figure 4.2: The experimental approach.

All of the steps in the above experimental approach are described in the upcoming sections.

4.1 Defining the suitable test alloys

In order to reach the desired mechanical properties in a cost-efficient way, it was important to design the experimental trials by taking a number of different aluminium casting alloys, heat treatments and casting conditions into consideration. All those aspects and their combinations are represented in *Table 4.1* as follows.

4. Experimental approach

Table 4.1: An overview about the different alloys and their standard specifications (1) (2) (3), the heat treatments, the suppliers and the casting processes that were used in this thesis.

Denomination Alloy - HT (Supplier)	Alloy	Heat treat- ment (HT)	Supplier	Casting process	Standard specifications			
					Rp0.2 (MPa)	Rm (MPa)	A (%)	
AlSi7Mg0.3-F (1)	AlSi7Mg0.3	-	1	HPDC & Rheom- etal™	80- 140	140- 220	2- 4	
AlMg5Si2Mn-F (1)	AlMg5Si2Mn				(160- 220)*	(310- 340)*	(11- 22)*	
AlMg6Si2MnZr- F (1)	AlMg6Si2MnZr				(200- 220)"	(340- 360) "	(9- 12)"	
AlMg4Fe2-F (1)	AlMg4Fe2				(120- 150) *	(240- 280) *	(10- 22)*	
AlSi10MnMg-F (2)	AlSi10MnMg	T5	2	HPDC	120- 150	250- 290	5- 11	
AlSi10MnMg-T5 (2)					150- 240	270- 320	4- 9	
AlSi10MnMg-T7 (2)					120- 150	190- 220	12- 18	
AlSi7MnMg-F (2)	AlSi7MnMg	-	(F)	T5	125- 145	245- 265	9- 12	
AlSi7MnMg-T5 (2)					120- 160	190- 260	6- 12	
EN AB-42000-F (3)					EN AB-42000	-	(F)	3
AlMg4Fe2-F (3)	AlMg4Fe2	(120- 150) *	(240- 280) *	(10- 22)*				
MYFORD-F (3)	MYFORD	-						

*Valid for a thickness range of 2-4 mm. " Valid for a thickness range of 2-3 mm.

As shown in *Table 4.1*, the test plates and the parts were produced at the following three suppliers:

- Supplier 1, which refers to the *Foundry Institute (GI) of the RWTH Aachen University*.
- Supplier 2, which refers to *Magna BDW technologies Soest GmbH*.
- Supplier 3, which resembles *Comptech AB*.

At each supplier, a distinct group of alloys was chosen to produce the castings. Each alloy-heat treatment-casting process combination was then tested to determine if it can meet the mechanical requirements of the 2020 Ford explorer shock tower, which according to Ford's specification manual should have a yield strength value (Rp0.2) greater than 120 MPa, an ultimate tensile strength value (Rm) greater than 180 MPa and a total elongation value (A) greater than 10%. These mechanical requirements are valid for the defined thickness range in *Figure 4.1(b)*.

4. Experimental approach

The first step involved testing the alloys, which belong to the Al-Si alloy family in *Table 2.5*, at supplier 2. These alloys are mainly used, as illustrated earlier in *section 2.1*, to produce the structural body castings by HPDC. However, they might require heat treatment to reach the desired mechanical properties of these castings. In this thesis, the T5 and the T7 heat treatments were implemented by *Magna BDW technologies Soest GmbH* on several Al-Si die-cast plates. This was done in order to test the possibility of reaching the required mechanical properties of the 2020 Ford explorer shock tower by using the cost-efficient T5 heat treatment process. In addition, and as AlSi10MnMg-T7 is the currently applied alloy-heat treatment combination for this shock tower, the mechanical testing outcomes from the T7 heat-treated AlSi10MnMg plates were used as a reference to simulate the expected performance.

Although the AlSi10MnMg alloy is highly suitable for the HPDC process, it cannot be regarded as an ideal candidate for the RheoMetal™ process. This is due to its large Si content, which results in a narrow solidification interval of approximately 17 K (75). Therefore, and due to the positive impact of the RheoMetal™ process on the cost efficiency of the castings, it was important to investigate other alloys, such as the AlMg5Si2Mn and the AlMg6Si2MnZr alloys, which could not only achieve the desired mechanical properties without heat treatment, but can also be suitable for the RheoMetal™ process. This suitability was confirmed by comparing the performances of those alloys in the RheoMetal™ process to the performances of the standard RheoMetal™ alloys, such as the AlSi7Mg0.3 and the EN AB-42000 alloys.

On the other hand, the new alloy, MYFORD, was mainly developed to enhance the feeding efficiency and the rheocastability of the AlMg4Fe2 alloy, and thus facilitate the use of this alloy family (Al-Mg-Fe), with the enhanced as-cast mechanical properties, in the cost-efficient mass production of the thin walled structural aluminium body castings.

4.2 The production of the test plates using the HPDC process

For the production of the supplier 1 plates by the high pressure die casting process, a cold chamber H-630 SC Buehler machine with a 400 mbar Fondarex vacuum unit and vacuum valve was used. The required molten metal for each shot was transferred from the holding furnace in *Figure 4.3(a)* into the shot sleeve in *Figure 4.3(b)* with the help of a ladle that is attached to a robot arm.

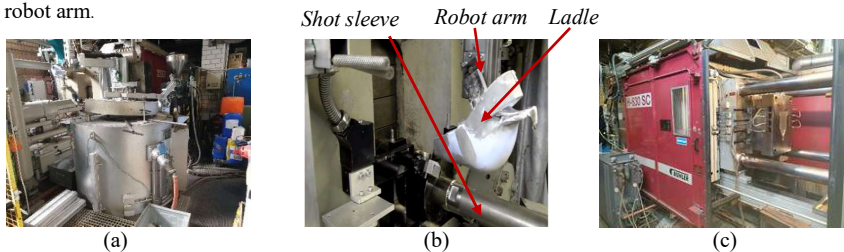


Figure 4.3: The HPDC setup consisting of (a) the holding electric resistance furnace, (b) the shot sleeve, ladle & robot arm and (c) the vacuum assisted die.

4. Experimental approach

These plates, produced using the setup in *Figure 4.3*, were 3.1 mm thick and had the dimensions in *Figure 4.4*.

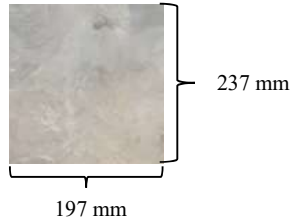


Figure 4.4: The dimensions of the plates from supplier 1.

The die cavity's design in *Figure 4.5*, with the gate dimensions in *Table 4.2*, was used for the HPDC trials at supplier 1.

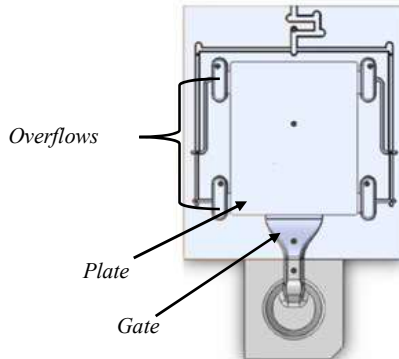


Figure 4.5: The die cavity's design for the HPDC trials at supplier 1.

Table 4.2: The different dimensions of the gate that was used for the HPDC trials at supplier 1.

Feature	Dimension (mm)
Thickness of the gate	2.087
Length of the gate	88.699

The gate dimensions in *Table 4.2* were chosen because they followed the gate thickness' requirements and the gate area requirement for an atomized jet flow (19). The upper and lower overflows served in reducing the overall porosity level by facilitating the escape of the air during the casting process.

Unlike the plates in *Figure 4.4*, the plates from supplier 2 were 2.5 mm thick and had the dimensions in *Figure 4.6*. For these plates, the external supplier (*Magna BDW technologies*

4. Experimental approach

Soest GmbH) provided no information about the size and the features of the gating system, as well as the process parameters. However, it was assumed that, like for the supplier 1 plates, respective optimum process parameters were also used to produce the plates at supplier 2.

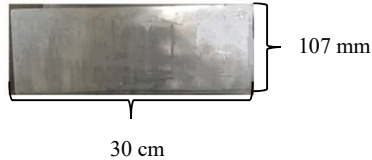


Figure 4.6: The dimensions of the plates from supplier 2.

The test plan for the HPDC trials at supplier 1 is represented in *Table 4.3*. The reasons beyond choosing the parameters in the upcoming test plan will be addressed extensively in *section 5.1.1*.

Table 4.3: The test plan for the HPDC trials.

Designation	Alloy denomination from <i>Table 4.1</i>	Piston velocity in the 1 st phase (m/s)	Piston velocity in the 2 nd phase (m/s)	Intensification pressure (bar)	Total number of produced plates
A-(2.5-650)*	AlSi7Mg0.3-F (1)	0.2	2.5	650	10
A-(3-650)			3		10
A-(3.5-650)			3.5		20
B-(2.5-650)*	AlMg5Si2Mn-F (1)		2.5	650	10
B-(3-650)*			3		10
B-(3.5-650)			3.5		20
C-(2.5-650)*	AlMg6Si2MnZr-F (1)		2.5	650	10
C-(3-650)*			3		10
C-(3.5-650)			3.5		20
D-(2.5-650)*	AlMg4Fe2-F (1)		2.5	650	10
D-(3-650)		3	84		
D-(3.5-650)		3.5	10		
D-(3.5-300)*			300	20	
H	AlSi10MnMg-F (2)	Produced at <i>Magna BDW technologies Soest GmbH</i>			10
H-T5	AlSi10MnMg-T5 (2)				10
H-T7	AlSi10MnMg-T7 (2)				10
I	AlSi7MnMg-F (2)				10
I-T5	AlSi7MnMg-T5 (2)				10

*Used exclusively for the determination of the optimum process parameters.

4. Experimental approach

4.3 The production of the test plates using the RheoMetal™ process

Similar to the HPDC process, test plates, with the dimensions in *Figure 4.4*, were produced by the RheoMetal™ process. These plates were produced from the alloys in *Table 4.5*, with the help of the manual setup in *Figure 4.7*.

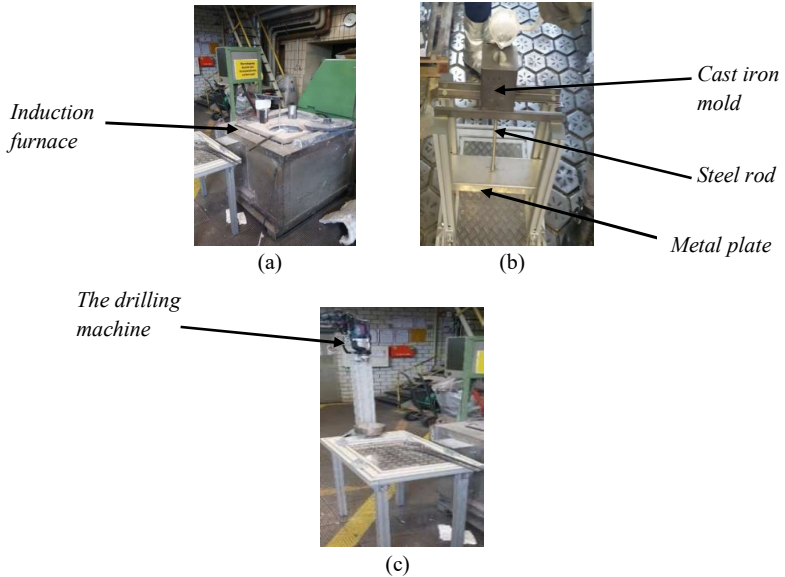


Figure 4.7: The setup consisting of (a) the induction furnace, (b) the EEM production station and (c) the slurry production station.

Figure 4.7 illustrates the three stations that were used to produce the semi-solid slurry. The induction furnace in the first station, *Figure 4.7(a)*, was responsible for melting the feedstock (ingots). The second station, *Figure 4.7(b)*, is where the production of the EEM took place by:

1. Introducing a steel rod to the bottom of the open mold and supporting this rod from falling by a metal plate.
2. Filling the closed mold with melt from the furnace to obtain an initial casted EEM.
3. Calculating the exact height of the EEM (h_{EEM}), which is required to achieve the needed %EEM, with the help of the following formulas:

$$\text{Mass of the EEM} = \%EEM * \text{Mass of the shot} \quad (4.1)$$

4. Experimental approach

$$\text{Volume of the EEM} = \pi * h_{EEM} * (R^2 - r^2) \quad (4.2)$$

Where R is the radius of the EEM, and r is the radius of the rod.

By incorporating the mass and the volume of the EEM into the density equation, it was possible to calculate the h_{EEM} by using the following formula:

$$h_{EEM} = \frac{\text{Mass of the shot} * \%EEM}{\text{Density} * (R^2 - r^2) * \pi} \quad (4.3)$$

4. Adjusting the height of the casted EEM to the calculated h_{EEM} with the help of the sawing machine in *Figure 4.8(b)*.

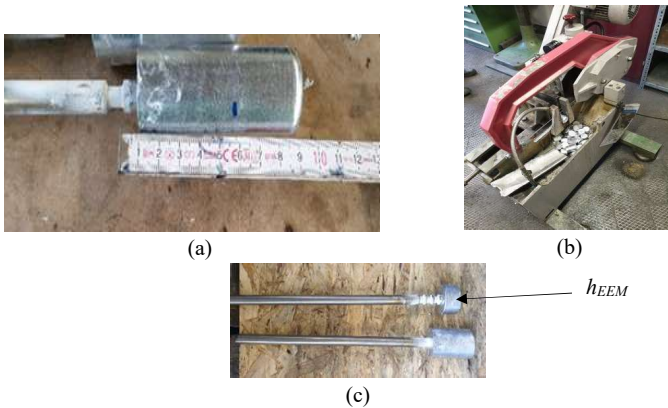


Figure 4.8: (a) The EEM's height before adjustment (casted EEM), (b) the sawing machine and (c) the EEM's height after adjustment (h_{EEM}).

The third station, *Figure 4.7(c)*, is where the semi-solid slurry was made, first by attaching the rod with the EEM into the drilling machine and then lowering it into the ladle containing the melt, as shown in *Figure 4.9*. The rod was always kept rotating during this step to break down the dendrites, which form during solidification, in order to develop a globular microstructure.



Figure 4.9: The slurry making process.

4. Experimental approach

After the slurry was produced, it was then poured into the shot sleeve of the cold chamber H-630 SC Buehler HPDC machine and later injected into the die cavity using a piston, with a diameter of 60 mm, to produce the plates in *Figure 4.4*.

Unlike the dimensions in *Table 4.2* and as shown in *Figure 4.10* and *Table 4.4*, a longer and a thicker gate was chosen for the RheoMetal™ casting trials at supplier 1. This choice was based on the earlier findings that emphasised the need for gates with larger dimensions to enhance the flow of the slurry and to prevent its premature solidification (76). In addition, no lower overflows were used. This was done in order to improve the flow of the semi-solid slurry into the die cavity by preventing its accumulation and clogging at the entries of the overflows.

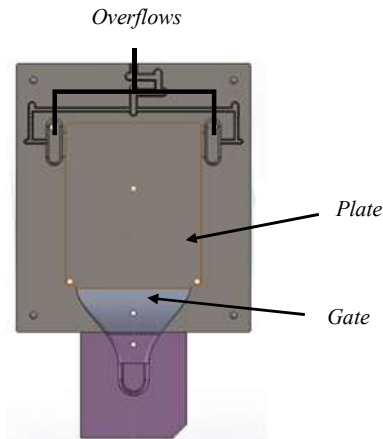


Figure 4.10: The die cavity's design for the RheoMetal™ casting trials at supplier 1.

Table 4.4: The different dimensions of the gate that was used for the RheoMetal™ casting trials at supplier 1.

Feature	Dimension (mm)
Thickness of the gate	3.305 mm
Length of the gate	169 mm

The test plan for the RheoMetal™ casting trials at supplier 1 is represented in *Table 4.5*. The reasons beyond choosing the parameters in the upcoming test plan will be addressed extensively in *sections 6.1.1.1 and 6.1.1.2*

4. Experimental approach

* Used exclusively for the determination of the optimum process parameters.

Table 4.5: The test plan for the RheoMetal™ casting trials at supplier 1.

Designation	Alloy denomination from Table 4.1	Super heat (°C)	Piston velocities (m/s)	Mass of the shot (g)	h _{EEM} (mm)	EEM's		Intensification pressure (bar)	Rotation speed of the EEM (rpm)	Total Number of produced plates
						Temperature (°C)	Insertion time (s)			
A-(50-4.63-575-1000)-R	AlSi7Mg0.3-F (1)	50		2128	4.63				0-1000	20
A-(50-4.63-575-3000)-R*										5
B-(30-2.49-575-1000)-R*	AlMg5Si2Mn-F (1)	30		2108	2.49				0-3000	5
B-(30-4.63-575-1000)-R										20
C-(40-4.63-575-1000)-R*	AlMg6Si2MnZr-F (1)	40	1 st phase = 0.15-0.2 2 nd phase = 1.26	2112					575	4
C-(50-4.63-575-1000)-R										20
D-(50-4.63-575-1000)-R	AlMg4Fe2-F (1)	50		2136	4.63				0-1000	20
D-(50-4.63-500-1000)-R*										20
D-(50-4.63-300-1000)-R*										5
										5

4. Experimental approach

4.4 The production of the parts

The production of a part, with similar dimensions to the 2020 Ford explorer shock tower in *Figure 4.1*, was a very important milestone within the framework of this thesis. This is because, unlike the results obtained from the plates, it was possible to retrieve reliable and more representable conclusions by testing and analyzing the different sections of the considered parts.

The considered part in my case was a heatsink, which is used in the telecommunication industry. The shape and the dimensions of this part are demonstrated in *Figure 4.11* as follows.

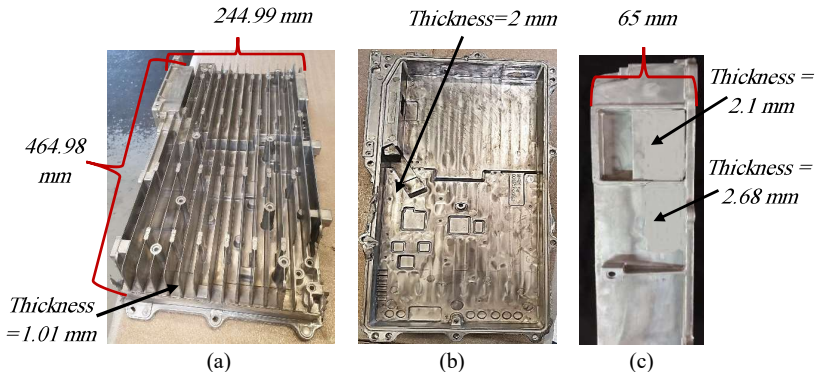


Figure 4.11: (a) The top view, (b) the bottom view and the (c) side view of the part.

The parts, with the dimensions in *Figure 4.11*, were produced at the Swedish company *Comptech AB* using the conventional high pressure die casting process as well as the Rheometal™ process. The dimensions of the gate that was used to produce these parts is represented in *Table 4.6* as shown below.

Table 4.6: The different dimensions of the gate that was used for the HPDC and the RheoMetal™ casting trials at supplier 1.

Feature	Dimension (mm)
Thickness of the gate	9
Length of the gate	178

The production of each part using the HPDC process involved transferring 5 kg of the liquid melt from the furnace to the shot sleeve of a cold chamber 800-ton Buehler machine, which was equipped with a vacuum unit and a vacuum valve, with the help of a robot arm. At the end of the production cycle and as shown in *Figure 4.12(b)* and *Figure 4.12(c)*, a second robot arm was assigned with the task of removing the part from the die into a movable tray for inspection and for the removal of the gating system and the overflows (at the top of the part) by one of the plant's workers.

4. Experimental approach

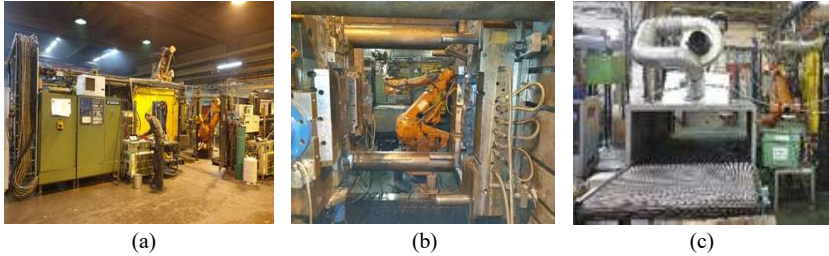


Figure 4.12: (a) The 800-ton HPDC machine, (b) the die and the second robot arm and the (c) moving tray.

On the other hand, and as mentioned earlier, the production of the parts using the Rheometal™ process was not that straight forward and involved a number of additional pre-steps. These steps, as illustrated in *Figure 4.13*, were mainly needed for the production of the semi-solid slurry.

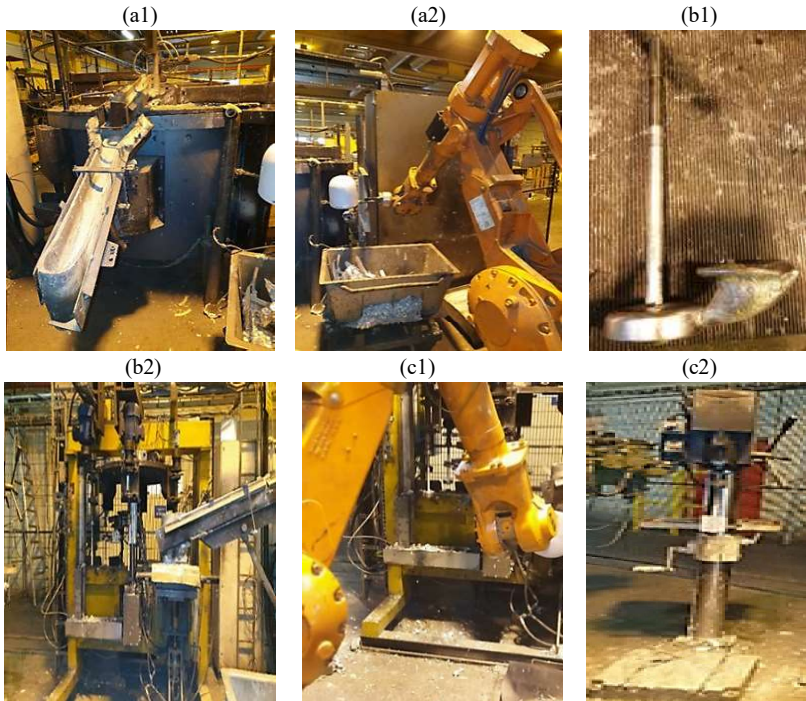


Figure 4.13: The different pre-steps for the production of the semi-solid slurry.

4. Experimental approach

As shown in *Figure 4.13* and similar to the sketch in *Figure 2.20*, the additional pre-steps for the Rheometal™ process were:

1. Transferring the liquid melt from the furnace (a1) to the setup in (b2) with the help of the robot arm in (a2).
2. In the meanwhile, the production of the EEM in (b1) proceeded by the setup in (b2).
3. After that and as seen in (c1), the EEM was inserted into the slightly rotated ladle having the liquid melt for the sake of producing the globular microstructure of the semi-solid slurry.
4. (c2) illustrates the extra step, which was applied to promote the homogenous mixing of the new formed slurry.

4.4.1 New alloy for an enhanced feeding efficiency and rheocastability

Although the Al-Mg-Fe alloys in general and the AlMg4Fe2 alloy in particular have superior as-cast mechanical properties, they might be, as mentioned earlier in *section 2.5*, difficult to cast. In addition, and due to its solidification sequence that involves the primary solidification of an Fe-intermetallic phase ($\text{Al}_{13}\text{Fe}_4$ phase) prior to the α -Al phase, the standard AlMg4Fe2 alloy, which is represented by the region between the dashed lines in *Figure 4.14*, might experience a low feeding efficiency of the melt during HPDC and might not be suitable for the Rheometal™ casting process.

Therefore, and in order to benefit from the advantageous mechanical properties of this alloy in the as-cast state, it was important to investigate the different means that could play a role in enhancing and optimizing its feeding efficiency and rheocastability.

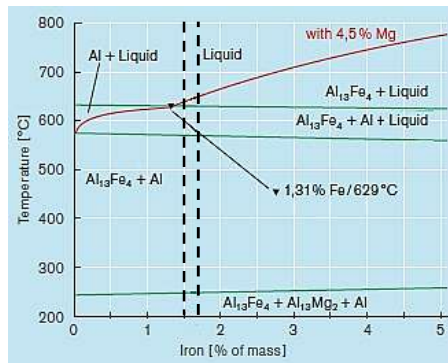


Figure 4.14: The phase diagram of the standard AlMg4Fe2 alloy with 1.5-1.7%Fe and 4.5% Mg (modified from (77)).

4. Experimental approach

Towards enhancing this AlMg4Fe2 alloy's performance, a number of different steps were carried out as follows:

1. The first step involved analyzing the phase diagram of the AlMg4Fe2 alloy in *Figure 4.14*, with, as represented by the region between the dashed lines, an iron mass percentage in the range of 1.5-1.7%, and, as represented by the red line, a magnesium mass percentage of 4.5%. The purpose of this analysis was to identify the approaches that would lead to an enhancement in its feeding efficiency and rheocastability.

This analysis led to the suggestion of initially setting the iron mass percentage to a value less than 1.3%. This suggestion, demonstrated by the black arrow and circle in *Figure 4.15*, was expected to result in the primary solidification of the α -Al phase, which does not only cause an improvement in the feeding efficiency of the alloy by decreasing the restrictions to the interdendritic pathways, but also, as mentioned earlier in *section 2.4*, leads to it being more suitable for the semi-solid casting processes, as it results in the development of an adequate solid fraction of the slurry (α -Al phase) before any other phase started to develop.

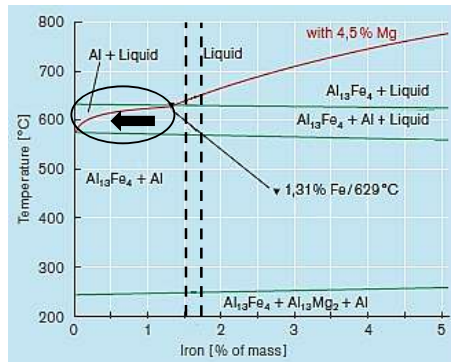


Figure 4.15: The suggested enhancement to the standard AlMg4Fe2 alloy, as demonstrated by the circle and the arrow (modified from (77)).

2. The second step involved performing a number of simulations using the JMatPro® software for the sake of checking whether the suggestion in the first step was valid or not. All the simulations, which were performed by the company *RheoMetal AB* in Stockholm city, were based on Scheil-Gulliver equation that assumes a local equilibrium at the solid-liquid interface, no diffusion of the elements in the solid phase and a very fast diffusion in the liquid phase (78) (79).

The first simulation involved an Al-Mg-Fe alloy, with the chemical composition in *Table 4.7*.

4. Experimental approach

Table 4.7: The considered chemical composition in mass % of the Al-Mg-Fe alloy.

Si	Fe	Mn	Mg	Cu	Al
0.1	1.3	0.075	4.3	0.1	94.125

All of the elements in *Table 4.7*, except iron and aluminium, had mass percentages that complied with the standard AlMg4Fe2 alloy (2).

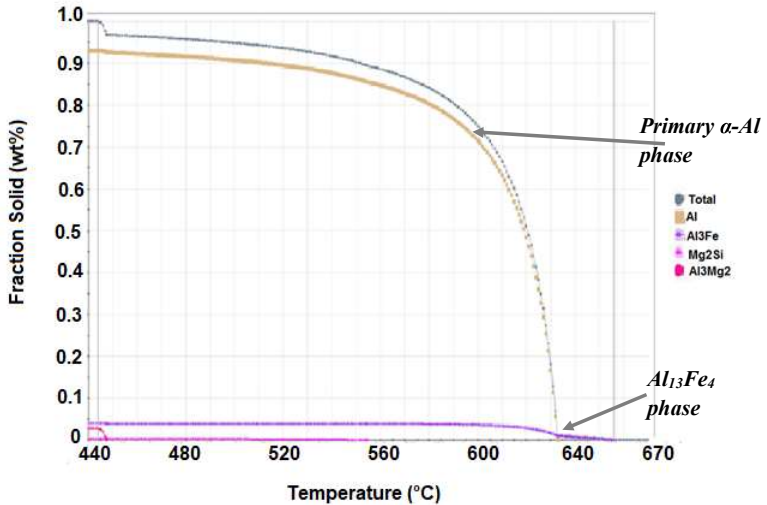


Figure 4.16: The JMatPro® simulation for the Al-Mg-Fe alloy with a 1.3%Fe.

The main outcome of the simulation in *Figure 4.16* was that although a lower Fe% than that of the standard AlMg4Fe2 alloy was used in the simulation, it was still not enough to cause the aimed primary solidification of the α -Al phase.

The second simulation was done to check whether a further reduction in the iron mass percentage from 1.3% to 0.5% (MYFORD) can lead to an enhancement in the properties of the alloy or not. This simulation was performed using the chemical composition in *Table 4.8*.

Table 4.8: The suggested chemical composition in mass % of the MYFORD alloy.

Si	Fe	Mn	Mg	Cu	Al
0.1	0.5	0.075	4.3	0.1	94.925

Comparing between the chemical compositions in *Table 4.7* and *Table 4.8* shows that lower iron and higher aluminium mass percentages were considered for the second simulation.

4. Experimental approach

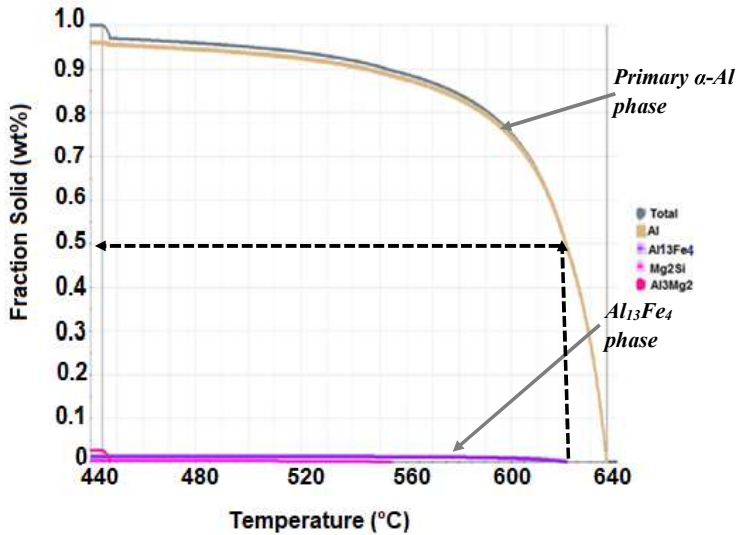


Figure 4.17: The JMatPro® simulation for the MYFORD alloy.

As seen in Figure 4.17, setting the iron content of the AlMg₄Fe₂ alloy to 0.5% (MYFORD) had resulted in the desired modifications to the feeding efficiency of the melt, by delaying the solidification of the Al₁₃Fe₄ phase to be beyond the primary α -Al phase, and in the alloy's rheocastability, by causing, as demonstrated by the black dashed lines, the development of 50% solid fraction (α -Al phase) before any other phase started to form.

Further improvement in the alloy's rheocastability can be reached by additionally reducing the Fe% to a level below the 0.5%. This is due to the ability of this adjustment to cause a wider solidification interval, which is beneficial for the stability of the thixotropic slurry. Therefore, the ideal iron content for this new alloy shall be $\leq 0.5\%$.

Regarding this newly developed alloy, two patent applications have been filed [Patapp1] [Patapp2].

The test plan for the HPDC trials and the RheoMetal™ casting trials at supplier 3 is represented in Table 4.9. The reasons beyond choosing the parameters in this test plan will be addressed extensively in sections 5.1.2 and 6.1.2.

4. Experimental approach

* Used exclusively for the determination of the process parameters' optimization potential.

Table 4.9: The test plan for the HPDC and the RheoMetal™ casting trials at supplier 3.

Designation	Alloy denomination from <i>Table 4.1</i>	Casting process	Melt superheat (°C)	Furnace temperature (°C)	Piston velocities (m/s)	Mass of the shot (g)	Mass of the EEM (mm)	EEM's		Intensification pressure (bar)	Rotation speed of the EEM (rpm)	Total Number of produced plates				
								Preheating temperature (°C)	Insertion time (s)							
E-(730)	EN AB-42000-F (3)	HPDC	-	730	1 st phase= 0.223 2 nd phase= 2.86	5000	30	-	15	340	1100	5				
E-(730-30-1100)-R			-					25								
E-(730-30-1500)-R*		Rheometal TM _M	40					750			5502	40	100	30	5	
E-(730-40-1100)-R*			50													5
E-(750-30-1100)-R*			-													
F-(740)		AlMg4Fe2	HPDC					-			740	1 st phase= 0.223 2 nd phase= 5.23	5000	-	-	-
F-(750-30-1100)-R	-F (3)	Rheometal TM _M	40	750	1 st phase= 0.223 2 nd phase= 2.86	5500	30	100	1100	24						
G-(755)	MYFORD	HPDC	-	755	1 st phase=0.223 2 nd phase= 5.23	5000	-	-	-	-	10					
G-(755-30-1100)-R	-F (3)	Rheometal TM _M	40	750	1 st phase= 0.223 2 nd phase= 2.86	5498	30	100	1100	15						

4. Experimental approach

4.5 The characterization of the material properties and the process parameters

For the complete and accurate characterization of the material properties and the process parameters, the following tests and evaluation approaches were implemented:

- Uniaxial tensile test.
- 3-point bending test.
- Density measurement with the help of Archimedes' principle.
- Self-piercing riveting test.
- Microstructural analysis.
- SEM-EDS analysis.
- Spectrochemical analysis.

4.5.1 Uniaxial tensile test

Tensile testing is regarded as one of the most common methods for the characterization of the mechanical properties. In this thesis, the tensile testing was implemented in the following manner:

1. Defining the tensile testing sample types

In the tensile testing trials, two different sample types were used as shown below.

The *Type E* sample from the *DIN 50125* standard (6). This sample, in *Figure 4.18*, with a total length (L_t) of 105.27 mm and an original gauge length (L_o) of 30 mm, was extracted mainly from the supplier 1 plates (thickness = 3.1 mm) due to its suitability to the thickness range of 3-18 mm.

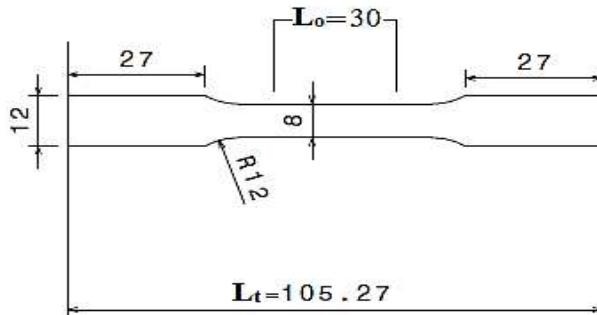


Figure 4.18: The exact geometrical dimensions of the Type E sample in mm (6).

4. Experimental approach

The *mini sample*, in *Figure 4.19*, was designed by downscaling the *DIN 50125* standard's Type H sample (6) to a total length (L_t) of 76 mm and an original gauge length (L_o) of 25 mm. This downscaling facilitated the extraction of the samples from smaller sections, specifically in the supplier 2 plates and the supplier 3 parts.

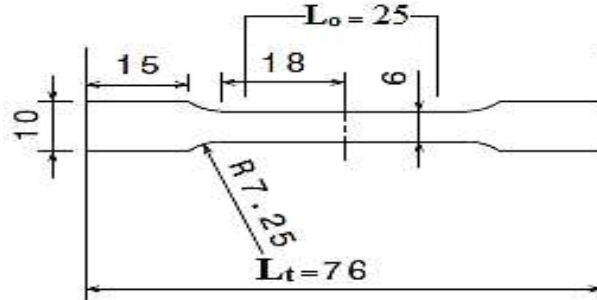


Figure 4.19: The exact geometrical dimensions of the mini samples in mm.

2. Extracting the samples from the castings

After defining the suitable sample designs, it was important to specify and carry out the following steps in order to extract those designs from the designated castings:

The first step involved, as seen in *Figure 4.20*, creating three dimensional models (3D) of the samples and the castings with the help of the software *CATIA*®. These 3D models were created by the Advanced Materials & processes department of *Ford-Werke GmbH* in Aachen city.

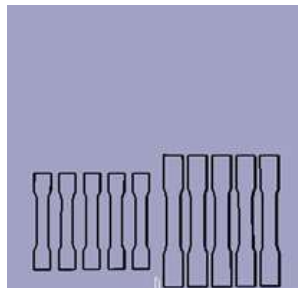


Figure 4.20: A 3D model of the supplier 1 plate and the tensile testing samples.

The 3D models of the samples were designed, as shown in *Figure 4.21*, to have slightly different dimensions than those displayed in *Figure 4.18* and *Figure 4.19*.

4. Experimental approach

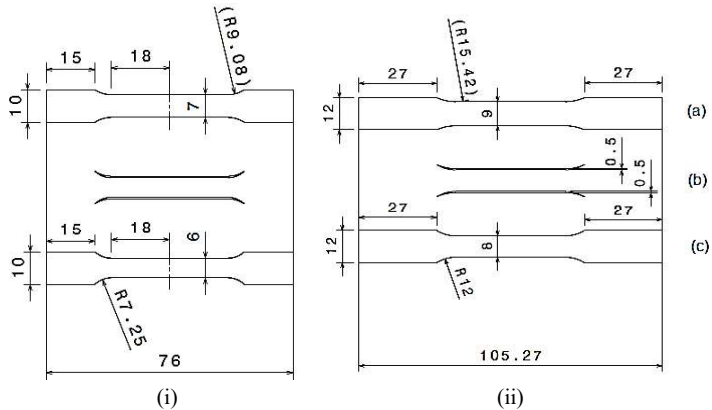


Figure 4.21: (a) The initial dimension, (b) the extra 1 mm and (c) the final dimension of the (i) mini sample and the (ii) Type E sample in mm.

Although the extra 1 mm in *Figure 4.21(b)*, was removed from each sample by a milling machine. It was however still initially needed to avoid the formation of the rough edges and the surface defects in the final (standard) dimensions of the samples. These defects that develop during the extraction of the samples from the castings, as seen in *Figure 4.22*, might act as sites for crack initiation and propagation during tensile testing.

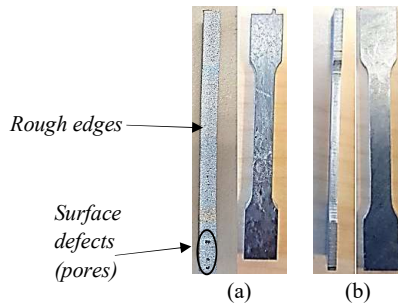


Figure 4.22: The top and side views of a mini sample (a) before and (b) after preparation.

The waterjet cutting method was the implemented sample extraction method, due to the ability of this cold cutting mechanism to produce unhardened edges with high precision values (80) (81). This cutting mechanism was carried out at the Pilot-Plant of *Ford-Werke GmbH* in Cologne city.

4. Experimental approach

For the samples to be extracted from the castings by waterjet cutting, as seen in *Figure 4.23*, the 3D models from the first step had to be converted into the DXF file format, as this is the suitable file format for the waterjet cutting machine.

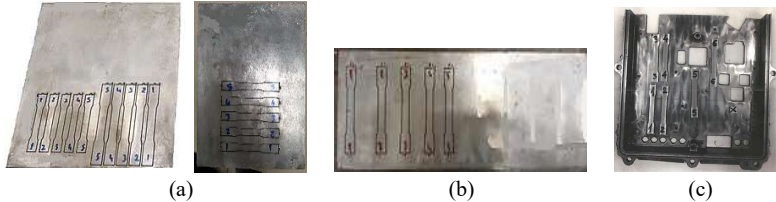


Figure 4.23: The extracted tensile test samples from the (a) supplier 1 plates, (b) supplier 2 plates and (c) supplier 3 parts.

3. Defining the uniaxial tensile testing setup and parameters

An improvised testing setup was installed in a *ZwickRoell* materials testing machine for the Type E and the mini samples. This was due to the relatively small size of those samples, which made it not possible for the standard setup to be used. A picture of this special setup is shown in *Figure 4.24* as follows.

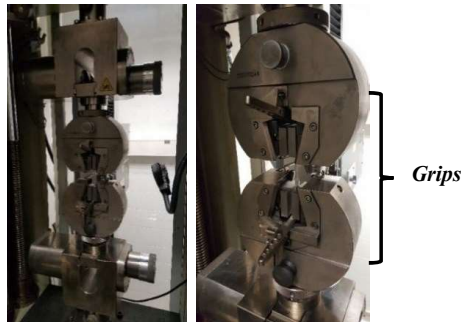


Figure 4.24: The tensile test setup for the mini and the Type E samples.

As seen in *Figure 4.24* and unlike the conventional set up, two special grips were used. The purpose of implementing this approach was to be able to adjust the gap between the grips to better accommodate the relatively small parallel length of the samples.

The uniaxial tensile tests were conducted according to method B of the ISO 6892-1 standard (5). For all the trials a pre-force of 5 MPa was implemented. The Young's modulus determination interval varied for each alloy and was typically in the range of 20-80 MPa.

4. Experimental approach

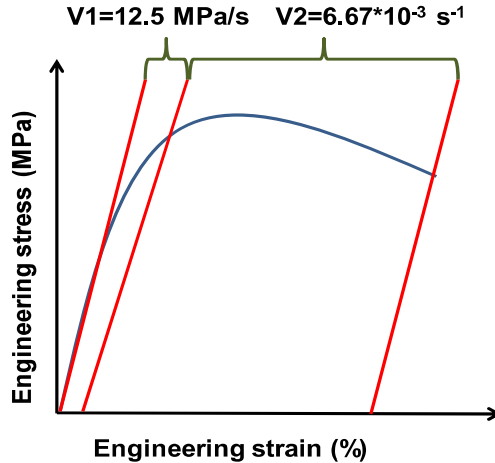


Figure 4.25: The different test speeds during tensile testing.

For all the different alloys and as shown in *Figure 4.25*, the test speed in the elastic region (V1) was stress controlled at a stress rate value of 12.5 MPa/s. However, the test speed in the plastic region (V2) was displacement controlled at a strain rate ($\dot{\epsilon}$) value of 0.00667 s⁻¹.

4.5.2 3-point bending test

Like the tensile test, bending test is considered to provide representable readings that accurately describes the mechanical properties of the tested material. Unlike in the tensile test, a bending force is applied on the sample and not a uniaxial tension force.

In this study, 3-point bending tests were also performed using the same *ZwickRoell* materials testing machine as the one used for tensile testing. These tests were done for the sake of backing up the tensile test results and for their ability to better represent the outcome of some of the investigated phenomena, such as the crash resistance behaviour of the castings. The actual setup of the 3-point bending test and the important dimensions that had to adhere to the chosen testing standard are represented in *Figure 4.26*.

4. Experimental approach

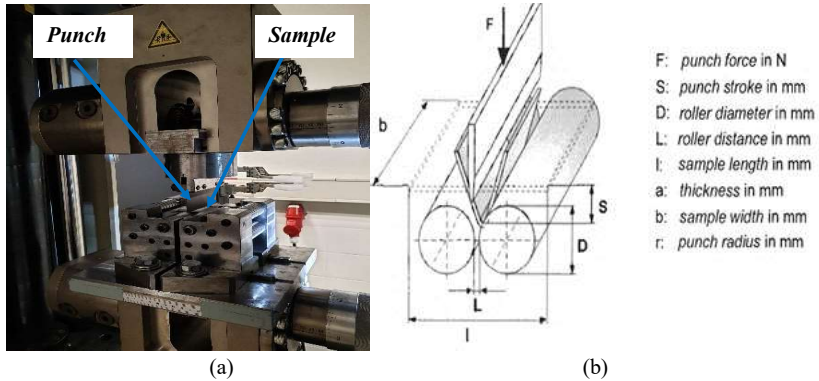


Figure 4.26: (a) The setup of the 3-point bending test and (b) the important dimensions (4).

All the steps in *section 4.5.1*, except the sample preparation step after the waterjet cutting procedure, were implemented as pre-bending test steps.

The 3-point bending tests were conducted according to the VDA 238 -100 standard (4). The defined conditions for each 3-point bending test included a test speed of 20 mm/min, a punch radius of 0.4 mm, a pre-force of 100 N, a force shut off threshold of 60 N and a roller distance equal to double the thickness of the sample.

The samples used in the trials did not exactly comply with the VDA 238 -100 standard and had a width of 30 mm as shown in *Figure 4.27*.

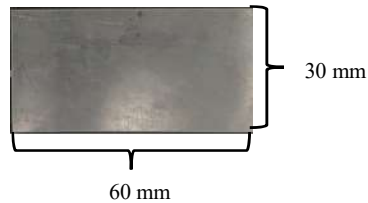


Figure 4.27: The dimensions of the bending test samples.

The above test samples were extracted from several positions within the castings as shown in *Figure 4.28*.

4. Experimental approach

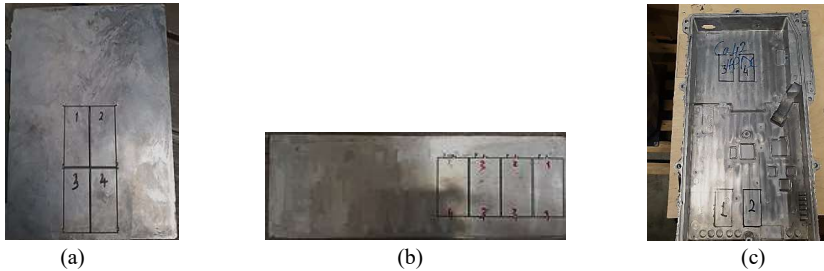


Figure 4.28: The location of the 3-point bending test samples in the (a) supplier 1 plates, (b) supplier 2 plates and (c) supplier 3 parts.

After performing the test, the bending angle for each of the deformed samples, e.g. *Figure 4.29 (a)*, was measured with the tool in *Figure 4.29(b)*.

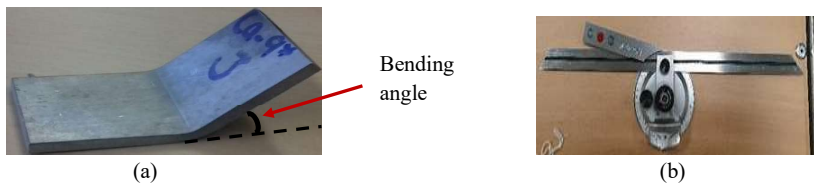


Figure 4.29: (a) An example of a bending angle and (b) the bending angle's measuring tool.

4.5.3 Density measurement

The integrity of the castings depends on their porosity levels. Therefore, finding a method that could quantify these porosity levels was considered vital for accurately characterizing the quality of the plates.

Measuring the density of the plates by the Archimedes' principle, which states that the difference between the weight of an object in air and its weight in water is equal to the weight of the displaced water (82), is regarded as one of the main methods that can provide an estimation of the micro porosity content (83).

In general, a higher density refers directly to a lower porosity level as shown in *Figure 2.8(b)*.

The porosity level for each of the investigated plates was calculated with the help of the following formula:

$$\text{Porosity \%} = \frac{(\rho_0 - \rho_{\text{of plate}_{\text{air}}})}{\rho_{\text{of plate}_{\text{air}}}} * 100 \quad (4.4)$$

4. Experimental approach

In which ρ_0 is the ideal density and ρ of *plate_{air}* is the measured density of the plate by the Archimedes' principle.

- According to *Aluminium Rheinfelden GmbH*, the density values in their supplier manuals were derived using Archimedes' principle from flawless and airtight chill casting discs. For this reason, the ideal density of each alloy (ρ_0) in my calculations was considered to be the same as the one provided by the alloy's supplier.
- For the measured density (ρ of *plate_{air}*), the following setup and formulas were used for the measurement of the density:

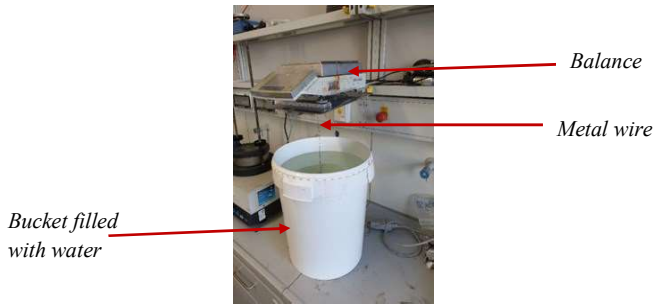


Figure 4.30: The setup for the density measurement trials.

Prior to the beginning of the density measurement trials, the temperature of water had to be first measured and inserted in the balance, to determine the exact density of water (ρ_{water}).

The trials were then conducted, with the help of the setup in *Figure 4.30*, for the sake of determining the mass of the plate in air (M of *plate_{air}*) and the mass of the plate in water (M of *plate_{water}*). Using both masses, it was possible to calculate the volume of the plate (V_{plate}) according to the *equation (4.5)* as follows:

$$V_{plate} = \frac{M \text{ of } plate_{air} - M \text{ of } plate_{water}}{\rho_{water}} \quad (4.5)$$

The density of the plate in air (ρ of *plate_{air}*) was then calculated based on the following formulas:

$$\rho \text{ of } plate_{air} = \frac{M \text{ of } plate_{air}}{V_{plate}} \quad (4.6)$$

$$\rho \text{ of } plate_{air} = \frac{M \text{ of } plate_{air}}{M \text{ of } plate_{air} - M \text{ of } plate_{water}} \rho_{water} \quad (4.7)$$

4. Experimental approach

4.5.4 Self-piercing riveting

The ability to join the car body parts is essential for the automotive industry. For this reason, it is important to make sure that the joining requirements of the parts are fulfilled by their assigned alloys or alloy-heat treatment combinations.

Due to the difficulty in welding the lightweight materials, self-piercing riveting (SPR) is presently the main joining process in the automotive industry for aluminium intensive and mixed-material vehicle structures (84) (85). This technology is suitable for high volume productions, as in the case of Ford's F-150 trucks, which require between 2200 and 2700 rivets per vehicle (85).

In this thesis, SPR trials were conducted at *Atlas Copco* according to the joining requirements of the 2020 Ford explorer shock tower. The reason beyond conducting these trials was their ability to predict the actual rivetability of the castings by simulating the complex bending and stretching mechanisms that occur during the riveting process at different forming limits. The planning of the SPR trials encompassed a number of different steps. These steps were done in the following order, for the aim of making sure that the outcomes of the joining trials are accurate and representable:

1. The first step involved checking the CAD design of the 2020 Ford explorer car body to identify the different materials and structures that are joined to the cast aluminium shock tower. From all the possible materials' combinations, the 1.3 mm DP600 steel sheet was chosen for the SPR trials. The reason beyond this choice is the higher joining difficulty that this structure offers in comparison to the other material combinations such as the mild steels and the aluminium extrusions.
2. The second step involved obtaining samples for the SPR trials by cutting sections from the different plates, as shown in *Figure 4.31*. Each of these samples had a length of 100 mm and a width ranging from 25 mm to 37 mm.

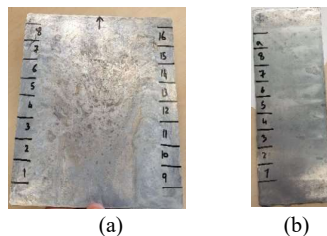


Figure 4.31: The positions of the SPR samples in (a) the supplier 1 plates (thickness = 3.1 mm) and (b) the supplier 2 plates (thickness = 2.65 mm).

4. Experimental approach

- The third step involved performing different SPR trials on plates that were made from the AlSi10MnMg-T7 alloy-heat treatment combination, to determine four suitable rivet-die combinations, see *Table 4.10*. These different combinations were then considered as a benchmark for the remainder of the joining trials.

The choice of the four rivet-die combinations was based on a joint evaluation criteria, which states that a good joint, such as the one shown in *Figure 4.32*, has to be symmetrical, shall have no crevice points under the aligned rivet head and that the rivet legs have to engage into the bottom sheet (interlock), while keeping a minimum non engaged thickness (t_{min}) (86). By checking all the cross sections in *Table 4.10*, it was concluded that all the above requirements for a good joint were fulfilled.

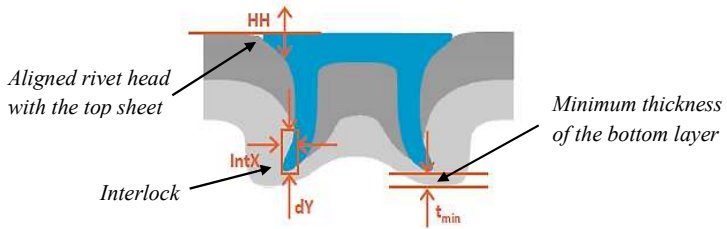


Figure 4.32: An example of a good SPR joint (86).

Table 4.10: The benchmark for the SPR trials.

1st combination		2nd combination		3rd combination		4th combination	
Rivet	Die	Rivet	Die	Rivet	Die	Rivet	Die
BG0542	EHG13	BG0542	EHG13	BG054	EHG140	BG0E4	EHG1
EHL0	209	EHL0	210	2EHL0	34	4EHL0	4033

As shown in *Table 4.10*, BG rivets were implemented due to their suitability in joining high strength steels to aluminium castings (87). In this study, two different BG rivets with different effective lengths were used. The BG0542EHL0 rivet with an effective length of 5 mm and the slightly shorter BG0E44EHL0 rivet with an effective length of 4 mm.

Unlike the Rivets, four different flat dies, similar to the design in *Figure 4.33*, were used for the SPR trials as represented in *Table 4.10*. Each of those dies had a distinctive diameter and depth combination, as seen in *Table 4.11*, to simulate different forming limits.

The largest forming limit was offered by the deepest die (EHG13209), whereas the smallest forming limit was offered by the shallowest die (EHG14033).

4. Experimental approach

Table 4.11: The specifications of the different dies.

Die	Depth(mm)	Diameter (mm)
EHG13209	2	11
EHG13210	1.5	12
EHG14034	1	12
EHG14033	0.5	12



Figure 4.33: The flat die design (88).

After setting the parameters above, the SPR trials were performed with the help of the Henrob SPR setup in *Figure 4.34*. During the trials, both the rivet and the die were applied manually to the top and the bottom nozzles of the setup.

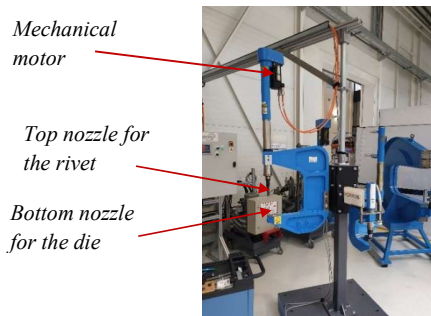


Figure 4.34: Henrob SPR setup for manual trials.

The joining proceeded by placing the DP600 steel samples on the top of the cast aluminium alloy samples. The reason behind this stack orientation's choice is the expected higher strength and energy absorption capability of the joint due to the larger interlock without excessive thinning of the thicker bottom sheet (89). Each material combination was then positioned between the nozzles in *Figure 4.34 (a)*, and the joint was made by forcing the rivet against the die with the help of a mechanical motor.

4. Experimental approach

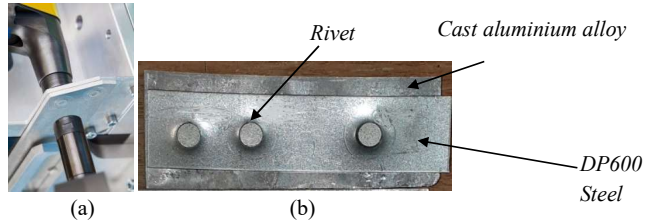


Figure 4.35: (a) The joint making using the SPR process (86) and (b) the connected structures.

For every material combination, cast Aluminium alloy and DP600 steel, three joints were made using each of the benchmarked rivet-die combinations as seen in *Figure 4.35(b)*. The next step involved accessing the joints, by checking mainly for radial and circumferential cracks, similar to the examples in *Figure 4.36*, on their outer bulging surfaces. The presence of such defects, which are an indication for reaching the forming limit, can cause a deterioration in the strength of the joint and can act as a favorable spot for galvanic corrosion (90).

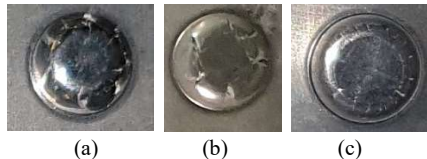


Figure 4.36: An example of the (a) circumferential cracks, (b) deep radial cracks and (c) light radial cracks.

The purpose of this assessment was to determine the rivetability of each of the investigated cast alloy-heat treatment-casting process combinations by detecting their forming limits, and to select their best rivet-die combination. According to *Atlas Copco*, if reliable joints could be made using different rivet–die combinations, then the best combination would be the one with the deepest die. This can be contributed to the larger penetration depth of the rivet (90) and to the less negative impact of the joining force on the lives of the die and the SPR machine.

The best rivet-die combination was then later used for a number of cast alloy-heat treatment-casting process combinations to develop the lap shear test samples. These samples, with the dimensions in *Figure 4.37*, were tested according to Ford's FLTM BA 157-02 standard at a test speed of 10 mm/min for the determination of the force-displacement behaviours of the joints



Figure 4.37: The 25 mm * 100 mm lap shear test samples.

In the case of the parts from supplier 3, the SPR trials were conducted directly on the parts without cutting any sections as shown in *Figure 4.38*. The assessment of the joints was carried

4. Experimental approach

as described earlier. However, no lap shear tests were performed in this case due to the difficulty in extracting the lap shear test samples from the supplier 3 parts.

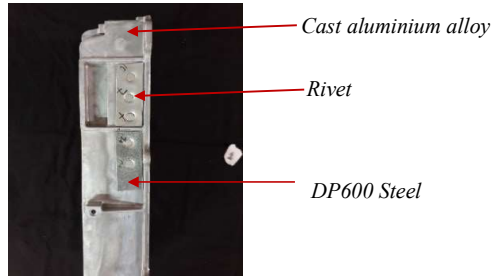


Figure 4.38: The SPR trials on the parts from supplier 3.

4.5.5 Evaluation of the results

In order to draw relevant conclusions from the performed tensile tests, bending tests, the density measurement of the plates and the self-piercing riveting tests, it was important to consider a number of different analytical tools.

These tools helped in providing a visual and an organized representation of the results, which therefore led to a better conclusion drawing process.

The two main tools used were *Minitab*, which made it possible to conduct accurate comparisons between the different parameters with the help of individual value plots, and *Microsoft Excel* that was used for the organization and the graphical representation of the results.

4.5.6 Microstructural analysis

The following steps were carried out for the microstructural analysis:

1. Extracting representative samples, as seen in *Figure 4.39*, from different locations in the plates and the parts.

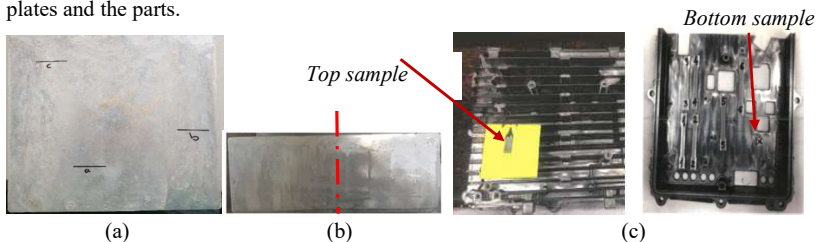


Figure 4.39: The location of the extracted samples from (a) the supplier 1 plates, (b) the supplier 2 plates and (c) the supplier 3 parts.

4. Experimental approach

As shown in *Figure 4.39*, three samples from three different positions were extracted from the supplier 1 plates. In the case of the supplier 2 plates and due to its relatively small size, only samples from the central position were used for microstructural analysis. On the hand and since the thickness is not constant within the supplier 3 parts, samples from the top (thinner) and the bottom (thicker) sections of the parts were needed for an accurate microstructural investigation.

2. Hot mounting of the extracted samples with acrylic resin at a temperature of 150 – 180 °C and a pressure of ~ 80 bar.



Figure 4.40: An example of a hot mounted sample.

3. Grinding the surfaces of the mounted samples, shown in *Figure 4.40*, with different SiC abrasive grinding papers, starting from the rough 120 grit paper until the very soft 2400 grit paper.
4. Polishing the samples on two different polishing cloths, by spraying a mixture of a solvent and a 3 μm diamond suspension on the first polishing cloth and a mixture of a solvent and a 1 μm diamond suspension on the second polishing cloth.
5. Taking pictures of the microstructures with the help of an optical light microscope.

For the samples from the suppliers 1 and 2 plates, the above steps were performed by supplier 1. However, for the samples from the supplier 3 parts, these steps were done by supplier 3.

4.5.7 SEM-EDS Analysis

Scanning electron microscopy (SEM) was implemented in this thesis to obtain microstructural images at higher magnifications and resolutions than those obtained using the optical light microscope. The SEM creates an image of the studied surface via the detection of the released electrons, by either the Backscattered electron detector (BSE) or the Secondary electron detector (SED). These electrons are released after subjecting the surface to a high energy electron beam in a vacuum condition (91).

Energy dispersive X-ray spectroscopy (EDS) was also applied in this thesis along with SEM, by supplier 1, to identify the different phases in the microstructures by subjecting the studied surface to a high energy electron beam and detecting the released X-rays with the help of an EDS detector (91).

4. Experimental approach

4.5.8 Optical Emission spectroscopy

The optical emission spectroscopy, which was mainly needed for the patents in *chapter 12*, was used for the determination of the exact chemical compositions of the alloys. This technique, especially spark spectroscopy, which was carried out at *Comptech AB* in Skillingaryd city, depends on measuring the intensity and the wavelength of the electromagnetic radiations that are emitted from various elements within the alloy (92).

4.6 Guidelines for testing

Detailed characterization of the test plates, from supplier 1, and the determination of the suitable testing guidelines were important first steps towards accurately evaluating the tensile and bending test results. For the sake of reaching this target, the investigations in *Table 4.12* were performed and their outcomes were accordingly evaluated.

Table 4.12: Test sequence for the characterization of supplier 1 test plates.

Purpose of the investigation	Set of parameters (Designation) from <i>Table 4.3</i> or <i>Table 4.5</i>	Test method	Sample form & orientation relative to the flow direction	Total number of tested samples for each designation *
(a) Determining the best location within the plates to extract the test samples	D-(3-650) & D-(50-4.63-575-1000)-R	Microstructural analysis	<ul style="list-style-type: none"> • Microstructural analysis' sample • Perpendicular 	3 S from 1 P (positions a,b &c)
(b) Determining the symmetry of the plates	D-(2.5-650)	Tensile test	<ul style="list-style-type: none"> •Type E •Longitudinal 	2 S from 1 P
(c) Determining the influence of the tensile test sample type on the results	D-(3.5-650)		<ul style="list-style-type: none"> •Type E & Mini samples •Longitudinal 	<ul style="list-style-type: none"> •15 TE from 5 P •15 Ms from 5 P
(d) Determining the suitable orientation of the samples	D-(3-650)		<ul style="list-style-type: none"> •Type E •Longitudinal & Perpendicular 	<ul style="list-style-type: none"> •10 Ls from 2 P •6 Ps from 2 P

4. Experimental approach

Table 4.12 (continued.)

(e) Determining the consistency of the HPDC process at supplier 1	D-(3.5-650)	<ul style="list-style-type: none">•Type E & Mini samples•Longitudinal	<ul style="list-style-type: none">•15 TE from 5 P•15 Ms from 5 P
---	-------------	--	---

* TE: Type E samples, Ms: Mini samples, S: Sample(s), P: Plate(s), Ls: Longitudinal samples and Ps: Perpendicular samples.

A detailed description of the different investigations and their outcomes are represented in the upcoming sections.

4.6.1 The best location within the plates

As mentioned earlier in *sections 2.3.4 & 2.4.3.4*, defects have a deteriorating effect on the resultant mechanical properties of the castings. The evolution of some of those defects, specifically the gas porosities and the gas blisters, can be linked to the gate design and the flow rate of the melt as represented in *Table 2.2*.

For the sake of deriving reliable conclusions about the investigated alloys and alloy-heat treatment combinations, it was therefore important to determine the best location within the plates, where the testing samples could be extracted. This was done by analyzing the microstructural images from a high pressure die casted plate (D-(3-650)) and a RheoMetal™ casted plate (D-(50-4.63-575-1000)-R). For each plate and as shown in *Figure 4.41*, a comparison between *positions a, b and c* was conducted.

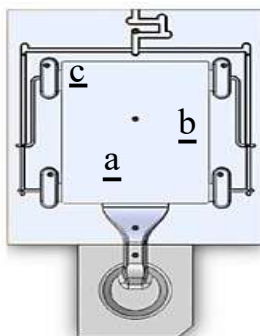



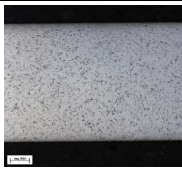

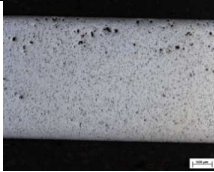


Figure 4.41: The positions a, b and c in the supplier 1 plates.

The images, represented in *Table 4.13*, were taken at a magnification of 25x to facilitate the detection of the defects.

4. Experimental approach

Table 4.13: The internal defects at the different locations of the supplier 1 plates.

Set of parameters (Designation) from Table 4.3 or Table 4.5	Position a	Position b	Position c
D-(3-650)			
D-(50-4.63-575- 1000)-R			

As seen in Table 4.13, different porosity levels were detected at the different positions in the plates. For the HPDC plate (D-(3-650)), the least porosity level was observed at *position a*. Similarly, the best soundness in the RheoMetal™ casted plate (D-(50-4.63-575-1000)-R) was also detected at *position a*.

Intermediate conclusion:

- Regardless of the gate design or the casting process, the least levels of internal defects were observed at the middle of the plates and close to the gates (*position a*). Based on this observation, it was concluded that the best location to extract the tensile test samples, bending test samples and microstructural analysis samples is *position a*.

4.6.2 The symmetry of the plates

An investigation about the symmetry of the plates was required in order to determine the possibility of drawing acceptable conclusions by comparing between the testing outcomes of the mirrored samples in the plates.

This investigation was first carried out by the uniaxial tensile testing of the two Type E samples (1&2) in Figure 4.42(b). These samples were extracted, as observed in Figure 4.41, from opposite positions along the symmetry line of the plate and close to the gate. The resultant total elongation values of both samples were then compared together, as shown in Figure 4.42(a).

4. Experimental approach

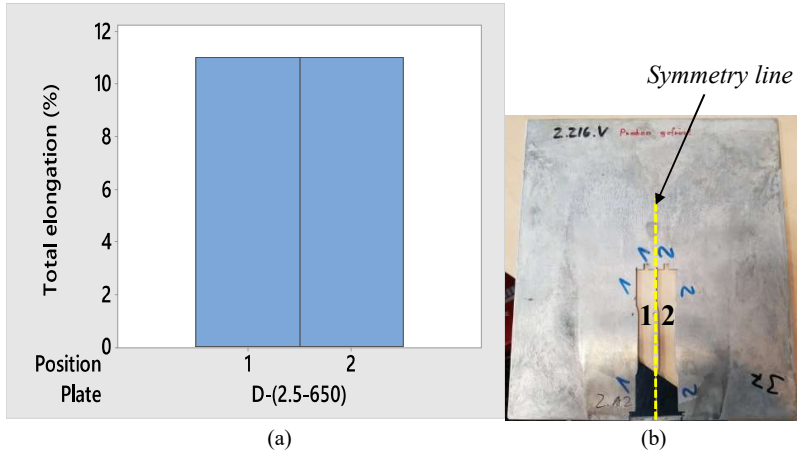


Figure 4.42: (a) The total elongation values (%) of the different samples and (b) their respective positions in the plates. (Designation from Table 4.3, P54)

The bar chart in *Figure 4.42(a)* illustrates that there was no detected difference between the total elongation values of the extracted samples.

Intermediate conclusion:

- As the positions of the samples in *Figure 4.42(b)* had no influence on the total elongation values, the plates from supplier 1 were considered to be symmetrical in their middle sections and close to their gates.
- As a result of the above point, it was concluded that tensile test samples, bending test samples and microstructural analysis samples could be extracted from both sides of the plate under the condition of being close to the symmetry line and in the vicinity of the gate.

4.6.3 The relevant tensile test sample

As mentioned earlier in *section 4.5.1*, two different sample types were used for the tensile testing trials. Therefore, in order to ensure that both sample types could efficiently characterize the studied alloys and alloy-heat treatment combinations and to make certain that comparisons between their testing outcomes could be made, an investigation had to be done.

This investigation involved extracting a total of 15 Type E samples and 15 mini samples from the middle sections and close to the gates of 5 different supplier 1 plates. These samples were then tested according to the tensile testing approach in *section 4.5.1* and the outcomes were compared together as shown below in *Figure 4.43*.

4. Experimental approach

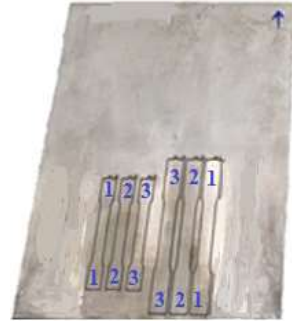
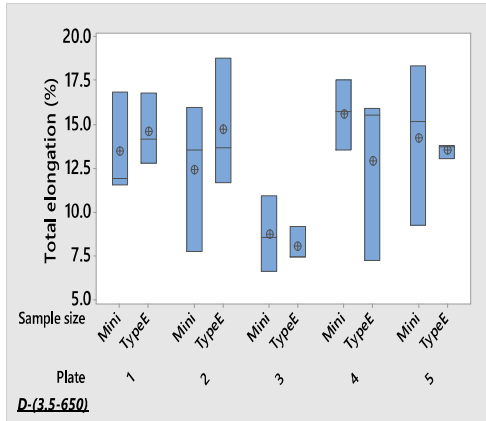


Figure 4.43: (a) The total elongation values (%) of the different sample types and (b) the outline of the samples in one of the investigated plates. (Designation from Table 4.3, P54)

As shown in *Figure 4.43(a)*, similar mean total elongation values (Θ) were obtained by both sample types. However, the larger samples (Type E) provided less variation in the total elongation values.

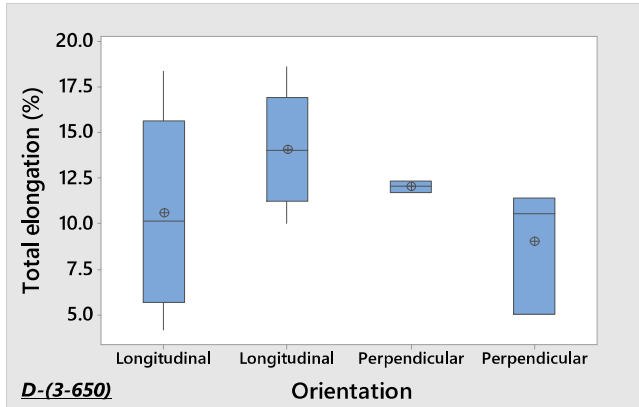
Intermediate conclusion:

- The sample type had no effect on the tensile test results, as similar outcomes were obtained by using the Type E and the mini samples in the tensile testing trials.
- Based on the above observation, it was concluded that both sample types could be used in the characterization of the castings.

4.6.4 The suitable orientation of the samples

For the sake of identifying whether the choice of the sample orientation was critical for the investigations or not, it was important to determine its influence on the testing outcomes. This was done by the tensile testing of a total of 16 longitudinal and perpendicular Type E samples.

4. Experimental approach



(a)



(b)

(c)

(d)

Figure 4.44: (a) The effect of the sample orientation on the total elongation values (%), (b) the positions of the longitudinal and perpendicular samples in respect to each other, (c) the location of the extracted longitudinal samples and (d) the location of the extracted perpendicular samples. (Designation from Table 4.3, P54)

The longitudinal samples (Figure 4.44 (c)) and the perpendicular samples (Figure 4.44 (d)) were extracted from four different plates. The locations of the longitudinal and perpendicular samples were defined in such a way that their middle sections would intersect together if placed in the same plate. This was important in ensuring a valid comparison between both sample orientations, as it made sure that the middle sections of the samples, where most of the deformation during tensile testing takes place, were overlapping.

As shown in Figure 4.44(a), similar tensile testing outcomes were obtained by using the longitudinal and the perpendicular samples. The larger variation in the results of the longitudinal samples can be however contributed to the larger number of tested samples (4 more than the perpendicular samples).

4. Experimental approach

Intermediate conclusion:

- After comparing between the tensile test results of the extracted perpendicular and longitudinal samples, it was concluded that the orientation of the samples in the plates had no influence on the mechanical properties.
- Based on the above point, it was considered acceptable to characterize the castings with the help of longitudinally or perpendicularly oriented samples.

4.6.5 The consistency of the casting process

The consistency of the HPDC process at supplier 1 was another aspect that had to be investigated. The purpose of this investigation, which was conducted using a total of 30 tensile test samples from 10 different plates, was to determine the ability of the supplier to produce reliable castings with a consistent and a repeatable quality.

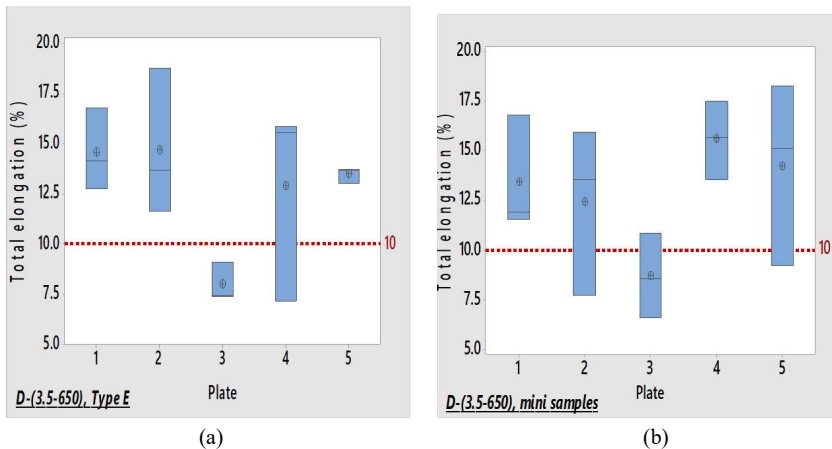


Figure 4.45: The consistency of the HPDC process at supplier 1 using the (a) Type E samples and the (b) mini tensile test samples. (Designation from Table 4.3, P54)

As seen in *Figure 4.45*, the results from all plates are close to and not extremely divergent from the industrially specified total elongation value of the cast alloy (2), which is represented by the red dotted lines in *Figure 4.45(a)* and *Figure 4.45(b)*.

Intermediate conclusion:

- A conclusion about the stability and the consistency of the HPDC process at the *Foundry Institute (GI) of the RWTH Aachen University* could be drawn. This is since similar plates

4. Experimental approach

were obtained along the casting process, and since most of the plates were able to meet the industrial specification of the cast alloy.

- The above point together with the outcomes from *sections 4.6.1, 4.6.2, 4.6.3 & 4.6.4*, have led to the overall conclusion that regardless of any sample size and orientation, reliable conclusions could be drawn from the supplier 1 plates by investigating the middle sections of those plates at locations close to the gate, e.g. *position a* in *Figure 4.41*.
- For the supplier 2 plates and the supplier 3 parts, the findings in *sections 4.6.2, 4.6.3, 4.6.4 & 4.6.5* were also considered to be valid. However, and due to their different gates' designs, the extraction of the samples was not restricted to their middle sections.

5. The investigations regarding the high pressure die casting process

5 The investigations regarding the high pressure die casting process

After analyzing the outcomes of the cost calculation study in *chapter 3*, it was clear that the choice of the alloy and its heat treatment requirement have the largest influence on the casting's cost. Therefore, testing the suitability of a number of different alloys, which either require a low-cost heat treatment process or preferably has no heat treatment requirement, was vital towards achieving the aim of deriving a cost-efficient process route for the mass production of thin walled structural aluminium body castings.

In this thesis and as mentioned earlier in *section 3.1*, the 2020 Ford explorer shock tower was the subject of the investigations. For this reason and as it was difficult to cast and thus perform the different tests on this shock tower, a number of alternatives (plates and parts) that satisfied its thickness and/or its dimensional requirements were instead casted by HPDC.

Prior to the HPDC trials, it was important to determine the optimum process parameters that could enable the retrieval of the best possible outcomes from the nine investigated alloys at supplier 1 and supplier 3. This was done by testing the impact of each of the different process parameters on the mechanical properties and the quality of the supplier 1 plates and the supplier 3 parts.

By extracting the microstructural and tensile test samples from the high pressure die casted plates and parts and then respectively analyzing and testing them, it was possible to accurately check whether the investigated alloys and alloy-heat treatment combinations could be suitable for the HPDC process and if they could reach the desired properties of the 2020 Ford explorer shock tower or not.

In addition, and as the 2020 Ford explorer shock tower is a crash relevant part, it was important to analyze the impacts of each HPDC alloy and alloy-heat treatment combination on the crash resistance potential of the castings and to compare these impacts to that of the currently implemented AlSi10MnMg-T7. These impacts on the crash resistance potential were retrieved by conducting 3-point bending tests on samples from the high pressure die casted plates and parts.

Furthermore, and as the 2020 Ford explorer shock tower is joined to the car body structure, most importantly to DP steel sheets, by the SPR joining method, it was necessary to evaluate the response of each of the different HPDC alloys and alloy-heat treatment combinations to this joining mechanism by visually evaluating the outer surfaces of four different SPR joints between the respective SPR samples and 1.3 mm DP steel sheets. The obtained responses were then compared to that of the currently implemented AlSi10MnMg-T7.

Each of the above steps is described in a separate section as follows.

5. The investigations regarding the high pressure die casting process

5.1 The optimum HPDC process parameters

As mentioned before in *section 2.3.2*, the melt flow velocity, especially during the 2nd phase (die filling), the intensification pressure and the vacuum condition are the main process parameters in HPDC that affect the soundness of the cast part.

Therefore, in order to facilitate the production of high-quality plates at supplier 1 and high-quality parts at supplier 3, it was important to derive the optimum values of these parameters. This was made possible for the HPDC trials at supplier 1 by analyzing the outcomes of the pre-trials, which were performed under vacuum condition. However, for the HPDC trials at supplier 3, the optimum values of the process parameters were defined based on information from the literature and on the supplier's recommendations.

The melt flow velocity in the shot sleeve (1st phase) was not investigated in this section. For the HPDC trials at supplier 1 and 3, a low piston velocity in the range of 0.2-0.223 m/s was assigned to this phase.

As seen in *Table 4.3*, no information was disclosed about the optimum process parameters for the externally produced plates at supplier 2.

5.1.1 The optimum HPDC process parameters to produce the plates at supplier 1

In order to determine the optimum process parameters for the production of the plates at supplier 1, the test sequence in *Table 5.1* was followed and implemented.

Table 5.1: The test sequence for the determination of the optimum HPDC test conditions.

Purpose of the investigation	Sets of parameters (Designations) from <i>Table 4.3</i>	Test method	Sample form & orientation relative to the flow direction	Total number of tested samples for each designation*
(a) Determining the optimum melt flow velocity in the die filling phase (2 nd phase) for the production of the supplier 1 plates	A-(2.5-650), A-(3-650) & A-(3.5-650)	•Tensile test •Density measurement	Tensile test: •Type E •Perpendicular	Tt: 9 S from 3 P Dm:3 P
	B-(2.5-650), B-(3-650) & B-(3.5-650)			
	C-(2.5-650), C-(3-650) & C-(3.5-650)			
	D-(2.5-650), D-(3-650) & D-(3.5-650)			Tt: average of 3 S from 1 P Dm: 1 P (D-(3.5-650)) 10 P (D-(3-650))

5. The investigations regarding the high pressure die casting process

Table 5.1 (continued.)

(b) Determining the optimum intensification pressure value	D-(3.5-650), D-(3.5-300) & D-(3-650)		Tt: 5 S from 5 P Dm: 10 P
--	---	--	--

* **Tt:** Tensile test, **Dm:** Density measurement, S: Sample(s), P: Plate(s).

The outcomes of the above test sequence are represented in *sections 5.1.1.1 and 5.1.1.2* as follows.

5.1.1.1 The optimum melt flow velocity

In order to determine the optimum melt flow velocity in the 2nd phase (die filling), it was important to analyze the mechanical properties and the porosity levels of the supplier 1 plates, which were produced from four different alloys using different piston velocities.

The reason beyond choosing to examine the results of more than one alloy is the contradiction in the literature about the influence of the melt flow velocity on the mechanical properties. This contradiction could have therefore led to misleading conclusions, if only the results from one alloy were to be considered.

For the AlMg4Fe2 alloy, the influence of the melt flow velocity on the total elongation (%) is illustrated in *Figure 5.1*.

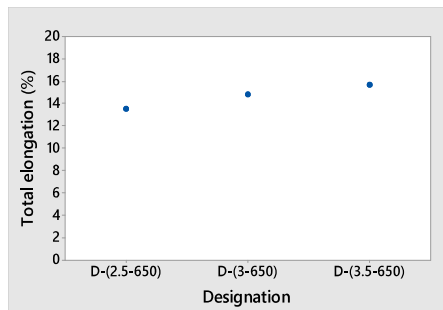


Figure 5.1: The influence of the melt flow velocity on the total elongation (%) of AlMg4Fe2. (*Designations from Table 4.3, P54*)

From *Figure 5.1*, it is obvious that at constant pressure values, increasing the melt flow velocity did result in a slight enhancement in the average total elongation values. The reason for such behaviour can be linked to the reduction in the porosity levels at the higher melt flow velocities, as seen in *Table 5.2*.

5. The investigations regarding the high pressure die casting process

Table 5.2: The porosity levels at different melt flow velocities for the AlMg4Fe2 alloy.

Alloy	Set of parameters (Designation) from Table 4.3	Ideal density (g/cm ³)	Average measured density (g/cm ³)	Porosity (%)
AlMg4Fe2	D-(3-650)	2.67	2.656	0.527
	D-(3.5-650)		2.67	0

The measured densities in Table 5.2, as well as in the other tables in sections 5.1.1.1 and 5.1.1.2, are the average of their corresponding plates' measured densities, which were in turn derived based on the approach in section 4.5.3. The porosity levels were calculated using equation (4.4), in which the ideal densities (ρ_0) were obtained from the alloys' supplier manual (2).

On the contrary and as shown in Figure 5.2, no clear trend between the melt flow velocity and the total elongation (%) could be found for the AlSi7Mg0.3 and the AlMg6Si2MnZr alloys.

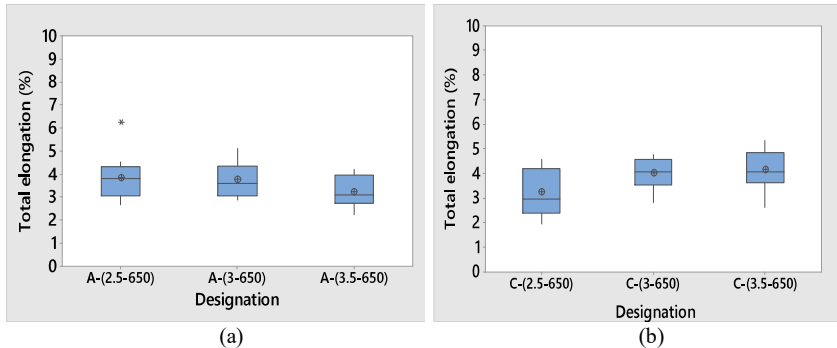


Figure 5.2: The influence of the melt flow velocity on the total elongation (%) of (a) AlSi7Mg0.3 and (b) AlMg6Si2MnZr. (Designations from Table 4.3, P54)

Similar to AlMg4Fe2, the porosity levels for each of the above alloys were measured at different melt flow velocities, as illustrated in Table 5.3, in order to determine the reason beyond the behaviours in Figure 5.2

Table 5.3: The porosity levels at different melt flow velocities for the AlSi7Mg0.3 and the AlMg6Si2MnZr alloys.

Alloy	Set of parameters (Designation) from Table 4.3	Ideal density (g/cm ³)	Average measured density (g/cm ³)	Porosity (%)
AlSi7Mg0.3	A-(2.5-650)	2.66	2.653	0.264
	A-(3-650)		2.664	0
	A-(3.5-650)		2.654	0.226

5. The investigations regarding the high pressure die casting process

Table 5.3 (continued.)

AlMg6Si2MnZr	C-(2.5-650)	2.64	2.598	1.617
	C-(3-650)		2.597	1.656
	C-(3.5-650)		2.598	1.617

By analyzing *Table 5.3* and comparing its entries to the outcomes in *Figure 5.2*, it was possible to state the following reason for the observed behaviours:

- The porosity levels of the AlSi7Mg0.3 and the AlMg6Si2MnZr alloys neither increased nor decreased by changing the melt flow velocity. This outcome is not seldom and could be related to Robert Karban's literature review (17), where one out of eleven previous researches showed no relation between the porosity content and the melt flow velocity.

A third observation about the deterioration in the mechanical properties at higher melt velocities was detected for AlMg5Si2Mn after assessing *Figure 5.3*. The reason for such behaviour can be linked to the increase in the porosity levels at the higher melt velocities as seen in *Table 5.4*.

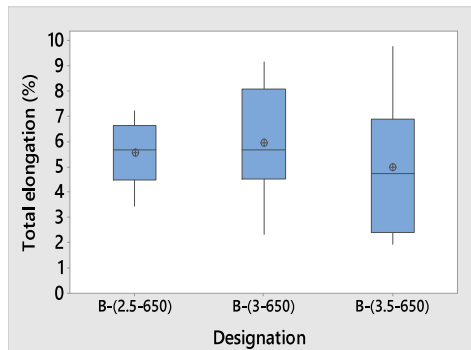


Figure 5.3: The influence of the melt flow velocity on the total elongation (%) of AlMg5Si2Mn. (*Designations from Table 4.3, P54*)

Table 5.4: The porosity levels at different melt flow velocities for the AlMg5Si2Mn alloy.

Alloy	Set of parameters (Designation) from <i>Table 4.3</i>	Ideal density (g/cm ³)	Average measured density (g/cm ³)	Porosity (%)
AlMg5Si2Mn	B-(2.5-650)	2.63	2.633	0
	B-(3-650)		2.634	0
	B-(3.5-650)		2.62	0.381

5. The investigations regarding the high pressure die casting process

Intermediate conclusions:

- Similar to the literature review in *section 2.3.2*, there was a contradiction in the influence of the melt flow velocity on the mechanical properties.
- For most cases, there was a direct relation between the mechanical properties and the porosity levels.
- Changing the melt flow velocity during die filling did not play a major role in affecting the mechanical properties. In other words, the mechanical properties were either not affected or were slightly affected by changing the melt flow velocity.
- Due to the previous three remarks, no optimum melt flow velocity could be defined.

5.1.1.2 The optimum intensification pressure

As mentioned earlier in *section 2.3.2*, an increase in the intensification pressure enhances the mechanical properties of the casting by reducing its pore content. For this reason and as illustrated in this section, it was important to determine an optimum intensification pressure value that can be used for the production of the plates.

As there was no contradiction in literature about the influence of this parameter on the mechanical properties, it was acceptable to use the test results from a single alloy.

In this investigation, the considered alloy was AlMg4Fe2. The influence of the intensification pressure on the resultant mechanical properties and on the porosity levels of this alloy are represented in *Figure 5.4* and *Table 5.5*.

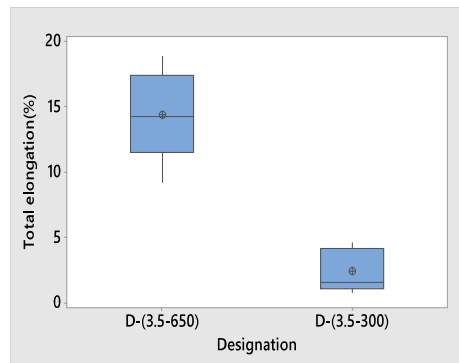


Figure 5.4: The influence of the intensification pressure on the total elongation (%) of AlMg4Fe2. (Designations from *Table 4.3, P54*)

5. The investigations regarding the high pressure die casting process

Table 5.5: The porosity levels at different intensification pressure values for the AlMg4Fe2 alloy.

Alloy	Set of parameters (Designation) from Table 4.3	Ideal density (g/cm ³)	Average measured density (g/cm ³)	Porosity (%)
AlMg4Fe2	D-(3-650)	2.67	2.656	0.527
	D-(3.5-300)		2.588	3.168

As seen in *Figure 5.4* and *Table 5.5* increasing the intensification pressure from 300 bar to 650 bar has led to an increase in the average total elongation value by approximately 12 % and a decrease in the porosity level by approximately 2.6 %.

Intermediate conclusion:

- Increasing the intensification pressure has caused an enhancement in the mechanical properties by reducing the porosity levels in the castings.
- An optimum intensification pressure of 650 bar was defined for the HPDC trials at supplier 1. This explains the reason beyond implementing this pressure value in most of the trials in *Table 4.3*.

5.1.2 The optimum HPDC process parameters to produce the parts at supplier 3

Unlike the previous section, no detailed investigation was performed to determine the optimum process parameters to produce the parts at supplier 3. However, by considering the findings of *section 5.1.1.1*, *section 5.1.1.2*, the literature review in *section 2.3.2* and the supplier's recommendations, it was possible to obtain optimum melt flow velocity and intensification pressure values for the production of the parts.

5.1.2.1 The optimum melt flow velocity

As mentioned earlier in *section 2.3.2*, a maximum gate velocity of 40 m/s had to be chosen during the second phase (die filling) to avoid die erosion. This information together with the recommendation from supplier 3 had led to the choice of 25.63 m/s to be the gate velocity.

This velocity was transformed to a piston velocity of 5.23 m/s with the help of the equations in *section 2.4.3.2*.

The inputs for those equations were the gate area, which was calculated based on the gate dimensions in *Table 4.6* and the piston area, which was calculated after taking the piston diameter of 100 mm into consideration.

5. The investigations regarding the high pressure die casting process

Intermediate conclusion:

- A piston velocity of 5.23 m/s in the second phase (die filling) was considered suitable for the production of the parts at supplier 3.

5.1.2.2 The optimum intensification pressure

As the choice of the intensification pressure is based on the size of the gate, the optimum pressure value for the gate design at Supplier 1 (650 bar) was not considered to be valid for the gate design at supplier 3. Therefore, and due to the larger gate at supplier 3, a smaller intensification pressure value had to be applied to prevent its transition into the casting (93).

Based on the previous remark, the gate dimensions in *Table 4.6*, and on supplier 3's recommendation, an intensification pressure value of 340 bar was chosen for the production of the parts.

Intermediate conclusion:

- An intensification pressure value of 340 bar was assigned to the HPDC trials at supplier 3.
- This intensification pressure value, which is lower than its counterpart in *section 5.1.1.2*, was chosen due to the larger area of the gate.

5.2 Characterization of the different HPDC alloys and alloy-heat treatment combinations

As mentioned earlier at the beginning of *chapter 5*, the accurate characterization and evaluation of the different HPDC alloys and alloy-heat treatment combinations was considered as an important stage towards reaching the aim of this thesis. This stage was conducted by:

1. Assessing the microstructures of the different alloys and alloy-heat treatment combinations and determining the possible defects that might develop during their use in the casting process.
2. Comparing between the mechanical testing outcomes of the different alloys and alloy-heat treatment combinations, and correlating these outcomes to the mechanical requirements of the 2020 Ford explorer shock tower.

As seen from the designations in *Table 5.6*, the evaluated plates, from supplier 1 and 2, and parts, from supplier 3, were made from the different alloys using the optimum process parameters in *section 5.1*.

5. The investigations regarding the high pressure die casting process

Table 5.6: The test sequence for the comparison between the different HPDC alloys and alloy-heat treatment combinations.

Purpose of the investigation	Set of parameters (Designation) from Table 4.3 or Table 4.9	Test method	Sample form & orientation relative to the flow direction	Total number of tested samples for each designation*
a) To provide an accurate characterization of the HPDC alloys that were used for the casting of the plates at supplier 1 and 2	H	Tensile test	Tensile test: •Mini samples •Longitudinal	Tt: 19 S from 9 P Ma: 1 S
	H-T5			Tt: 12 S from 3 P Ma: 1 S
	H-T7			Tt: 6 S from 2 P Ma: 1 S
	I			Tt: 5 S from 2 P Ma: 1 S
	I-T5			Tt: 9 S from 2 P Ma: 1 S
	D-(3.5-650) / D-(3-650)			Tt: 15 S from 5 P Ma: 1 S (position a)
	A-(3.5-650) / A-(3-650)			Tt: 6 S from 2 P Ma: 1 S (position a)
	B-(3.5-650) C-(3.5-650)			
b) To accurately characterize the HPDC alloys that were used for the casting of the parts at supplier 3	E-(730)	Microstructural analysis	Tensile test: •Mini samples •Longitudinal	Tt: 6 S from 1 Pa Ma: 1 S (gate side)
	F-(740)			
	G-(755)			

* **Tt:** Tensile test, **Ma:** Microstructural analysis, **S:** Sample(s), **P:** Plate(s), **Pa:** Part (s).

5.2.1 Characterization of the HPDC alloys and alloy-heat treatment combinations that were used at the suppliers 1 and 2

As mentioned before, the characterization of the alloys and alloy-heat treatment combinations involved performing a detailed microstructural investigation and a comparison between their resultant mechanical properties.

For the HPDC alloys and alloy-heat treatment combinations that were used at supplier 1 and 2, these two stages are represented in *section 5.2.1.1* and *section 5.2.1.2* as follows.

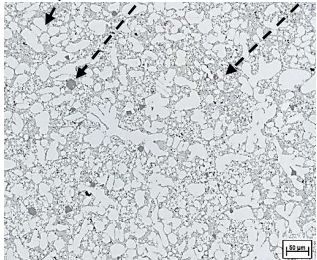

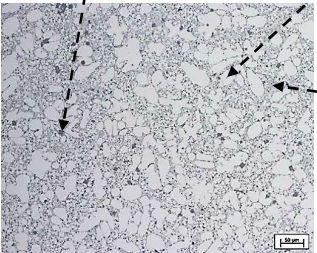
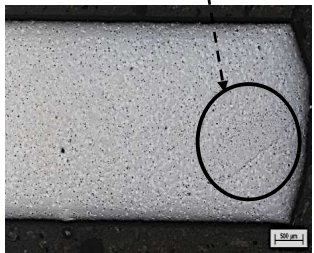
5. The investigations regarding the high pressure die casting process

5.2.1.1 Microstructural investigation of the HPDC alloys and alloy-heat treatment combinations that were used at the suppliers 1 and 2

Analyzing the microstructural constitution and the defects that may accompany the use of each alloy in the HPDC process was a required stage for the accurate differentiation between these alloys and for determining the reasons beyond the differences in their mechanical properties.

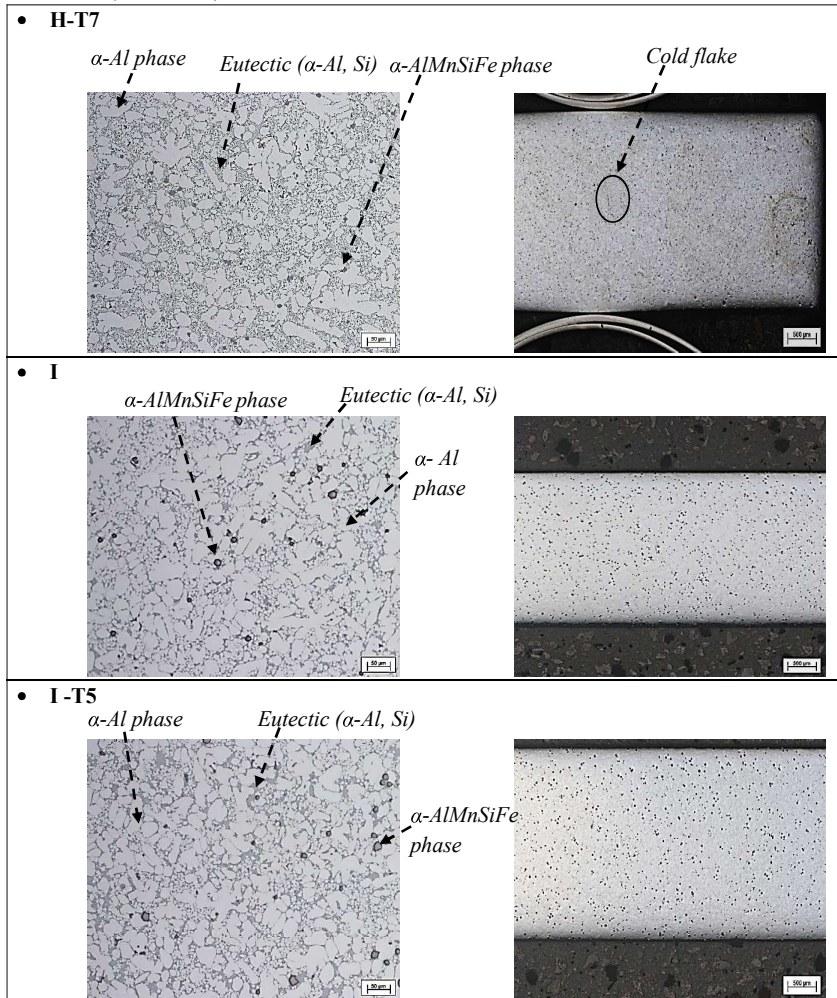
In this thesis, the microstructural investigation was performed for each alloy and alloy-heat treatment combination by evaluating their 25x and 200x microstructural images, which were taken with the help of an optical light microscope. The 200x images were used specifically to highlight the different phases, which were identified with the help of the SEM-EDS analysis technique. On the other hand, the low magnification images (25x) were used to provide an overview about the defects that occurred across the studied cross sections. A representation of the different microstructural images for each designation, from Table 4.3, is shown in Table 5.7 as follows.

Table 5.7: The 200x and 25x microstructural images of the HPDC alloys and alloy-heat treatment combinations that were used at supplier 1 and 2. (Designations from Table 4.3, P54)

Magnification	
200x	25x
<p>• H</p>  <p><i>α-Al phase</i> <i>α-AlMnSiFe phase</i> <i>Eutectic (α-Al, Si)</i></p> <p style="text-align: right;">20 μm</p>	 <p style="text-align: right;">500 μm</p>
<p>• H-T5</p>  <p><i>α-AlMnSiFe phase</i> <i>α-Al phase</i> <i>Eutectic (α-Al, Si)</i></p> <p style="text-align: right;">20 μm</p>	 <p><i>Cold flake</i></p> <p style="text-align: right;">500 μm</p>

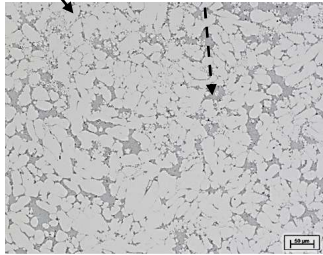
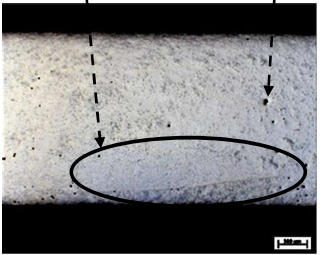
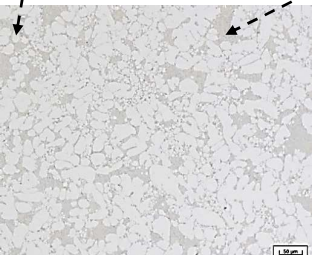
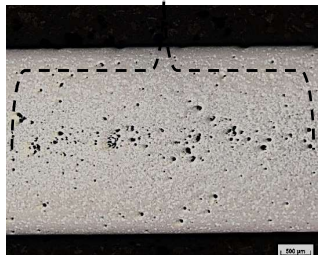
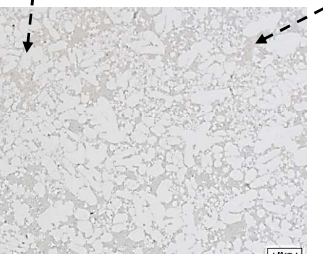
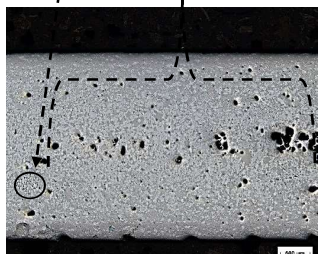
5. The investigations regarding the high pressure die casting process

Table 5.7 (continued.)



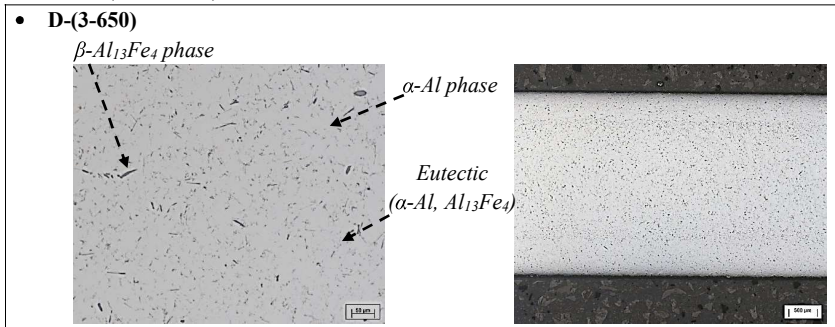
5. The investigations regarding the high pressure die casting process

Table 5.7 (continued.)

<ul style="list-style-type: none">A-(3-650)  <p><i>α-Al phase</i> <i>Eutectic (α-Al, Si)</i></p> <p>This micrograph shows a fine, granular structure. The α-Al phase is represented by the lighter, more irregularly shaped regions, while the eutectic structure is the darker, more uniform matrix. A scale bar in the bottom right corner indicates 100 μm.</p>	 <p><i>Cold flake</i> <i>Shrinkage porosities</i></p> <p>This macrograph shows a cross-section of the casting. A large, dark, irregularly shaped region is circled in black and labeled as a cold flake. Several smaller, dark spots are scattered throughout the lighter matrix, labeled as shrinkage porosities. A scale bar in the bottom right corner indicates 100 μm.</p>
<ul style="list-style-type: none">B-(3.5-650)  <p><i>α-Al phase</i> <i>Eutectic (α-Al, Mg₂Si)</i></p> <p>This micrograph shows a structure similar to A-(3-650) but with a different eutectic composition. The α-Al phase is the lighter, irregular regions, and the eutectic structure is the darker matrix. A scale bar in the bottom right corner indicates 100 μm.</p>	 <p><i>Shrinkage porosities</i></p> <p>This macrograph shows a cross-section of the casting with a dashed rectangular box highlighting a region containing numerous small, dark spots, which are identified as shrinkage porosities. A scale bar in the bottom right corner indicates 100 μm.</p>
<ul style="list-style-type: none">C-(3.5-650)  <p><i>α-Al phase</i> <i>Eutectic (α-Al, Mg₂Si)</i></p> <p>This micrograph shows a structure similar to B-(3.5-650) but with a different eutectic composition. The α-Al phase is the lighter, irregular regions, and the eutectic structure is the darker matrix. A scale bar in the bottom right corner indicates 100 μm.</p>	 <p><i>Cold flake</i> <i>Shrinkage porosities</i></p> <p>This macrograph shows a cross-section of the casting with a dashed rectangular box highlighting a region containing numerous small, dark spots (shrinkage porosities) and a larger, dark, irregularly shaped region (cold flake). A scale bar in the bottom right corner indicates 100 μm.</p>

5. The investigations regarding the high pressure die casting process

Table 5.7 (continued.)



Analysing the above 200x microstructural images in Table 5.7 shows that each of the investigated microstructures consists of a primary $\alpha\text{-Al}$ phase, with a dendritic morphology, a eutectic and, even if not illustrated, at least a single intermetallic phase.

The evaluation of the 25x images showed that the plates casted at supplier 2 had less defects than those casted at supplier 1. Furthermore, unlike the supplier 2 plates, the entire supplier 1 plates had a higher fraction of the $\alpha\text{-Al}$ phase and a larger grain size at the middle of their cross sections. Moreover, and as seen in the 25x images, the largest number and volume of casting defects were detected in the plates of AlMg5Si2Mn (B-(3.5-650)) and AlMg6Si2MnZr (C-(3.5-650)).

Intermediate conclusion:

- The plates casted at supplier 2 were more homogenous than those casted at supplier 1.
- The least suitable alloy-process parameters combinations for the HPDC of the plates were AlMg5Si2Mn (B-(3.5-650)) and AlMg6Si2MnZr (C-(3.5-650)). This conclusion is based on the fact that their microstructures were composed of a large volume of shrinkage porosities.
- The above outcome doesn't however exclude the AlMg5Si2Mn and AlMg6Si2MnZr alloys from being suitable to the production of structural body castings via the HPDC process. This is due to the possibility of decreasing their microstructural defects, in particular the shrinkage porosities, by several ways such as adjusting the process parameters, changing the gate design and by controlling the die temperature.
- All the other alloy-process parameters combinations, such as AlSi10MnMg, AlSi7MnMg, AlSi7Mg0.3 (A-(2.5-650)) and AlMg4Fe2 (D-(3-650)), were suitable for the HPDC of the plates as no defects could be visually detected in their microstructures.
- The above conclusion does not exclude the possibility that there can still be other visually undetectable defects in the nanometer range (e.g. precipitates) and/or defects in other regions of the castings that can negatively impact the resultant mechanical properties of the castings.

5. The investigations regarding the high pressure die casting process

5.2.1.2 The mechanical properties of the HPDC alloys and alloys-heat treatment combinations that were used at the supplier 1 and 2

As mentioned earlier in *section 5.2*, the comparison between the mechanical testing outcomes was considered as a second step for the accurate characterization of the different alloys and alloy-heat treatment combinations. The chosen test for this purpose was the tensile test.

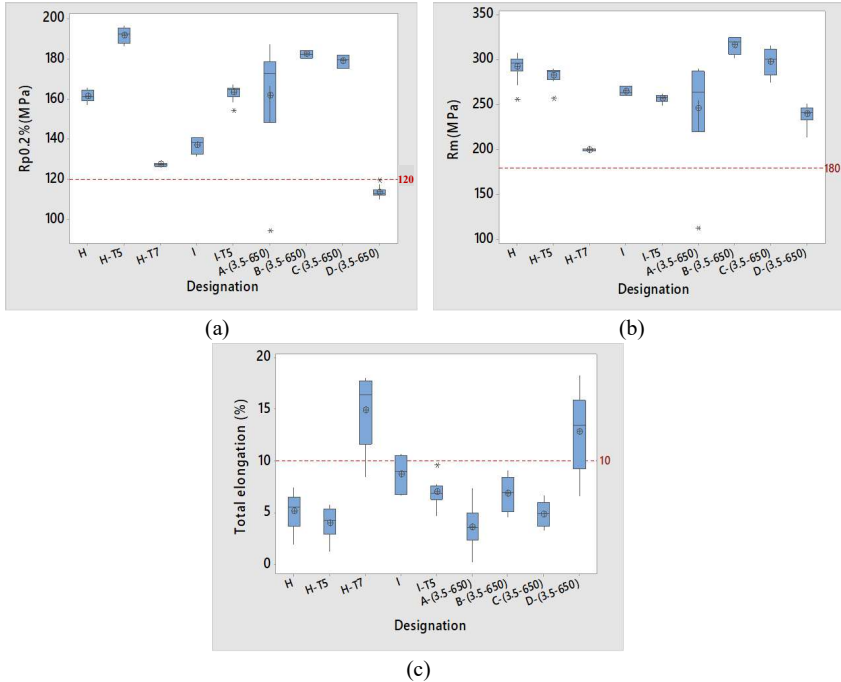


Figure 5.5: The comparison between the different HPDC alloys and alloy-heat treatment combinations in terms of their (a) Rp0.2 values (MPa), (c) Rm values (MPa) and (c) total elongation values (%). (Designations from *Table 4.3, P54*)

Figure 5.5 illustrates the Rp0.2, Rm and total elongation values of all the different HPDC alloys and alloy-heat treatment combinations that were used at supplier 1 and 2. The respective mechanical requirements of the 2020 Ford explorer shock tower refer to values greater than those represented by the broken line in the above figure.

As seen in *Figure 5.5(a)*, most of the alloys and alloy-heat treatment combinations were able to meet the yield strength requirement of the shock tower. However, AlMg4Fe2 (D-(3.5-650)) was the single alloy that had a slightly lower value than 120 MPa.

5. The investigations regarding the high pressure die casting process

Unlike *Figure 5.5(a)*, *Figure 5.5(b)* shows that there were no exceptions in terms of the alloys and alloy-heat treatment combinations that had higher ultimate tensile strength values than 180 MPa.

The total elongation (%) chart demonstrates a different outcome than its Rp0.2 and Rm counterparts. By analyzing *Figure 5.5(c)*, AlMg4Fe2 (D-(3.5-650)) and AlSi10MnMg-T7 (H-T7) were respectively found to be the alloy and alloy-heat treatment combination with higher average total elongation values (Θ) than 10%. However, this does not necessarily mean that the alloys with slightly lower average total elongation values than 10 %, such as AlSi7MnMg (I), won't be able to fulfil the joining requirements and thus be suitable for the 2020 Ford explorer shock tower.

The reasons beyond the mechanical testing outcomes in *Figure 5.5* can be related to a number of factors such as the chemical composition of the alloys, the morphology and size of their different phases, the heat treatment process and the process parameters and conditions that have an influence on the microstructural defects' evolution.

In addition and based on the remarks in *section 2.3.3*, the thickness of the plates can be also regarded as an influencing factor due to its effect on the cooling rate during solidification and thus its influence on the overall soundness of the casting. In other words, and in order to facilitate the comparison between the outcomes from the different suppliers, where the tensile test samples have been extracted from plates with different thicknesses and where respective optimum process parameters were used, the inverse proportionality between the plate thickness and the resultant Rp0.2, R_m and total elongation values had to be taken into consideration.

Intermediate conclusion:

- The Ford explorer shock tower's yield strength and ultimate tensile strength requirements were fulfilled by most of the investigated alloys and alloy-heat treatment combinations, including AlMg5Si2Mn (B-(3.5-650)) and AlMg6Si2MnZr (C-(3.5-650)). This observation indicates that even with the presence of a large volume of microstructural defects, as seen in *Table 5.7*, it was still possible to achieve the required Rp0.2 and Rm values.
- Due to the difference in the thickness between the plates from supplier 1 and supplier 2, it should be noted that the recorded values in *Figure 5.5* are expected to be different (better for the alloys casted at supplier 1 and worse for the alloys casted at supplier 2), if the alloys from the different suppliers were to be casted into the other suppliers' plates.
- Due to the ability of AlMg4Fe2 (D-(3.5-650)) and AlSi10MnMg-T7 (H-T7) to achieve higher total elongation values than 10%, both of them can be considered as suitable candidates for the production of the 2020 Ford explorer shock tower with the help of the HPDC process.

5. The investigations regarding the high pressure die casting process

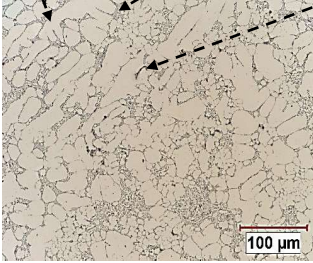
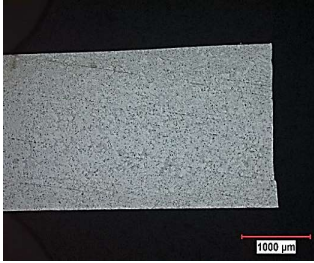
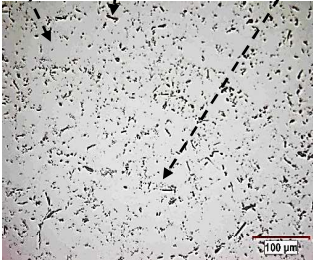
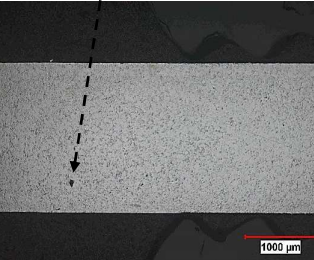
5.2.2 Characterization of the HPDC alloys that were used at supplier 3

The microstructural investigation and the mechanical properties of the HPDC alloys, which were used at supplier 3, are represented in *section 5.2.2.1* and *section 5.2.2.2* as follows.

5.2.2.1 Microstructural investigation of the HPDC alloys that were used at supplier 3

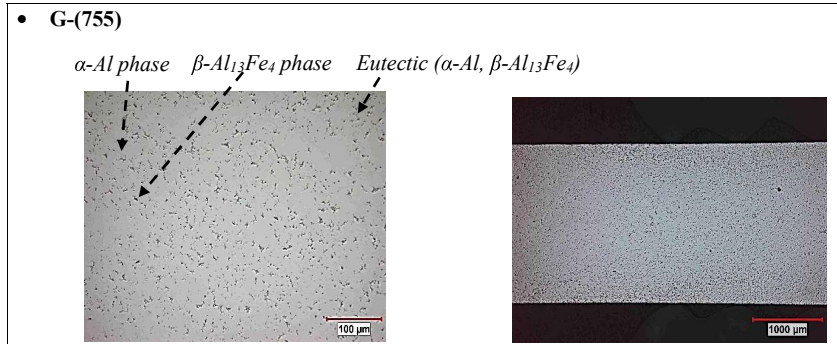
The microstructural investigation was conducted in a similar manner to that mentioned in *section 5.2.1.1*. A representation of the different microstructural images for each designation, from *Table 4.9*, is shown in *Table 5.8* as follows.

Table 5.8: The 200x and 25x microstructural images of the HPDC alloys that were used at supplier 3. (Designations from *Table 4.9*, P65)

Magnification	
200x	25x
<ul style="list-style-type: none"> E-(730) <div style="display: flex; justify-content: space-around; align-items: flex-start;"> <div style="text-align: center;"> <p><i>α-Al phase</i></p>  <p>100 μm</p> </div> <div style="text-align: center;"> <p><i>Fe-rich intermetallic phase</i></p>  <p>1000 μm</p> </div> </div> 	
<ul style="list-style-type: none"> F-(740) <div style="display: flex; justify-content: space-around; align-items: flex-start;"> <div style="text-align: center;"> <p><i>α-Al phase</i></p> <p><i>β-Al₁₃Fe₄ phase</i></p> <p><i>Eutectic (α-Al, β-Al₁₃Fe₄)</i></p>  <p>100 μm</p> </div> <div style="text-align: center;"> <p><i>Shrinkage porosity</i></p>  <p>1000 μm</p> </div> </div> 	

5. The investigations regarding the high pressure die casting process

Table 5.8 (continued.)



The analysis of the above 200x microstructural images in Table 5.8 shows that the each of the investigated microstructures consists of a primary α -Al phase, with a dendritic morphology, a eutectic and at least a single intermetallic phase.

Similar to the supplier 1 plates and as seen in the above 25x images, a higher fraction and a larger size of the α -Al phase were detected at the middle of the cross sections of the supplier 3 parts. In addition, no/negligible defects were detected at this magnification.

Intermediate conclusion:

- The scarcity of the visually detectable defects in the 25x microstructural images was an indication that the three investigated alloy-process parameters combinations (EN AB-42000 (E-(730)), AlMg4Fe2 (F-(740)) and MYFORD (G-(755))) were suitable for the HPDC of the parts at supplier 3.
- The above conclusion does not rule out the possibility that there can still be other visually undetectable defects in the nanometer range (e.g. precipitates) and/or defects in other regions of the castings that can negatively impact the resultant mechanical properties of the castings.

5. The investigations regarding the high pressure die casting process

5.2.2.2 The mechanical properties of the HPDC alloys that were used at supplier 3

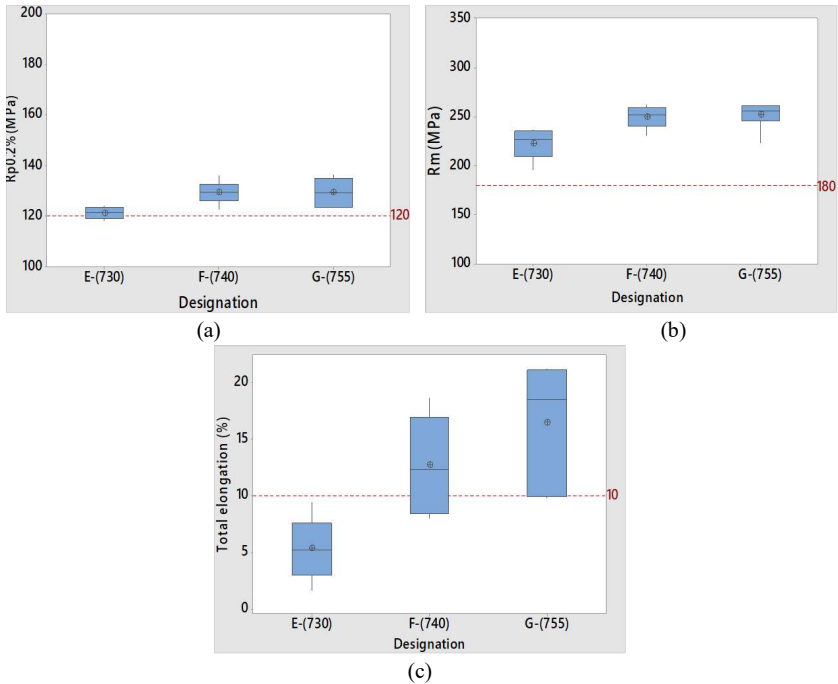


Figure 5.6: The comparison between the different HPDC alloys in terms of their (a) Rp0.2 values (MPa), (c) Rm values (MPa) and (c) total elongation values (%). (Designations from Table 4.9, P65)

The Rp0.2, the Rm and the total elongation values of the HPDC alloys that were used at supplier 3 are shown in Figure 5.6. Similar to Figure 5.5, the mechanical requirements of the 2020 Ford explorer shock tower also refer to values, which are higher than those represented by the broken lines in Figure 5.6.

As seen in Figure 5.6(a), all the considered alloys were able to meet the yield strength requirement of the shock tower. This includes the AlMg4Fe2 alloy (F-(740)), which had previously illustrated, during the plate casting trials at supplier 1, slightly lower values than the 120 MPa limit. In addition and as shown in Figure 5.6(b), the ultimate tensile strength requirement of greater than 180 MPa was also met by the three alloys.

On the other hand and as seen in Figure 5.6(c), EN AB-42000 (E-(730)) was the only alloy, which was not able to achieve a higher total elongation value than 10 %.

5. The investigations regarding the high pressure die casting process

By comparing between the MYFORD (G-(755)) and the AlMg4Fe2 (F-(740)) alloys, it is obvious that G-(755) had a higher average total elongation value (\oplus) than F-(740). In addition, and although the total elongation values were largely scattered for both alloys, all the values for G-(755) were higher than 10%. This however doesn't exclude the AlMg4Fe2 alloy from being a suitable candidate for the 2020 Ford explorer shock tower, as its average total elongation value, which can be further enhanced by implementing an additional adjustment to the process parameters, did meet the requirement of 10%.

Intermediate conclusion:

- EN AB-42000 (E-(730)) is not considered suitable to produce the 2020 Ford explorer shock tower by HPDC, due to its inability to meet the total elongation requirement of more than 10%.
- Although MYFORD (G-(755)) was capable of providing higher average total elongation value than the AlMg4Fe2 (F-(740)), both alloys are still considered suitable for the production of the 2020 Ford explorer shock tower by the HPDC process. This is because they were both able to meet the mechanical requirements for this structural body part during the casting trials at supplier 3.

5.3 The impacts of the HPDC alloys and alloy-heat treatment combinations on the crash resistance potential of the casting

Most of the structural body parts have to be, up to a certain extent, resistant to crash. In other words, they must be able to absorb enough energy prior to fracture for a better passengers' safety. Therefore, checking the impacts of the different alloys and alloy-heat treatment combinations on the crash resistance potential of the investigated casting was regarded as an important aspect that had to be looked into within the framework of this thesis.

The main aim of this investigation was to determine which of the considered HPDC alloys and alloy-heat treatment combinations can result in a higher crash resistance potential for the 2020 Ford explorer shock tower. To achieve this aim, different plates and parts, which were produced using *section 5.1's* optimum process parameters, had to be tested according to the test sequence in *Table 5.9*.

5. The investigations regarding the high pressure die casting process

Table 5.9: The test sequence for determining the influences of the HPDC alloys and alloy-heat treatment combinations on the crash resistance potentials of the castings.

Purpose of the investigation	Set of parameters (Designation) from Table 4.3 or Table 4.9	Test method	Sample form	Total number of tested samples for each designation
(a) To determine and compare between the HPDC alloys and alloy-heat treatment combinations' impacts on the crash resistance potentials of the plates from supplier 1 and 2	H	•3-point bending test	The 3-point bending test Samples in <i>Figure 4.27</i>	12 bending samples from 3 different plates
	H-T5			
	H-T7			
	I			
	I-T5			
	A-(3.5-650)			
	B-(3.5-650)			
	C-(3.5-650)			
D-(3-650)	•Simulation of the 3-point bending test			
(b) To determine and compare between the HPDC alloys' impacts on the crash resistance potentials of the parts from supplier 3		E-(730)		
		F-(740)		
G-(755)				

The findings of the sub investigations, ((a) and (b)) in the above test sequence, are represented in *sections 5.3.1 and 5.3.2* as follows.

5.3.1 The impacts of the HPDC alloys and alloy-heat treatment combinations on the crash resistance potentials of the plates from the suppliers 1 and 2

The first step towards determining the crash resistance behaviour was to subject the plates to the 3-point bending test, which is described earlier in *section 4.5.2*.

For each of the investigated alloys and alloy-heat treatment combinations, 12 bending samples from 3 different plates were tested. The sample that resembled the average outcome was then selected in the analysis as a representative to its respective alloy or alloy-heat treatment combination.

For the Al-Si alloys and alloy-heat treatment combinations, the bending test results are shown in *Figure 5.7* as follows.

5. The investigations regarding the high pressure die casting process

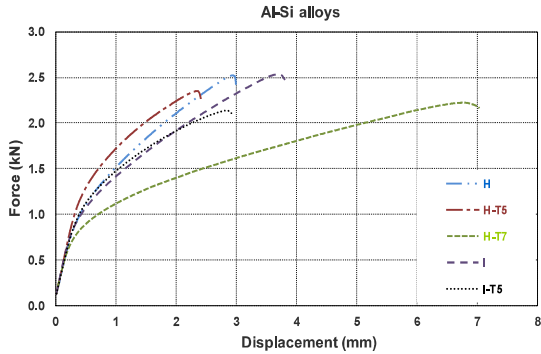


Figure 5.7: The force-displacement chart of the Al-Si alloys and alloy-heat treatment combinations. (Designations from Table 4.3, P54)

The second step towards determining the crash resistance potential involved calculating the total area under each force-displacement curve. This area resembles the energy absorption by the plate and ultimately its crash resistance potential. For a better representation of the crash resistance potentials, energy-displacement graphs, such as Figure 5.8, were plotted for the investigated alloys and alloy-heat treatment combinations.

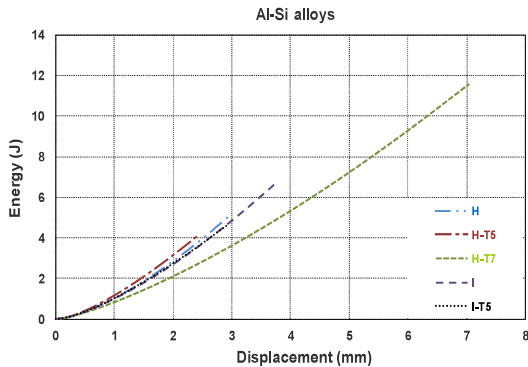


Figure 5.8: The energy-displacement diagram of the Al-Si alloys and alloy-heat treatment combinations. (Designations from Table 4.3, P54)

A simulation of the 3-point bending test results for the Al-Si alloys and alloy-heat treatment combinations had to be done for the sake of an accurate comparison between them, casted into 2.5 mm thick plates, and the rest of the alloys, which were casted into 3.1 mm thick plates. The function of this simulation, which was constructed with the help of the *Altair RADIOSSTM* software, was to predict the outcomes of the 3-point bending test when performed on a different

5. The investigations regarding the high pressure die casting process

plate thickness. The simulation calculations were set up and carried out by the Vehicle Systems Engineering and Technologies department of *Ford Werke GmbH* in Aachen city.

For validation purposes, a simulation of the 3-point bending test on a 2.5 mm thick plate was first done and the outcomes from this simulation were then compared to the real test results in *Figure 5.7*.

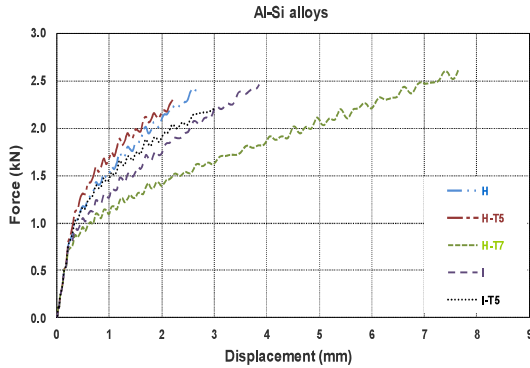


Figure 5.9: The simulated force-displacement chart of the Al-Si alloys and alloy-heat treatment combinations. (*Designations from Table 4.3, P54*)

Unlike the curves in *Figure 5.7*, the curves in *Figure 5.9* are not smooth. This difference in the curves' appearance was mainly due to the dependence of the simulation on an explicit solver (dynamic model), which unlike the much slower real trials, causes an increase in the oscillation of the 3-point bending plates during the acceleration of the punch and results in the jagged appearance of the curves.



Figure 5.10 : The simulated energy-displacement chart of the Al-Si alloys and alloy-heat treatment combinations. (*Designations from Table 4.3, P54*)

5. The investigations regarding the high pressure die casting process

The resultant energy-displacement diagram, in *Figure 5.10*, was also compared to its counterpart in *Figure 5.8*. This comparison confirmed the validity of the simulation tool, as it provided accurate estimations of the force-displacements curves.

As a result of the above conclusion, another simulation was similarly conducted to predict the bending test outcomes of the Al-Si alloys and alloy-heat treatment combinations at the plate thickness of 3.1 mm. The findings from this simulation were then compared to the other alloys' real average test results.

The resultant force-displacement and energy-displacement graphs of all the HPDC alloys and alloy-heat treatment combinations that were used for plate casting are respectively represented in *Figure 5.11* and *Figure 5.12*.

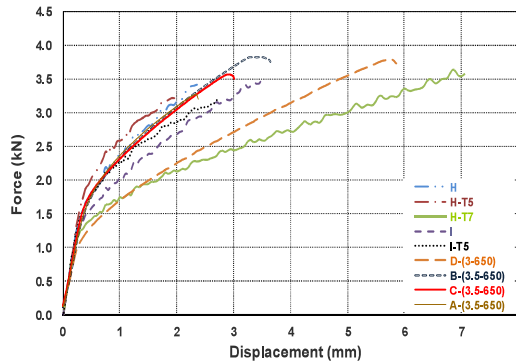


Figure 5.11: The force-displacement chart of all the HPDC alloys and alloy-heat treatment combinations that were used for the casting of the plates. (*Designations from Table 4.3, P54*)

A comparison between the Al-Si curves in *Figure 5.9* and *Figure 5.11* showed that larger forces are required to deform the thicker plates (3.1 mm) via the 3-point bending test. This finding is still valid, although it contradicts the outcome of *section 2.3.3*, which states that an increase in the wall thickness shall result in a deterioration to the mechanical properties. The reason for this contradiction can be linked to the nature of the 3-point bending test, which, unlike the tensile test, mainly affects the top and bottom layers of the tested plate and not its entire thickness.

5. The investigations regarding the high pressure die casting process

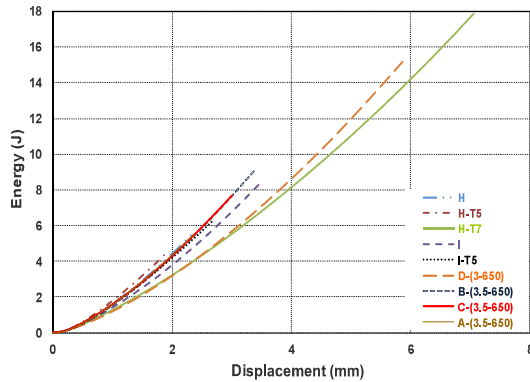


Figure 5.12: The energy-displacement chart of all the HPDC alloys and alloy-heat treatment combinations that were used for the casting of the plates. (*Designations from Table 4.3, P54*)

As shown in *Figure 5.12*, AlMg4Fe2 (D-(3-650)) and AlSi10MnMg-T7 were respectively the alloy and the alloy-heat treatment combination with the largest energy absorption capabilities. Unlike AlSi10MnMg-T7, AlMg4Fe2 offers the additional advantage of being able to withstand these large energy levels in the as-cast state, and without the need for an expensive heat treatment process.

The above outcome can be linked to the total elongation values of the different alloys and alloy-heat treatment combinations in *Figure 5.5*. This is because the highest average total elongation values were attained by AlMg4Fe2 (D-(3-650)) and AlSi10MnMg-T7, which enabled them to have the highest impacts on the crash resistance potentials of the castings.

Intermediate conclusions:

- The 3-point bending test simulations were able to predict the real crash resistance behaviours.
- The thickness of the plate was directly related to its crash resistance behaviour.
- The largest crash resistance behaviours were recorded for AlMg4Fe2 (D-(3-650)) and AlSi10MnMg-T7.
- Other alloys, such as AlSi7Mg0.3 (A-(3.5-650)), AlMg5Si2Mn (B-(3.5-650)) and AlMg6Si2MnZr (C-(3.5-650)) were not able to achieve high levels of energy absorption, and therefore are regarded to be less suitable for crash relevant parts, such as the 2020 Ford explorer shock tower .

5. The investigations regarding the high pressure die casting process

5.3.2 The impacts of the HPDC alloys on the crash resistance potentials of the parts from supplier 3

Like the alloys chosen for plate casting, it was also important to perform the crash resistance analysis using the alloys that were chosen for the HPDC trials at supplier 3. This approach made it possible to cover the whole range of alloys. In addition, it also gave an overview about the effect of the casting's geometry on the crash resistance behaviour.

The force-displacement and the energy-displacement charts of the alloys that were used for the casting of the parts at supplier 3 are respectively represented in *Figure 5.13* and *Figure 5.14* as follows.

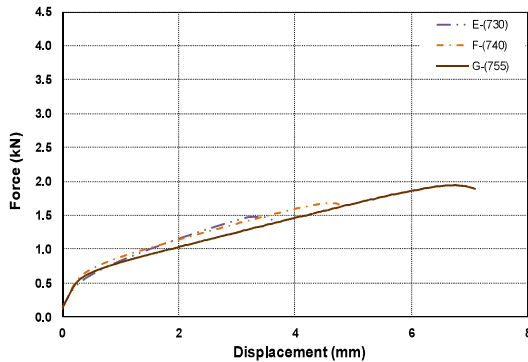


Figure 5.13: The force-displacement chart of the HPDC alloys that were used at supplier 3. (Designations from *Table 4.9, P65*)

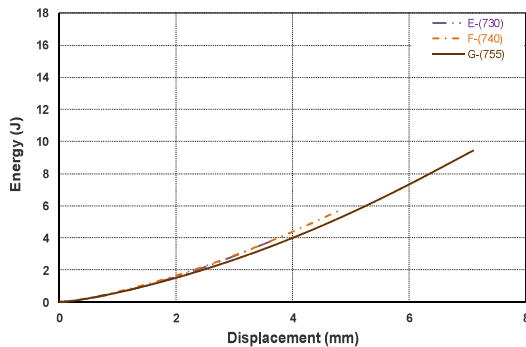


Figure 5.14: The energy-displacement chart of the HPDC alloys that were used at supplier 3. (Designations from *Table 4.9, P65*)

5. The investigations regarding the high pressure die casting process

Similar to the approach in the previous section, the force-displacement curves in *Figure 5.13* were retrieved from 3-point bending tests, which were conducted using 2 mm thick bending test samples. However, each energy-displacement curve in *Figure 5.14* was derived by calculating the area under its respective alloy's force-displacement curve.

Figure 5.14 illustrates that MYFORD (G-(755)) had the highest crash resistance behaviour in comparison to AlMg4Fe2 (F-(740)) and EN AB-42000 (E-(730)). This outcome can be linked to the total elongation values of the different alloys in *Figure 5.6*. This is because the highest average total elongation value was attained by the MYFORD alloy (G-(755)), which enabled it to have the highest impact on the crash resistance potential of the casting.

Intermediate conclusions:

- The implementation of the MYFORD alloy resulted in a better crash resistance potential than the AlMg4Fe2 alloy.
- After analyzing *Figure 5.12* and *Figure 5.14*, it was concluded that, among all alloys and alloy-heat treatment combinations that were used for the HPDC of the plates and the parts, MYFORD and AlSi10MnMg-T7 led to the best crash resistance potentials.

5.4 The rivetability of the HPDC alloys and alloy-heat treatment combinations

The outcomes of the SPR trials for the different HPDC alloys and alloy-heat treatment combinations are demonstrated in this section. The main purposes of these trials, which were performed according to the experimental approach in *section 4.5.4*, are represented in *Table 5.10*, and their findings are illustrated in *sections 5.4.1* and *5.4.2*.

Table 5.10: The test sequence for determining the rivetability of the HPDC alloys and alloy-heat treatment combinations.

Purpose of the investigation	Set of parameters (Designation) from <i>Table 4.3</i> or <i>Table 4.9</i>	Tests	Total number of joints/samples for each test method
a) To determine the suitability of joining each of the HPDC plates from supplier 1 and supplier 2 to a 1.3 mm DP steel sheet using a 36MnB4 rivet	H	• SPR	<ul style="list-style-type: none"> • SPR: 3 joints for each rivet-die combination • Lap shear: 3 samples using the best rivet-die combination
	H-T5		
	H-T7	• Lap shear test	
	I		
	I-T5		
	A-(2.5-650)		
	B-(2.5-650)		
	C-(2.5-650)		
	D-(3-350)		

5. The investigations regarding the high pressure die casting process

Table 5.10 (continued.)













b) To compare between the rivetability of MYFORD, EN AB-42000 and AlMg4Fe2	E-(730)		
	F-(740)		
	G-(755)		

As shown in *Table 5.10*, all the investigated supplier 1 plates and supplier 3 parts were produced using the optimum process parameters in *section 5.1*.

5.4.1 The rivetability of the HPDC alloys and alloy-heat treatment combinations that were utilized at the suppliers 1 and 2

























The rivet-die combinations in *Table 4.10* were used for the production of the joints between the cast aluminium plates and the DP steel sheets. The outer surfaces of these joints, which are represented in *Table 5.11*, were then evaluated to check if they were acceptable (✓), unacceptable (x) or borderline (o).

Table 5.11: The evaluation of the SPR joints on the plates from supplier 1 and 2.

Set of parameters (Designation) from <i>Table 4.3</i>	Rivet-die combination from <i>Table 4.11</i>			
	1 st combination BG0542EHL0-EHG13209	2 nd combination BG0542EHL0-EHG13210	3 rd combination BG0542EHL0-EHG14034	4 th combination BG0E44EHL0-EHG14033
H	X 	X 	X 	X 
H-T5	X 	X 	X 	O 
H-T7	X 	✓ 	✓ 	✓ 

5. The investigations regarding the high pressure die casting process

Table 5.11(continued.)

I	X 	X 	O 	√ 
I-T5	X 	X 	O 	√ 
A-(2.5-650)	X 	X 	X 	O 
B-(2.5-650)	X 	X 	O 	√ 
C-(2.5-650)	X 	X 	X 	X 
D-(3-650)	X 	√ 	√ 	√ 

The evaluation criteria of the joints in *Table 5.11* was based on checking if they consisted of radial and circumferential cracks, as in *Figure 4.36*, or not.

5. The investigations regarding the high pressure die casting process

Crack free joints were acceptable (✓). However, if they consisted of circumferential cracks, deep and long radial cracks or a combination of radial and circumferential cracks then they were regarded to be unacceptable (x). The joints were considered borderline (o) if they consisted of light radial cracks that did not extend towards the center of the joints.

By analyzing *Table 5.11*, the different HPDC alloys and alloy-heat treatment combinations could be divided into the following three groups based on their joining performances:

- The alloys and alloy-heat treatment combinations that did not have a single acceptable joint, such as AlSi10MnMg (H), AlSi10MnMg-T5 (H-T5), AlSi7Mg0.3 (A-(2.5-650)) and AlMg6Si2MnZr (C-(2.5-650)).
- The alloys and alloy-heat treatment combinations that had a single acceptable joint, such as AlSi7MnMg (I), AlSi7MnMg-T5 (I-T5) and AlMg5Si2Mn (B-(2.5-650)).
- The alloys and alloy-heat treatment combinations that had three or more acceptable joints, such as AlMg4Fe2 (D-(3-650)) and AlSi10MnMg-T7 (H-T7).

The different HPDC alloys and alloy-heat treatment combinations that belonged to the groups (b) and (c) were then used to produce the lap shear test samples. As mentioned earlier in *section 4.5.4*, these samples, three in this case, were produced for each of the considered HPDC alloys and alloy-heat treatment combinations using their best rivet-die combination. The results of this test gave an overview about the strength of the joints and their energy absorption capabilities.

The results of AlMg5Si2Mn (B-(2.5-650)) are not shown in *Figure 5.15*, as it was not possible to produce lap shear test sample for this alloy.

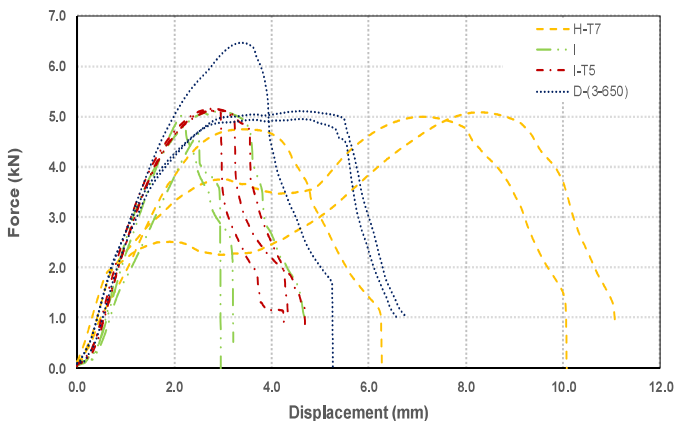


Figure 5.15: The force-displacement chart for the HPDC alloys and alloy-heat treatment combinations that belonged to the groups (b) and (c). (*Designations from Table 4.3, P54*)

5. The investigations regarding the high pressure die casting process

As seen in *Figure 5.15*, all the joints were able to withstand a maximum shear force value of at least 5 kN. However, there was a difference in their energy absorption capabilities. This energy absorption, which resembles the area under the respective force-displacement curve, was the highest for AlSi7MnMg-T7 (H-T7). The second highest energy absorption was recorded by AlMg4Fe2 (D-(3-650)), which unlike the rest of the alloys and alloy-heat treatment combinations in *Figure 5.15*, was casted into the thicker supplier 1 plates. The remaining alloy and alloy-heat treatment combination, AlSi7MnMg (I) and AlSi7MnMg-T5 (I-T5), showed the least energy absorption capabilities.

The above outcomes can be linked to the total elongation values of the different alloys and alloy-heat treatment combinations in *Figure 5.5*. This is because the ones with the higher average total elongation values (AlSi10MnMg-T7, AlMg4Fe2 (D-(3-650))) were the ones with the better rivetability and energy absorption capabilities than the rest of the considered alloys and alloy-heat treatment combinations, such as AlSi7MnMg (I) and AlSi7MnMg-T5 (I-T5).

Intermediate conclusion:

- AlSi10MnMg (H), AlSi10MnMg-T5 (H-T5), AlSi7Mg0.3 (A-(2.5-650)) and AlMg6Si2MnZr (C-(2.5-650)) are not suitable for SPR joining as they could not be riveted by any of the chosen rivet-die combinations.
- AlSi7MnMg (I), AlSi7MnMg-T5 (I-T5) and AlMg5Si2Mn (B-(2.5-650)), have a better rivetability than the combinations in the first group (a). However, they are highly dependent on the chosen rivet-die combination, as an acceptable joint by the SPR joining method was only made possible when a shallow die (EHG14033) and a short rivet (BG0E44EHL0) were used.
- Among the investigated HPDC alloys and alloy-heat treatment combinations in this section, AlSi10MnMg-T7 (H-T7) and AlMg4Fe2-F (D-(3-650)) are considered to have the best rivetability, and thus the highest suitability to the SPR joining method. These conclusions can be linked to their ability to withstand the higher forming limits of the deeper dies without developing cracks on their outer joints' surfaces. In addition to the ability of their SPR joints, in particular those belonging to AlSi10MnMg-T7, to withstand higher energy absorptions before fracture.
- Although the plates from supplier 1 and supplier 2 had different thicknesses, their force-displacement curves, in *Figure 5.15*, could be still compared together. This is because the reduction in the SPR joint strength is counteracted by the lower susceptibility of the thinner bottom plates to develop cracks (94) (90).











5. The investigations regarding the high pressure die casting process

5.4.2 The rivetability of the HPDC alloys that were utilized at supplier 3

By using the parts produced at supplier 3, it was possible to conduct SPR trials for the sake of comparing between the rivetability of MYFORD (G-(755)), EN AB-42000 (E-(730)), which is the standard alloy at supplier 3, and AlMg4Fe2 (F-(740)).

From the analysis of *Table 5.11*, it was clear that the joint with the highest susceptibility to crack formation was the one made using the 1st rivet-die combination. Therefore, it made sense to start this section by using the 2nd rivet-die combination. If the joint from this combination was accepted, then additional joints were made using the 1st rivet-die combination. If not, then only joints using the 3rd and 4th rivet die combinations were made.

Table 5.12: The evaluation of the SPR joints on the parts from supplier 3.

Set of parameters (Designation) from <i>Table 4.9</i>	Rivet-die combination from <i>Table 4.11</i>			
	1 st combination BG0542EHL0-EHG13209	2 nd combination BG0542EHL0-EHG13210	3 rd combination BG0542EHL0-EHG14034	4 th combination BG0E44EHL0-EHG14033
E-(730)	X	X 	X 	O 
F-(740)	X	X 	✓ 	✓ 
G-(755)	X 	✓ 	✓ 	✓ 

As seen in *Table 5.12*, more acceptable joints were obtained by G-(755) than by E-(730) or F-(740).

The outcomes in *Table 5.12* can be linked to the total elongation values of the different alloys in *Figure 5.6*. This is because the alloy with the highest average total elongation value (G-(755))

5. The investigations regarding the high pressure die casting process

was the one with the best rivetability. In addition, the other alloys with lower average total elongation values (E-(730) & (F-(740)) had accordingly worse rivetability.

Intermediate conclusion:

- Based on the outcomes of the SPR joining trials that were conducted on the HPDC parts from supplier 3, the MYFORD alloy (G-(755)) is regarded to have a better rivetability, and thus a better suitability to the SPR joining method than the AlMg4Fe2 alloy. This conclusion is based on the fact that unlike the AlMg4Fe2 alloy (F-(740)), it was possible to produce an acceptable joint for this alloy using the deeper die of the second rivet-die combination (BG0542EHL0- EHG13210).

6. The investigations regarding the RheoMetal™ process

6 The investigations regarding the RheoMetal™ process

As a result of the probable positive impact of the RheoMetal™ process on the overall cost reduction, as illustrated in *section 3.2*, and its numerous advantages, it was important to investigate the possibility of implementing this casting technology instead of HPDC for the mass production of thin walled structural aluminium body castings.

For the above reason and similar to the approach in *chapter 5*, plates and parts that satisfied the thickness and/or the dimensional requirements of the 2020 Ford explorer shock tower were casted by the RheoMetal™ process, to serve as a source of the test samples.

Prior to the RheoMetal™ trials, it was important to determine the optimum process parameters, which could facilitate the retrieval of the best possible outcomes from the seven investigated alloys at supplier 1 and supplier 3, by testing their impacts on the mechanical properties and the quality of the supplier 1 plates and the supplier 3 parts. These parameters did not only include the melt flow velocity and the intensification pressure, as in the case of HPDC, but also included other important factors such as the added EEM amount (%EEM), the rotation speed of the EEM and the melt superheat.

By extracting the microstructural and tensile test samples from the RheoMetal™ casted plates and parts and then respectively analyzing and testing them, it was possible to accurately check whether the investigated alloys could be suitable for the RheoMetal™ process and if they could reach the desired properties of the 2020 Ford explorer shock tower or not.

In addition, and as the 2020 Ford explorer shock tower is a crash relevant part, it was important to analyze the impact of each RheoMetal™ alloy on the crash resistance potential of the casting. These impacts on the crash resistance potential were retrieved by conducting 3-point bending tests on samples from the RheoMetal™ casted plates and parts.

Furthermore, and as the 2020 Ford explorer shock tower is joined to the car body structure, most importantly to DP steel sheets, by the SPR joining method, it was necessary to analyze the responses of the different RheoMetal™ alloys to this joining mechanism by visually evaluating the outer surfaces of four different SPR joints between the respective SPR samples and 1.3 mm DP steel sheets.

Each of the above steps is described in a separate section as follows.

6. The investigations regarding the RheoMetal™ process

6.1 The optimum RheoMetal™ process parameters

As mentioned earlier, in addition to the process parameters such the melt flow velocity, especially during the 2nd phase (die filling), and the intensification pressure, there are additional parameters that affect the outcome of the RheoMetal™ casting process such as the added EEM amount (%EEM), the rotation speed of the EEM and the melt superheat. Deriving the optimum values of all of these process parameters was therefore an important step towards the production of high-quality castings.

Most of the optimum process parameters that were required to produce the supplier 1 plates were derived after analyzing the outcomes of the pre-trials. However, no pre-trials were performed at supplier 3 to determine the respective optimum process parameters. This is because the supplier 3's cast parts were produced using the process parameters' values that were either based on information from the literature and on the supplier's recommendations, such as the melt flow velocity and the intensification pressure, or were recommended by the company *RheoMetal AB*, such as the %EEM, the rotation speed of the EEM and the melt superheat.

Similar to *section 5.1*, the melt flow velocity in the shot sleeve (1st phase) was not investigated. For the RheoMetal™ trials at supplier 1 and 3, a low piston velocity in the range of 0.15-0.223 m/s was assigned to this phase.

6.1.1 The optimum RheoMetal™ process parameters to produce the plates at supplier 1

For the production of the plates at supplier 1, the optimum value of the melt flow velocity in the 2nd phase (die filling) was defined based on information from the literature. On the other hand, the optimum values of the other process parameters, the intensification pressure, the melt superheat, the %EEM and the rotation speed of the EEM, were derived after conducting a number of investigations and tests according to the test sequence in *Table 6.1*.

Table 6.1: The test sequence for the determination of the optimum RheoMetal™ process parameters at supplier 1.

Purpose of the investigation	Set of parameters (Designation) from <i>Table 4.5</i>	Test methods	Sample form & orientation relative to the flow direction	Total number of tested samples for each designation*
(a) Determining the optimum value of the intensification pressure	D-(50-4.63-300-1000)-R	•Tensile test	Tensile test:	Tt: 3 S from 1 P Dm:5 P
	D-(50-4.63-500-1000)-R	•Density measurement	•Type E •Perpendicular	

6. The investigations regarding the RheoMetal™ process

Table 6.1 (continued.)

(b) Determining the optimum value of the melt superheat	C-(40-4.63-575-1000)-R	•Microst- ructural analysis	-	Ma: 1 S (position a) Dm: 4 P	
	C-(50-4.63-575-1000)-R			Ma: 1 S (position a) Dm: 10 P	
(c) Determining the optimum %EEM	B-(30-2.49-575-1000)-R			Ma: 1 S (position a) Dm: 5 P	
	B-(30-4.63-575-1000)-R			Ma: 1 S (position a) Dm: 10 P	
(d) Determining the optimum value of the rotation speed of the EEM	A-(50-4.63-575-1000)-R			•Density measure- ment	Ma: 1 S (position a) Dm: 10 P
	A-(50-4.63-575-3000)-R				Ma: 1 S (position a) Dm: 5 P

* **Tt:** Tensile test, **Dm:** Density measurement, **Ma:** Microstructural analysis, **S:** Sample(s), **P:** Plate(s), **Pa:** Part (s).

6.1.1.1 The optimum melt flow velocity

As mentioned earlier in section 2.4.3.2, the choice of the melt flow velocity for the RheoMetal™ process is highly dependent on the gate's thickness. Therefore, by using the gate thickness in Table 4.4, it was possible to linearly interpolate the maximum gate velocity for this gate design from Table 2.4. This velocity, which had a magnitude of 6.339 m/s, was then transformed, with the equations in section 2.4.3.2, into a piston velocity of 1.26 m/s (piston diameter = 60 mm).

Intermediate conclusion:

- The piston velocity of 1.26 m/s during the second phase of die filling was considered suitable for the production of the plates at supplier 1 by the RheoMetal™ casting process.

6.1.1.2 The optimum intensification pressure

By analyzing the influence of the intensification pressure on the mechanical properties of the AlMg4Fe2 alloy and the porosity levels of its casted plates, it was possible to obtain the optimum intensification pressure value for the RheoMetal™ trials at supplier 1

6. The investigations regarding the RheoMetal™ process

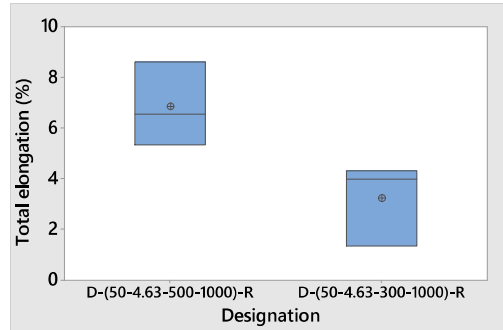


Figure 6.1: The influence of the intensification pressure on the total elongation (%) of the AlMg4Fe2 alloy. (Designations from Table 4.5, P58)

Table 6.2: The porosity levels at different intensification pressures for the AlMg4Fe2 alloy.

Alloy	Set of parameters (Designation) from Table 4.5	Ideal density (g/cm ³)	Average measured density (g/cm ³)	Porosity (%)
AlMg4Fe2	D-(50-4.63-300-1000)-R	2.67	2.635	1.311
	D-(50-4.63-500-1000)-R		2.643	1.011

The measured densities in Table 6.2, as well as in Table 6.4, Table 6.6 and Table 6.8 are the average of their corresponding plates' measured densities, which were in turn derived based on the approach in section 4.5.3. The porosity levels were calculated using equation (4.4), in which the ideal densities (ρ_0) were obtained from the alloys' supplier manual (2).

As seen in Figure 6.1 and Table 6.2, increasing the intensification pressure from 300 bar to 500 bar has led to an increase in the average total elongation value by approximately 4 % and a decrease in the overall porosity level by approximately 0.3 %.

Due to the above outcomes, it was decided to use the highest possible intensification pressure value for the RheoMetal™ casting trials at supplier 1. This value, which had a magnitude of 575 bar, was considered to be suitable for the gate design in Figure 4.10.

Intermediate conclusions:

- Increasing the intensification pressure has caused an enhancement in the mechanical properties by reducing the porosity level in the castings.
- As shown in Table 4.5, an optimum intensification pressure of 575 bar was defined for the RheoMetal™ casting trials at supplier 1.
- Due to the larger gate design, this chosen pressure value was lower than the outcome of section 5.1.1.2.




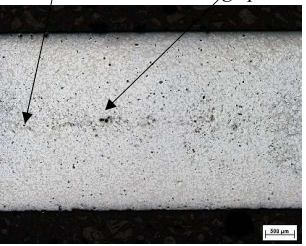
6. The investigations regarding the RheoMetal™ process

6.1.1.3 The optimum melt superheat

As discussed earlier in *section 2.4.3.3*, varying the melt superheat can affect the mechanical properties of the casting by influencing the size of the primary globular α_1 -Al phase (α_1 -Al phase), which forms during the slurry making step, and the solid fraction. Therefore, determining an optimum value for this factor was an important prerequisite for the RheoMetal™ casting trials at supplier 1.

The optimum melt superheat was determined after comparing between the microstructures from two different plates. These plates were produced using the AlMg6Si2MnZr alloy at different melt superheats.

Table 6.3: The influence of the melt superheat on the microstructures of the RheoMetal™ plates from supplier 1.

Magnification	Set of parameters (Designation) from Table 4.5	
	C-(50-4.63-575-1000)-R	C-(40-4.63-575-1000)-R
100x	 <p><i>α_1-Al phase</i></p>	 <p><i>α_1-Al phase</i></p>
25x	 <p><i>Shrinkage porosity</i></p>	 <p><i>Macrosegregation Shrinkage porosity</i></p>

As shown in *Table 6.3*, a comparison between the microstructural images of C-(40-4.63-575-1000)-R, which was produced at a superheat of 40°C, and C-(50-4.63-575-1000)-R, which was produced at a superheat of 50°C, was done.

6. The investigations regarding the RheoMetal™ process

According to *Figure 2.23(a)*, increasing the melt superheat is expected to cause a reduction in the size of the α_1 -Al phase. However, as this size reduction is not large, it could not be visually detected from the 100x microstructural images in *Table 6.3*.

On the other hand, the visual analysis of the 25x images in *Table 6.3* show that C-(40-4.63-575-1000)-R had a higher solid fraction (fraction of the α_1 -Al phase) and a higher porosity level than C-(50-4.63-575-1000)-R. This observation can be also correlated to:

- *Figure 2.23(b)*, which shows that an increase in the superheat can cause a reduction in the solid fraction.
- The porosity levels in *Table 6.4*

Table 6.4: The porosity levels at different melt superheats for the AlMg6Si2MnZr alloy.

Alloy	Set of parameters (Designation) from <i>Table 4.5</i>	Ideal density (g/cm ³)	Average measured density (g/cm ³)	Porosity (%)
AlMg6Si2MnZr	C-(40-4.63-575-1000)-R	2.64	2.562	3.044
	C-(50-4.63-575-1000)-R		2.575	2.524

As shown in *Table 6.4*, an increase in the superheat by 10 °C was responsible for reducing the overall porosity level by 0.493 %.

Intermediate conclusions:

- Changing the melt superheat had no visually detectable impact on the size of the α_1 -Al phase.
- The melt superheat was inversely proportional to the solid fraction and the porosity level.
- The lower melt superheats led to an increase in the solid fraction to a level higher than that required for a laminar flow. This unrequired increase in the solid fraction caused a reduction in the feeding efficiency of the semi-solid slurry close to the gate and was probably the reason beyond the detected microstructural defects in *Table 6.3*.
- Higher melt superheat was expected to cause an improvement in the mechanical properties of the plates, due to the better feeding of the slurry and the lower porosity levels of the plates. Therefore, an optimum melt superheat of 50 °C was defined for most of the RheoMetal™ casting trials at supplier 1.

6.1.1.4 The optimum %EEM

Like the melt superheat, the added EEM amount (%EEM) can have an impact on the mechanical properties by causing a change in the α_1 -Al phase's size and in the solid fraction.

In order to determine the optimum %EEM, RheoMetal™ casting trials using two different sizes of the EEM were conducted and the outcomes of these trials were analyzed.

6. The investigations regarding the RheoMetal™ process

The investigated %EEMs were:

- A 3.5%EEM (%EEM = 3.5% of the mass of the shot).
- A 6.5%EEM (%EEM = 6.5% of the mass of the shot).

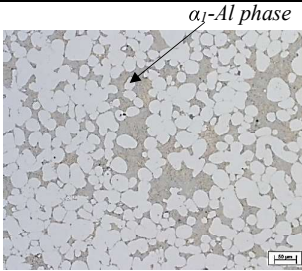
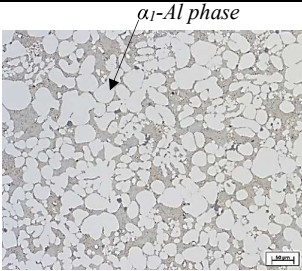

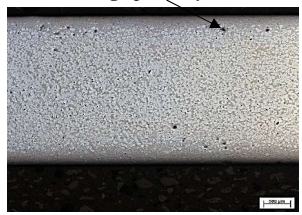
The exact heights of the investigated EEMs (h_{EEM}) were calculated using *equation (4.3)* in *section 4.3*. The inputs to this equation were the mass of the shot from *Table 4.5*, the %EEM, the density of the AlMg5Si2Mn alloy from the supplier manual (2), the 2 cm EEM's radius (R) and the 0.64 cm rod's radius (r).

The resultant h_{EEM} for each %EEM were:

- h_{EEM} for 3.5%EEM = 2.49 cm
- h_{EEM} for 6.5%EEM = 4.63 cm

The microstructures from the plates, which were produced using the above h_{EEM} , and their porosity levels are represented in *Table 6.5* and *Table 6.6* as follows.

Table 6.5: The influence of the %EEM on the microstructures of the RheoMetal™ plates from supplier 1.

Magnification	Set of parameters (Designation) from <i>Table 4.5</i>	
	B-(30-4.63-575-1000)-R	B-(30-2.49-575-1000)-R
200x	 <p><i>α_1-Al phase</i></p>	 <p><i>α_1-Al phase</i></p>
25x		 <p><i>Shrinkage porosity</i></p>

6. The investigations regarding the RheoMetal™ process

Table 6.6: The porosity levels at different melt superheats for the AlMg6Si2MnZr alloy.

Alloy	Set of parameters (Designation) from Table 4.5	Ideal density (g/cm ³)	Average measured density (g/cm ³)	Porosity (%)
AlMg6Si2MnZr	B-(30-4.63-575-1000)-R	2.63	2.632	0
	B-(30-2.49-575-1000)-R		2.621	0.343

By visually analysing the images in Table 6.5 and as seen in Table 6.6, increasing the %EEM from 3.5% to 6.5% was responsible for decreasing the α_1 -Al phase's size, increasing the solid fraction and decreasing the overall porosity level by 0.342%.

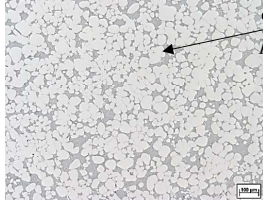
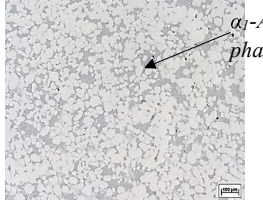
Intermediate conclusions:

- Increasing the %EEM led to a reduction in the size of the α_1 -Al phase. This can be contributed to the increase in the nucleation sites during the contact between the EEM and the liquid melt.
- Increasing the %EEM has caused a reduction in the porosity level. This outcome can be probably due to the increase in the solid fraction of the slurry to the limit that is required for a laminar flow.
- From the above findings, it was concluded that the use of a larger %EEM would result in an improvement in the mechanical properties of the plates. Therefore, an optimum %EEM of 6.5% was defined for most of the RheoMetal™ casting trials at supplier 1.

6.1.1.5 The optimum rotation speed of the EEM

Similar to the melt superheat and the %EEM, the rotation speed of the EEM during the slurry making process can have an impact on the mechanical properties of the plates. Therefore, it was important to determine the optimum EEM's rotation speed for the RheoMetal™ casting trials at supplier 1. This was done, as seen in Table 6.7 and Table 6.16, by testing the impacts of using two different rotation speed ranges on the microstructures and the porosity levels of the plates.

Table 6.7: The influence of the rotation speed of the EEM on the microstructures of the RheoMetal™ plates from supplier 1.

Magnification	Set of parameters (Designation) from Table 4.5	
	A-(50-4.63-575-1000)-R	A-(50-4.63-575-3000)-R
100x		

6. The investigations regarding the RheoMetal™ process

Table 6.7 (continued.)



Although, according to the literature review in *section 2.4.3.3*, a decrease in the α_1 -Al's grain size is usually expected at a higher EEM's rotation speed, no visually detectable difference in the α_1 -Al phase's size could be traced by visually inspecting the 100x images in *Table 6.7*.

Table 6.8: The porosity levels at different rotation speeds of the EEMs for the AlSi7Mg0.3 alloy.

Alloy	Set of parameters (Designation) from <i>Table 4.5</i>	Ideal density (g/cm ³)	Average measured density (g/cm ³)	Porosity (%)
AlSi7Mg0.3	A-(50-4.63-575-1000)-R	2.66	2.646	0.529
	A-(50-4.63-575-3000)-R		2.627	1.256

By visually evaluating the 25x images in *Table 6.7* and the porosity levels in *Table 6.8*, it is obvious that the rotation speed of the EEM and the porosity level of the plate are inversely proportional to each other.

Intermediate conclusion:

- Changing the rotation speed of the EEM had no visually detectable impact on the size of α_1 -Al phase.
- Increasing the EEM's rotation speed has caused an increase in the porosity level and a decrease in the feeding efficiency of the semi-solid slurry close to the gate. This finding can be correlated to the increase in the fraction of the α_1 -Al phase (solid fraction) at the higher EEM's rotation speed to a value beyond that required for a laminar flow.
- From the above findings, it was concluded that the use of a lower EEM's rotation speed would result in an improvement in the mechanical properties and the quality of the plates. For this reason, 0-1000 rpm was considered to be the optimum EEM's rotation speed for the RheoMetal™ casting trials at supplier 1.

6. The investigations regarding the RheoMetal™ process

6.1.2 The optimum RheoMetal™ process parameters to produce the parts at supplier 3

As mentioned earlier and similar to the approach in *section 6.1.1*, the optimum values of the melt flow velocity and the intensification pressure were defined based on information from the literature and on the supplier's recommendations. These values, illustrated in *sections 6.1.2.1* and *6.1.2.2*, were used in the production of the parts by the RheoMetal™ process at supplier 3.

However, for the RheoMetal™ trials at supplier 3, the implemented values of the %EEM, the rotation speed of the EEM and the melt superheat were based entirely on external recommendations from the company *RheoMetal AB*.

6.1.2.1 The optimum melt flow velocity

According to Table 2.4, the maximum gate velocity during die filling for a 9 mm thick gate should be approximately equal to 3.25 m/s. However, due to the large size of the part and for the sake of speeding up the casting process, it was advised by the supplier (Comptech AB) to increase the gate velocity to a value of 14.014 m/s. This value was then transformed to a piston velocity of 2.86 m/s with the help of the equations in section 2.4.3.2. The inputs to these equations were the gate dimensions in Table 4.6 and the piston area (diameter =100 mm).

Intermediate conclusion:

- A second phase's piston velocity of 2.86 m/s was considered suitable for the production of the parts at supplier 3 by the RheoMetal™ casting process.

6.1.2.2 The optimum intensification pressure

The gate design in *Figure 4.10* was used at supplier 3 for the HPDC trials and the RheoMetal™ casting trials. For this reason, it was concluded that the same intensification pressure value could be considered suitable for both casting processes.

Intermediate conclusion:

- The intensification pressure value of 340 bar was also considered to be suitable to the RheoMetal™ casting trials at supplier 3.

6.2 Characterization of the different RheoMetal™ alloys

Similar to the characterization criteria of the HPDC alloys in *section 5.2* and as stated at the beginning of *chapter 6*, the assessment of the different RheoMetal™ alloys' microstructures and the comparison between their mechanical testing outcomes were regarded as vital steps toward achieving the main aim of this thesis.

6. The investigations regarding the RheoMetal™ process

As seen from the designations in Table 6.9, the evaluated plates from supplier 1 were made from different as-cast alloys using the optimum process parameters in section 6.1.1. On the other hand, and as mentioned earlier, the evaluated parts from supplier 3 were produced from three different as-cast alloys using the process parameters' values that were either based on information from the literature and on the supplier's recommendations, such as the melt flow velocity and the intensification pressure, or were provided by the company *RheoMetal AB*, such as the %EEM, the rotation speed of the EEM and the melt superheat.

Table 6.9: The test sequence for the comparison between the different RheoMetal™ alloys.

Purpose of the investigation	Set of parameters (Designation) from Table 4.5 or Table 4.9	Test method	Sample form & orientation relative to the flow direction	Total number of tested samples for each designation*
(a) To provide an accurate characterization of the RheoMetal™ alloys that were used for the casting of the plates at supplier 1	A-(50-4.63-575-1000)-R	•Tensile test	Tensile test: •Type E •Perpendicular	Tt: 4 S from 2 P Ma: 1 S
	B-(30-4.63-575-1000)-R			Tt: 6 S from 2 P Ma: 1 S
	C-(50-4.63-575-1000)-R			Tt: 2 S from 1 P Ma: 1 S
	D-(50-4.63-575-1000)-R			Tt: 2 S from 1 P Ma: 1 S
(b) To provide an accurate characterization of the RheoMetal™ alloys that were used for the casting of the parts at supplier 3	E-(730-30-1100)-R	•Microstructural analysis	Tensile test: •Mini samples •Longitudinal	Tt: 6 S from 1 P Ma: 1 S
	F-(750-30-1100)-R			
	G-(755-30-1100)-R			

* **Tt:** Tensile test, **Ma:** Microstructural analysis, S: Sample(s), P: Plate(s), Pa: Part (s).

6.2.1 Characterization of the RheoMetal™ alloys that were used at supplier 1

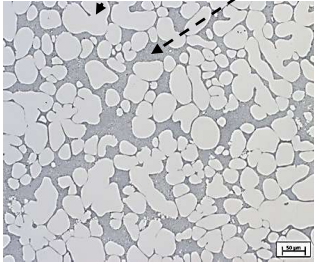

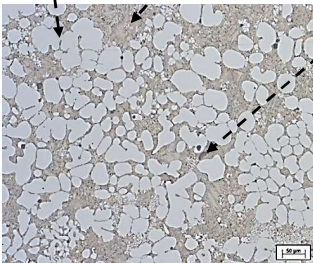

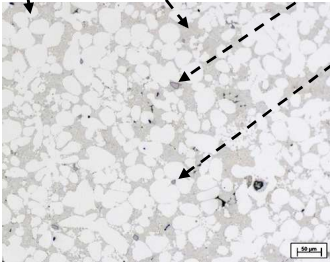

The microstructural investigation and the mechanical properties of the RheoMetal™ alloys that were used at supplier 1 are represented in *section 6.2.1.1* and *section 6.2.1.2* as follows.

6.2.1.1 Microstructural investigation of the RheoMetal™ alloys that were used at supplier 1

The microstructural investigation was conducted in a similar manner to that mentioned in section 5.2.1.1. A representation of the different microstructural images for each designation, from *Table 4.5*, is shown in *Table 6.10* as follows.

6. The investigations regarding the RheoMetal™ process

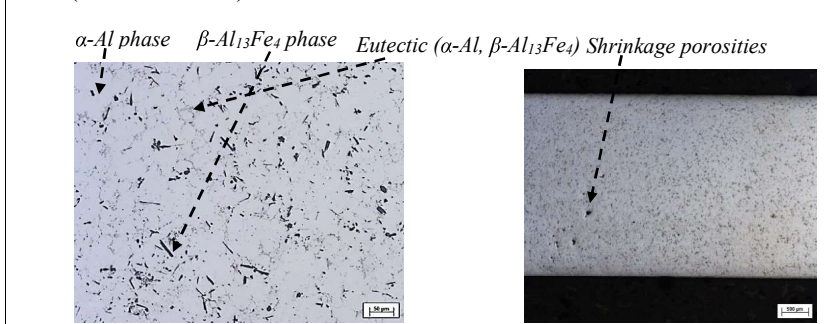
Table 6.10: The 200x and 25x microstructural images of the RheoMetal™ alloys that were used at supplier 1. (Designations from Table 4.5, P58)

Magnification	
200x	25x
<ul style="list-style-type: none"> A-(50-4.63-575-1000)-R  <p>α-Al phase Eutectic (α-Al, Si)</p> 	
<ul style="list-style-type: none"> B-(30-4.63-575-1000)-R  <p>α-Al phase Eutectic (α-Al, Mg₂Si) α-AlMnSiFe phase</p> 	
<ul style="list-style-type: none"> C-(50-4.63-575-1000)-R  <p>α-Al phase Eutectic (α-Al, Mg₂Si) Mg-rich phase α-AlMnSiFe phase</p> 	 <p>Shrinkage porosities</p>

6. The investigations regarding the RheoMetal™ process

Table 6.14 (continued.)

• D-(50-4.63-575-1000)-R



The analysis of the 200x microstructural images in *Table 6.10* shows that each of the investigated microstructures in this section consists of a primary α -Al phase, with a globular morphology, a eutectic and, even if not illustrated, at least a single intermetallic phase.

Intermediate conclusion:

- Unlike the dendritic morphology and the large size of the primary α -Al phase in each of the HPDC microstructures in *Table 5.7*, the RheoMetal™ microstructures of the same alloys in *Table 6.10* are characterized by having smaller and globular primary α -Al phase morphologies, which, as mentioned earlier in *section 2.4*, cause the thixotropic behaviour of the slurry by decreasing the restriction to the flow of the liquid phase under the application of a shear force.
- The presence of the shrinkage porosities in the microstructures of AlMg4Fe2 (D50-575) and AlMg6Si2MnZr (C-(50-4.63-575-1000)-R) can be due to the inefficient feeding of their semi-solid slurries into the die.
- Regardless of the shrinkage porosities, no additional defects were detected by visually analysing the microstructural images in *Table 6.10*. For this reason, it was basically concluded that the investigated alloy-process parameters combinations in this section were suitable for the production of the plates via the RheoMetal™ casting process.
- The above conclusion doesn't however negate the fact that there might still be other defects and precipitates in the nanometer range, which cannot be detected by the visual inspection of the microstructural images, and that can have a deteriorating influence on the mechanical properties of the castings. In addition, and as mentioned earlier in *section 2.4.3.4*, defects such as the transverse and longitudinal macrosegregations can be also present in different regions of the castings, as a result of the shear and the solidification behaviours of the slurry.

6. The investigations regarding the RheoMetal™ process

6.2.1.2 The mechanical properties of the RheoMetal™ alloys that were used at supplier 1

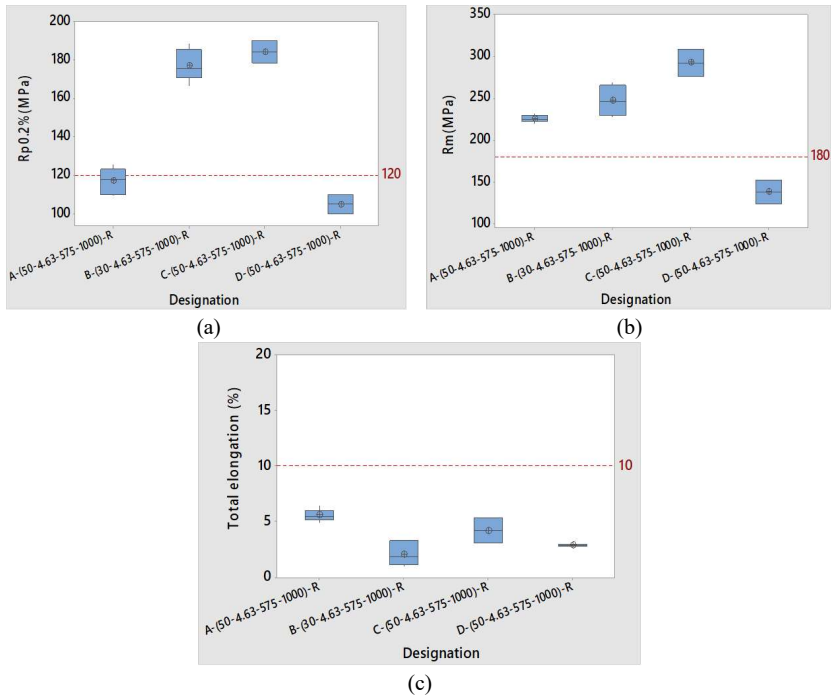


Figure 6.2: The comparison between the different RheoMetal™ alloys in terms of their (a) Rp0.2 values (MPa), (b) Rm values (MPa) and (c) total elongation values (%). (Designations from Table 4.5, P58)

Similar to the investigations in sections 5.2.1.2 and 5.2.2.2, the mechanical properties of the different RheoMetal™ alloys that were used at supplier 1 had to be studied and correlated to the requirements of the 2020 Ford explorer shock tower (values higher than those pointed out by the dashed lines in Figure 6.2).

As shown in Figure 6.2 (a), AlMg5Si2Mn (B-(30-4.63-575-1000)-R) and AlMg6Si2MnZr (C-(50-4.63-575-1000)-R) were the two alloys able to fulfill the Rp0.2 requirements of the shock tower. The Rm requirement, as seen in Figure 6.2 (b), was, however, not met by only the AlMg4Fe2 (D-(50-4.63-575-1000)-R) alloy. On the other hand and as seen in Figure 6.2 (c), not a single alloy was able to meet the Ford explorer's total elongation requirement of more than 10 %.

6. The investigations regarding the RheoMetal™ process

Intermediate conclusion:

- AlMg5Si2Mn (B-(30-4.63-575-1000)-R) and AlMg6Si2MnZr (C-(50-4.63-575-1000)-R) had better performances than the other investigated RheoMetal™ alloys, as they were both able to reach the yield strength and the ultimate tensile strength requirement of the 2020 Ford explorer shock tower.
- The inability of any alloy to fulfil the total elongation requirement of the shock tower can be linked to the inefficiency of the manual RheoMetal™ process at supplier 1.

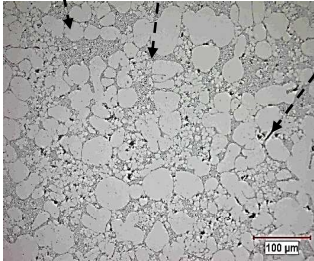

6.2.2 Characterization of the RheoMetal™ alloys that were used at supplier 3

The microstructural investigation and the mechanical properties of the RheoMetal™ alloys that were used at supplier 3 are represented in *section 6.2.1.1* and *section 6.2.1.2* as follows.

6.2.2.1 Microstructural investigation of the RheoMetal™ alloys that were used at supplier 3

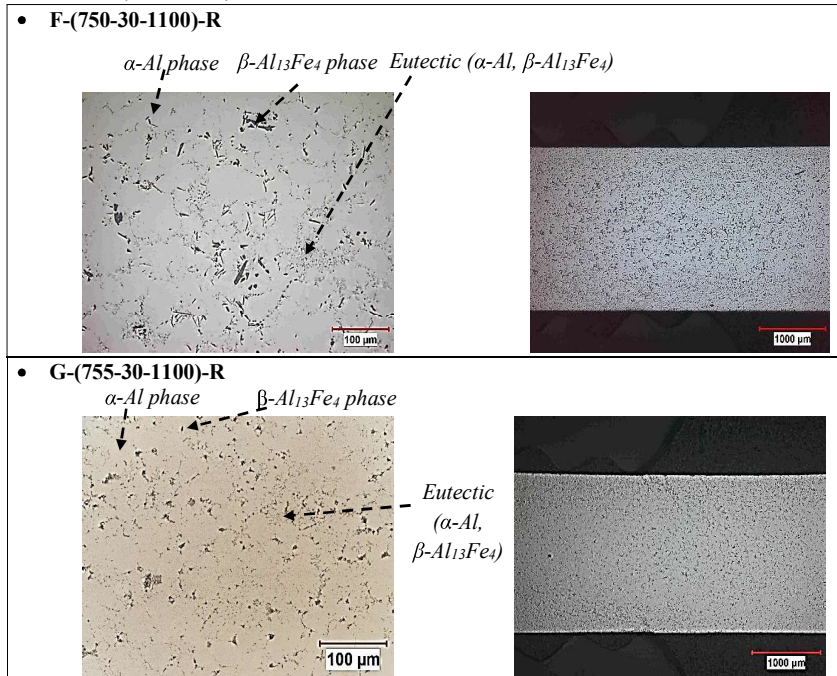
The microstructural investigation was conducted in a similar manner to that mentioned in *section 5.2.1.1*. A representation of the different microstructural images for each designation, from *Table 4.9*, is shown in *Table 6.11* as follows.

Table 6.11: The 200x and 25x microstructural images of the RheoMetal™ alloys that were used at supplier 3. (*Designations from Table 4.5, P58*)

Magnification	
200x	25x
<ul style="list-style-type: none"> • E-(730-30-1100)-R <div style="display: flex; justify-content: space-around; align-items: flex-start; padding: 10px;"> <div style="text-align: center;"> <p><i>α-Al phase</i> <i>Eutectic (α-Al, Si)</i></p>  </div> <div style="text-align: center;"> <p><i>Fe-rich intermetallic phase</i></p>  </div> </div> 	

6. The investigations regarding the RheoMetal™ process

Table 6.11 (continued.)



Each of the RheoMetal™ alloys' microstructures in *Table 6.11* consists of a primary α -Al phase, with a globular morphology, a eutectic and at least a single intermetallic phase. In the case of the EN AB-42000 alloy (E-(730-30-1100)-R), two α -Al phase morphologies could be visually detected at a 200x magnification (large globular primary α -Al phase that is surrounded by fine dendritic α -Al phase). However, in the case of the AlMg4Fe2 alloy (F-(750-30-1100)-R) and the MYFORD alloy (G-(755-30-1100)-R), only the globular α -Al phase morphology could be clearly detected by visually inspecting the 200x magnification images in *Table 6.11*.

From the 25x images, it is obvious that a higher fraction and a larger size of the globular α -Al phase were present at the middle of the cross sections of the supplier 3 parts.

Intermediate conclusion:

- The two α -Al phase morphologies in the microstructure of the EN AB-42000 alloy (E-(730-30-1100)-R) can be contributed to the slurry making process (large globular primary α -Al phase) and to the solidification of the slurry's liquid phase during the die casting step (fine dendritic α -Al phase) (45).

6. The investigations regarding the RheoMetal™ process

- The RheoMetal™ microstructures of the alloys in *Table 6.11* are characterized by having globular primary α -Al phase morphologies, which develop mainly during the slurry making process. These phase morphologies are smaller in size than their dendritic counterparts in the HPDC microstructures of the same alloys. This difference in the size and the morphology of the primary α -Al phase is what gives the slurry its thixotropic behaviour, as it facilitates the flow of the liquid phase under the application of a shear force.
- Due to the lack of defects in the 25x microstructural images, it can be basically concluded that the investigated alloy-process parameters combinations (EN AB-42000 (E-(730-30-1100)-R), AlMg4Fe2 (F-(750-30-1100)-R) and MYFORD (G-(755-30-1100)-R)) were suitable for the production of the parts via the RheoMetal™ casting process.
- The above conclusion does not exclude the probability that there can still be other defects in the nanometer range (e.g. precipitates) and/or in other regions of the castings (e.g. transverse or longitudinal macrosegregations) that can play a role in negatively impacting the resultant mechanical properties.

6.2.2.2 The mechanical properties of the RheoMetal™ alloys that were used at supplier 3

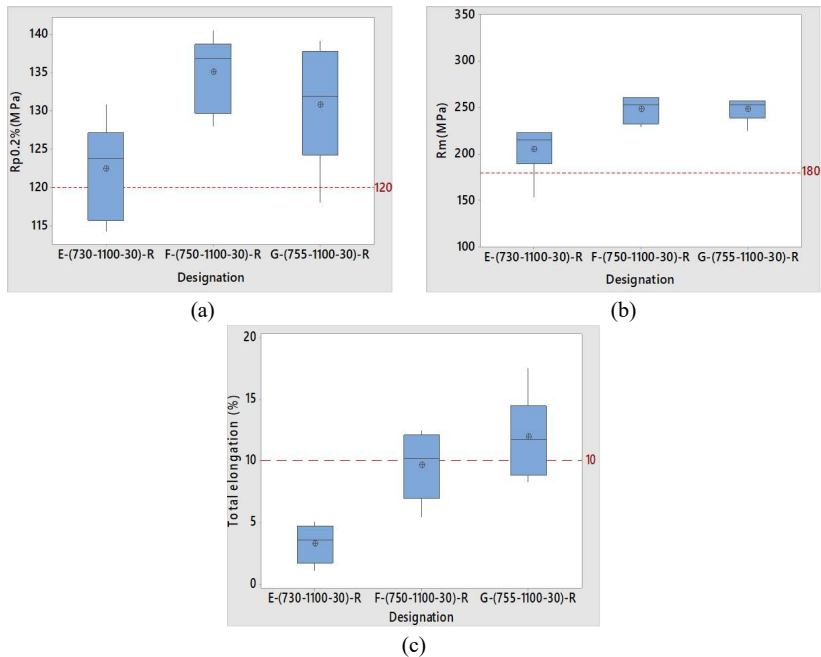


Figure 6.3: The comparison between the different RheoMetal™ alloys in terms of their (a) Rp0.2 values (MPa), (b) Rm values (MPa) and (c) total elongation values (%). (Designations from *Table 4.9, P65*)

6. The investigations regarding the RheoMetal™ process

The Rp0.2, the Rm and the total elongation values are illustrated in *Figure 6.3* for the RheoMetal™ alloys that were used at supplier 3. Similar to *Figure 6.2*, the respective mechanical requirements of the 2020 Ford explorer shock are also demonstrated in this figure and allude to values that are greater than those represented by the broken lines.

As shown in *Figure 6.3(a)*, the average yield strength values ($\bar{\sigma}$) of the three alloys were in line with the shock tower's requirement as they were higher than 120 MPa. Similar to the outcomes in *Figure 6.3(a)*, *Figure 6.3(b)* shows that the EN AB-42000 (E-730R-1100-30C), the AlMg4Fe2 (F-750R-1100-30C) and the MYFORD (G-755R-1100-30C) alloys were able to meet the ultimate tensile strength requirement of higher than 180 MPa.

Unlike the previous two charts, *Figure 6.3(c)* demonstrates that MYFORD (G-755R-1100-30C) was the only alloy whose average total elongation value was higher than 10%.

Intermediate conclusion:

- EN AB-42000 (E-730R-1100-30C) is not considered as a suitable RheoMetal™ alloy for the production of the 2020 Ford explorer shock tower. This conclusion was based on this alloy's inability to meet the total elongation requirement of more than 10%.
- The MYFORD (G-755R-1100-30C) and, to a smaller extent, AlMg4Fe2 (F-750R-1100-30C) were the only RheoMetal™ alloys able to meet the mechanical requirements of the 2020 Ford explorer shock tower. For this reason, it is considered suitable to use these alloys, in particular MYFORD, in the production of the shock tower.

6.3 The impacts of the RheoMetal™ alloys on the crash resistance potential of the casting

The main aim of this investigation was to determine which of the investigated alloys would lead to the highest crash resistance potential when used in the RheoMetal™ process. This aim was reached after following the test sequence in *Table 5.9*. The considered plates and parts in this test sequence were produced using the optimum or the defined process parameters in *section 6.1*.

Table 6.12: The test sequence for determining the impacts of RheoMetal™ alloys on the crash resistance potential of the casting.

Purpose of the investigation	Set of parameters (Designation) from <i>Table 4.5</i> or <i>Table 4.9</i>	Test method	Sample form	Total number of tested samples for each designation
(a) To determine and compare between the impacts of the different	A-(50-4.63-575-1000)-R			

6. The investigations regarding the RheoMetal™ process

Table 6.12 (continued.)

RheoMetal™ alloys on the crash resistance potential of the supplier 1 plates	B-(30-4.63-575-1000)-R	3-point bending test	The 3-point bending test samples in <i>Figure 4.27</i>	8 bending samples from 2 different plates
	C-(50-4.63-575-1000)-R			
	D-(50-4.63-575-1000)-R			
(b) To determine and compare between the impacts of the different RheoMetal™ alloys on the crash resistance potential of the supplier 3 parts	E-(730-30-1100)-R	3-point bending test	The 3-point bending test samples in <i>Figure 4.27</i>	8 bending samples from 2 different plates
	F-(750-30-1100)-R			
	G-(755-30-1100)-R			

The findings of the sub investigations, ((a) and (b)) in the above test sequence, are represented in *sections 6.3.1 and 6.3.2* as follows.

6.3.1 The impacts of the RheoMetal™ alloys on the crash resistance potential of the plates from supplier 1

The 3-point bending test results of the different RheoMetal™ casted plates at supplier 1 are represented in *Figure 6.4*. Unlike *section 5.3.1*, no simulation of the 3-point bending test was needed, as all the considered plates were casted at the same supplier and had the same thickness.

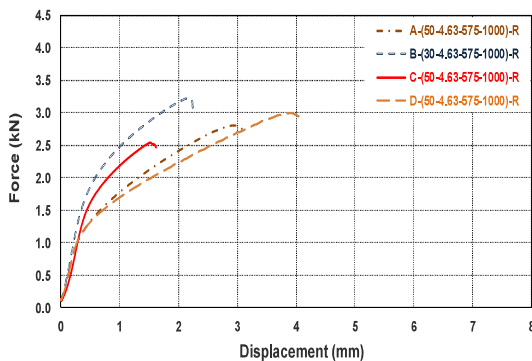


Figure 6.4: The force-displacement chart for the RheoMetal™ alloys that were used for the casting of the plates at supplier 1. (*Designations from Table 4.5, P58*)

6. The investigations regarding the RheoMetal™ process

As mentioned earlier in *section 5.3.1*, calculating the total area under each force-displacement curve made it possible to obtain the corresponding crash resistance behaviour. The energy-displacement curves for all the investigated alloys in this section are represented in *Figure 6.5* as follows.

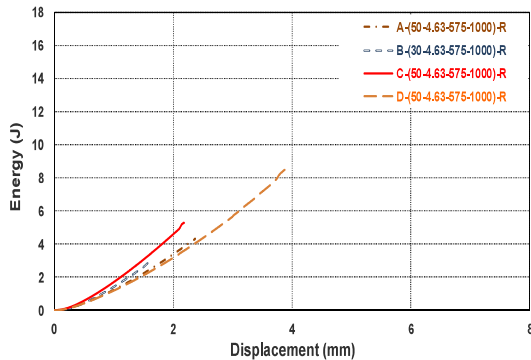


Figure 6.5: The energy-displacement chart for the RheoMetal™ alloys that were used for the casting of the plates at supplier 1. (*Designations from Table 4.5, P58*)

As seen in *Figure 6.5*, D-(50-4.63-575-1000)-R had the highest crash resistance potential. This outcome is similar to the finding in *section 5.3.1*. However, unlike the finding in *section 5.3.1*, the outcomes in *Figure 6.5* cannot be linked to the total elongation values of their respective alloys. This is because all of the considered alloys in *Figure 6.2* had, unlike their specifications, very low average total elongation values, which therefore indicates that the production of the plates by the RheoMetal™ process at supplier 1 was inefficient and that the outcomes from this process were not consistent nor reliable.

Intermediate conclusion:

- The crash resistance behaviour of the AlMg4Fe2 alloy (D-(50-4.63-575-1000)-R) was the highest among all the other alloys, which were considered for the production of the supplier 1 plates by the RheoMetal™ casting process.
- The above conclusion cannot be considered totally valid, due to the inefficiency of the RheoMetal™ process at supplier 1.

6.3.2 The impacts of the RheoMetal™ alloys on the crash resistance potential of the parts from supplier 3

Similar to *section 6.3.1* and in order to cover the whole range of alloys, it was also important to perform the crash resistance analysis on the alloys, which were chosen for the RheoMetal™

6. The investigations regarding the RheoMetal™ process

casting trials at supplier 3. The force-displacement and the energy-displacement curves of the investigated RheoMetal™ alloys are represented in *Figure 6.6* and *Figure 6.7* as follows.

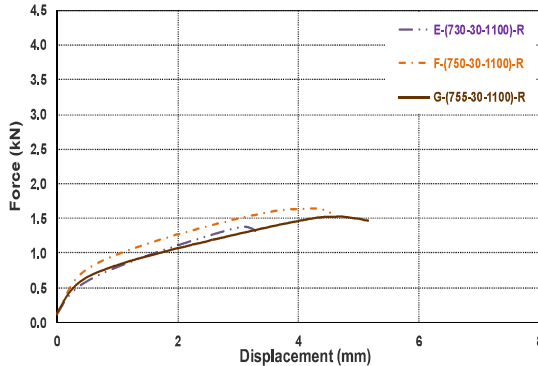


Figure 6.6: The force-displacement chart of the RheoMetal™ alloys that were used at supplier 3. (Designations from Table 4.9, P65)

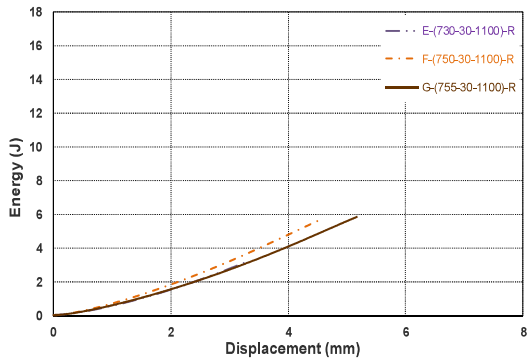


Figure 6.7: The energy-displacement chart of the RheoMetal™ alloys that were used at supplier 3. (Designations from Table 4.9, P65)

Figure 6.7 shows that the MYFORD alloy (G755R-100-30C) and the AlMg4Fe2 alloy (F750-1100-30C) led to better crash resistance behaviours than the EN AB-42000 alloy (E-(730-30-1100)-R), which is considered by supplier 3 to be the standard alloy for the RheoMetal™ casting process. In addition, comparing between MYFORD (G755R-100-30C) and AlMg4Fe2 (F750-1100-30C) illustrates that both alloys had similar impacts on the crash resistance potential of the casting. This is regardless of the slight difference in their energy absorption capabilities, which can be mainly contributed to the variation in the test results or to the small difference in their average total elongation values.

6. The investigations regarding the RheoMetal™ process

The above outcome can be linked to the total elongation values of the different alloys in *Figure 6.3*. This is because the alloys with the highest average total elongation values (MYFORD (G755R-100-30C) and AlMg4Fe2 (F750-1100-30C)) were the ones with the highest impacts on the crash resistance potential of the casting.

Intermediate conclusions:

- After analyzing *Figure 6.7*, it is concluded that MYFORD and AlMg4Fe2 would result in better crash resistance potentials than the EN AB-42000 alloy, and that both alloys would lead to similar impacts on the crash resistance potential of the casting.

6.4 The rivetability of the RheoMetal™ alloys

The outcomes of the SPR trials for the different RheoMetal™ alloys are represented in *sections 6.4.1* and *6.4.2*. These trials were conducted, according to the approach in *section 4.5.4*, for the purposes mentioned in *Table 6.13* as follows.

Table 6.13: The test sequence for determining the suitability of the RheoMetal™ alloys to the SPR joining method.

Purpose of the investigation	Set of parameters (Designation) from <i>Table 4.5</i> or <i>Table 4.9</i>	Test	Total number of joints for each test method
a) To determine the suitability of joining the RheoMetal™ plates from supplier 1 to 1.3 mm DP steel sheets using 36MnB4 rivets	A-(50-4.63-575-1000)-R	• SPR	<ul style="list-style-type: none"> • SPR: 3 joints for each rivet-die combination
	B-(30-4.63-575-1000)-R		
	C-(50-4.63-575-1000)-R		
	D-(50-4.63-575-1000)-R		
b) To compare between the joining behaviours of the MYFORD alloy, the EN AB-42000 alloy and the AlMg4Fe2 alloy	E-(730-30-1100)-R	• Lap shear	<ul style="list-style-type: none"> • Lap shear: 3 samples using the best rivet-die combination
	F-(750-30-1100)-R		
	G-(755-30-1100)-R		












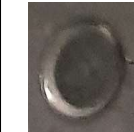




As shown in *Table 6.13*, all the considered plates and parts in this test sequence were produced using the optimum/defined process parameters in *section 6.1*.

6. The investigations regarding the RheoMetal™ process

6.4.1 The rivetability of the RheoMetal™ alloys that were used at supplier 1

The rivet-die combinations in *Table 4.10* were used for the production of the joints between the RheoMetal™ plates from supplier 1 and the DP steel sheets. The outer surfaces of these joints, which are represented in *Table 6.14*, were then evaluated to check if they were acceptable (✓), unacceptable (x) or borderline (o).

Table 6.14: The evaluation of the SPR joints on the plates from suppliers 1.

Set of parameters (Designation) from <i>Table 4.5</i>	Rivet-die combination from <i>Table 4.11</i>			
	1 st combination BG0542EHL0-EHG13209	2 nd combination BG0542EHL0-EHG13210	3 rd combination BG0542EHL0-EHG14034	4 th combination BG0E44EHL0-EHG14033
A-(50-4.63-575-1000)-R	X 	X 	X 	O 
B-(30-4.63-575-1000)-R	X 	X 	X 	X 
C-(50-4.63-575-1000)-R	X 	X 	X 	X 
D-(50-4.63-575-1000)-R	X 	O 	O 	✓ 

The evaluation of the joints in *Table 6.14*, which was carried out using the same criteria in *section 5.4.1*, showed that AlMg4Fe2 (D-(50-4.63-575-1000)-R) was the only alloy that could be joined to the DP steel sheet by the SRP method.

6. The investigations regarding the RheoMetal™ process

Only the 4th rivet-die combination was able to produce an acceptable joint for this alloy. However, as shown in *Table 6.14*, it was possible to produce borderline joints for the AlMg4Fe2 alloy (D-(50-4.63-575-1000)-R) using the 2nd and 3rd rivet-die combinations.

As previously done in *section 5.4.1*, three lap shear test samples were prepared for D-(50-4.63-575-1000)-R using the best rivet-die combination (4th). These samples were then tested for the purpose of deriving the energy absorption capabilities of their SPR joints.

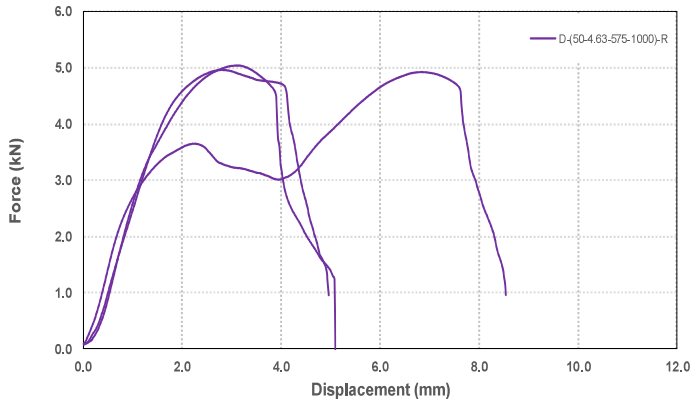


Figure 6.8: The force-displacement chart for D-(50-4.63-575-1000)-R. (*Designation from Table 4.5, P58*)

Like the results in *Figure 5.15*, a maximum shear force of 5kN was achieved by the SPR joint between AlMg4Fe2 (D-(50-4.63-575-1000)-R) and the DP steel sheet. However, and similar to the findings in *section 6.3.1*, the outcomes in *Table 6.14* and *Figure 6.8* are not reliable. This is because they cannot be linked to the total elongation values of the respective alloys in *Figure 6.2*, due to the inefficiency of the RheoMetal™ process at supplier 1.

Intermediate conclusion:

- Among all the RheoMetal™ alloys that were used for the plate casting trials at supplier 1, an acceptable joint could be only made for the AlMg4Fe2 alloy (D-(50-4.63-575-1000)-R).
- If the lap shear test samples were made using the 2nd rivet-die combination, the detected maximum shear force would be expected to be lower than 5 kN. This is due to the smaller mechanical interlock between the shorter rivet (BG0542EHL0) and the bottom sheet (90). Therefore, it is concluded that under the same joining condition, the energy absorption of the D-(50-4.63-575-1000)-R – DP steel joint is expected to be lower than that of the D-(3-650) – DP steel joint in *Figure 5.15*.











6. The investigations regarding the RheoMetal™ process

- As mentioned earlier, the above conclusions are not considered to be totally valid, due to the inefficiency of the RheoMetal™ process at supplier 1.

6.4.2 The rivetability of the RheoMetal™ alloys that were used at supplier 3

Similar to *section 5.4.2* and by using the parts produced at supplier 3, it was possible to conduct a comparison between the SPR joining behaviours of the MYFORD alloy (G-(755-30-1100)-R), EN AB-42000 (E-(730-30-1100)-R), which is the supplier's standard RheoMetal™ alloy, and the AlMg4Fe2 alloy (F-(750-30-1100)-R).

Table 6.15: The evaluation of the SPR joints on the parts from supplier 3.

Set of parameters (Designation) from <i>Table 4.9</i>	Rivet-die combination from <i>Table 4.11</i>			
	1 st combination BG0542EHL0- EHG13209	2 nd combination BG0542EHL0- EHG13210	3 rd combination BG0542EHL0- EHG14034	4 th combination BG0E44EHL0- EHG14033
E-(730-30-1100)- R	X	X 	X 	O 
F-(750-30-1100)- R	X	X 	√ 	√ 
G-(755-30-1100)- R	X 	√ 	√ 	√ 

As shown in *Table 6.15*, the joints made by the 2nd rivet-die combination were unacceptable for the EN AB-42000 alloy (E-(730-30-1100)-R) and the AlMg4Fe2 alloy (F-(750-30-1100)-R). Therefore, the 1st rivet-die combination was not used to produce SPR joints for these alloys.

On the other hand, the 1st rivet-die combination was implemented for the MYFORD alloy (G-(755-30-1100)-R), as it was possible to produce an acceptable joint for this alloy using the 2nd rivet-die combination.

6. The investigations regarding the RheoMetal™ process

The outcomes in *Table 5.12* can be linked to the total elongation values of the different alloys in *Figure 6.3*. This is because the alloy with the highest average total elongation value, MYFORD (G-(755-30-1100)-R), was the one with the best rivetability. In addition, the other alloys with lower average total elongation values, AlMg4Fe2 (F-(750-30-1100)-R) and EN AB-42000 (E-(730-30-1100)-R), had accordingly worse rivetability.

Intermediate conclusion:

- Among the investigated RheoMetal™ alloys, MYFORD (G-(755-30-1100)-R) is the alloy with the best rivetability and therefore the highest suitability to the SPR joining method. This conclusion was because, unlike the other RheoMetal™ alloys, it was possible to produce an acceptable SPR joint between the MYFORD alloy and the DP steel sheet using the deeper die of the 2nd rivet-die combination (EHG13210).

6.5 The optimization potential of the testing outcomes from the RheoMetal™ process trials at supplier 3

As the mechanical testing outcomes in *sections 6.2.2.2, 6.3.2 and 6.4.2* were reached by using *RheoMetal AB*'s recommended values of the %EEM, the rotation speed of the EEM and the melt superheat, and as there was no certainty that these values were the optimum ones for the production of the parts by the RheoMetal™ process at supplier 3, it was important to conduct additional investigations on the cast parts, as illustrated in *Table 6.16*, to identify whether there was a potential to optimize the recommended process parameters and thus the addressed mechanical testing outcomes or not.

Table 6.16: The test sequence for the determination of the optimum RheoMetal™ process parameters.

Purpose of the investigation	Set of parameters (Designation) from <i>Table 4.9</i>	Test methods	Total number of tested samples for each Set of parameters (Designation)
(a) Determining the optimum value of the melt superheat	E-(750-30-1100)-R*	Microstructural analysis	Microstructural analysis: 1 sample (gate side)
	E-(730-30-1100)-R		
(b) Determining the optimum %EEM	E-(730-40-1100)-R*		
	E-(730-30-1100)-R		
(c) Determining the optimum value of the rotation speed of the EEM	E-(730-30-1500)-R*		
	E-(730-30-1100)-R		

* Used exclusively for the determination of the process parameters' optimization potential.

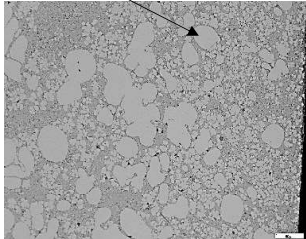
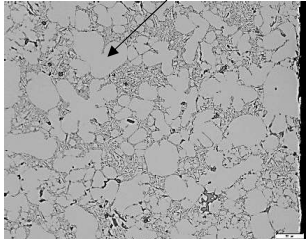
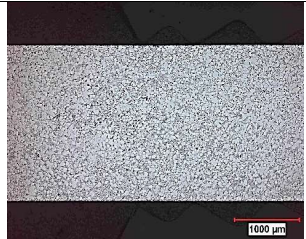

6. The investigations regarding the RheoMetal™ process

6.5.1 The optimum melt superheat

The effect of the melt superheat on the microstructures of the supplier 3 parts was studied in this section. The considered parts in this investigation were produced using the EN AB-42000 alloy at two different melt superheats.

The different melt superheats were 40°C, which was the standard value of the melt superheat according to *RheoMetal AB*, and 50°C.

Table 6.17: The influence of the melt superheat on the microstructures of the RheoMetal™ parts from supplier 3.

Magnification	Set of parameters (Designation) from Table 4.9	
	E-(750-30-1100)-R	E-(730-30-1100)-R
200x		
25x		

The visual evaluation of the 200x microstructural images in *Table 6.17* shows that an increase in the melt superheat from approximately 40 °C (E-(730-30-1100)-R) to approximately 50°C (E-(750-30-1100)-R) was the reason for the reduction in the α_1 -Al phase's size. This outcome is in accordance with the literature review in *section 2.4.3.3*.

However, unlike the findings in *section 6.1.1.3* and as seen in the 25x images, no major improvement in the feeding efficiency of the slurry was recorded near the gate side at the higher melt superheat.

6. The investigations regarding the RheoMetal™ process

Intermediate conclusions:

- Increasing the melt superheat led to a reduction in the size of the α_1 -Al phase.
- Changing the melt superheat had no visually detectable impact on the feeding efficiency of the semi-solid slurry close to the gate.
- Due to the above outcomes, it was concluded that the higher melt superheat of 50 °C would have resulted in better mechanical properties than the standard 40 °C.

6.5.2 The optimum %EEM

Similar to the previous section, the influence of the %EEM on the mechanical properties was investigated for the purpose of obtaining an optimum %EEM's value that can be used as a reference for the future trials.

The determination of the optimum %EEM involved analyzing the microstructures, which resembled the use of the following two %EEMs:

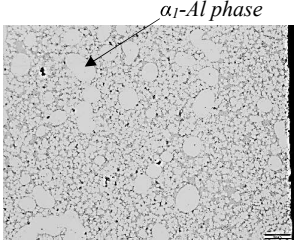
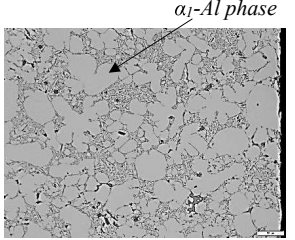
- A 5.6%EEM, which is the standard %EEM according to *RheoMetal AB*.
- A 7.3%EEM.

The exact heights of the investigated EEMs (h_{EEM}) were calculated using *equation (4.3)* in *section 4.3*. The inputs to this equation were the mass of the shot from *Table 4.9*, the %EEM, the density of the EN AB-42000 alloy from the supplier manual (3), the 3.5 cm EEM's radius (R) and the 1.2 cm rod's radius (r).

The resultant h_{EEM} for each %EEM were:

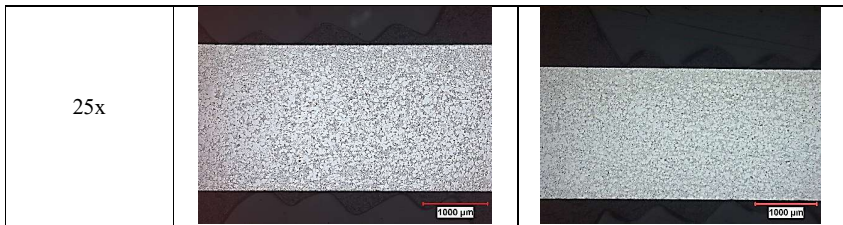
- h_{EEM} for 5.6%EEM = 30 cm
- h_{EEM} for 7.3%EEM = 40 cm

Table 6.18: The influence of the %EEM on the microstructures of the RheoMetal™ parts from supplier 3.

Magnification	Set of parameters (Designation) from <i>Table 4.9</i>	
	E-(730-40-1100)-R	E-(730-30-1100)-R
200x	 <p>α_1-Al phase</p>	 <p>α_1-Al phase</p>

6. The investigations regarding the RheoMetal™ process

Table 6.18 (continued.)



The visual analysis of the 200x images in *Table 6.18* shows that a decrease in the α_1 -Al phase's size was caused by increasing the %EEM from the standard 5.6% (E-(730-30-1100)-R) to 7.3% (E-(730-40-1100)-R). In addition, no major microstructural defects were visually detected in both of *Table 6.18*'s 25x images.

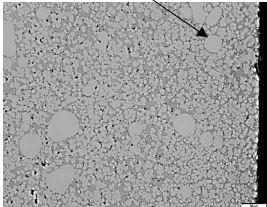
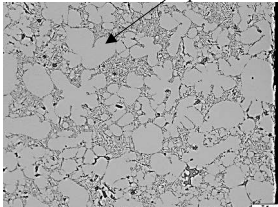
Intermediate conclusions:

- Increasing the %EEM led to a reduction in the size of the α_1 -Al phase.
- Changing the %EEM had no impact on the feeding efficiency of the semi-solid slurry close to the gate. This conclusion is based on the scarcity of defects in both of *Table 6.18*'s 25x images.
- Due to the above outcomes, it was concluded that the higher %EEM (7.3%) would have resulted in better mechanical properties than the standard 5.6 %.

6.5.3 The optimum rotation speed of the EEM

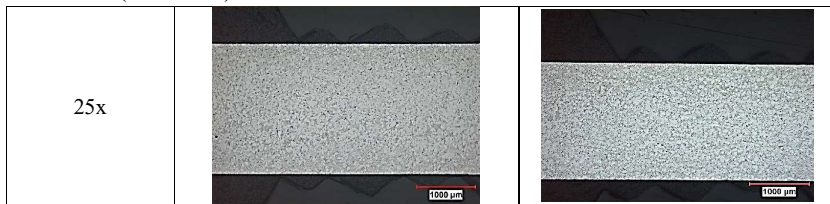
The impact of the EEM's rotation speed on the mechanical properties of the supplier 3 parts was studied in this section. This study was conducted by evaluating the microstructures of two parts, which were produced using the EN AB-42000 alloy at different EEM's rotation speeds.

Table 6.19: The influence of the rotation speed of the EEM on the microstructures of the RheoMetal™ parts from supplier 3.

Magnification	Set of parameters (Designation) from <i>Table 4.9</i>	
	E-(730-30-1500)-R	E-(730-30-1100)-R
200x	<p style="text-align: center;"><i>α_1-Al phase</i></p> 	<p style="text-align: center;"><i>α_1-Al phase</i></p> 

6. The investigations regarding the RheoMetal™ process

Table 6.19 (continued.)



The visual inspection of the 200x images in *Table 6.19* illustrates that by increasing the rotation speed of the EEM from 1100 rpm (E730-1100-3C), which was the standard rotation speed according to company *RheoMetal AB*, to 1500 rpm (E730-1500-30C), it was possible to cause a reduction in the size of the α_1 -Al phase.

In addition, the inspection of the 25x images shows that the feeding efficiency of the slurry close to the gate was high regardless of the applied EEM's rotation speed.

Intermediate conclusion:

- Increasing the EEM's rotation speed led to a reduction in the α_1 -Al phase's size.
- Changing the EEM's rotation speed had no impact on the feeding efficiency of the semi-solid slurry close to the gate.
- Due to the above outcomes, it was concluded that the higher EEM's rotation speed of 1500 rpm would have resulted in better mechanical properties than the standard 1100 rpm.

7. Discussion and conclusion

7 Discussion and conclusion

The detailed discussion of the test results from *chapters 5 and 6* was required for the purposes of determining the reasons beyond and the correlations between the detected outcomes, suggesting improvement possibilities for the future trials and finally reaching a conclusion about the cost-efficient process route for the mass production of thin walled structural aluminium body castings, such as the 2020 Ford explorer shock tower.

The discussion and the correlation between the test results was carried out in the following manner:

- Discussing and correlating between the outcomes of the HPDC trials.
- Discussing and correlating between the outcomes of the RheoMetal™ casting trials.
- Discussing the differences between the outcomes of the HPDC and the RheoMetal™ casting trials.

Each of the above points is addressed in a separate section as follows.

7.1 The HPDC trials

This section is focused about discussing the findings of the HPDC trials, which were conducted at suppliers 1, 2 and 3. A summary of the main investigations, their aims and the concluded findings are shown in *Table 7.1* as follows. In addition, an overview about the correlation between the different outcomes is illustrated in *section 7.1.1*.

Table 7.1: A summary of the HPDC trials' main investigations, aims and findings.

Investigation	Aim	Finding(s)
(a) Assessing the microstructures of the HPDC alloys and alloy-heat treatment combinations	<ul style="list-style-type: none"> ➤ To accurately characterize the different alloys and alloy-heat treatment combinations by determining the different phases in each of their microstructures ➤ To detect the microstructural defects in order to determine the suitability of the studied alloy-process parameters combinations to the HPDC process 	<ul style="list-style-type: none"> • Each of the investigated microstructures consisted of an α-Al phase, a eutectic and at least a single intermetallic phase • Cold flakes and shrinkage porosities were the detected defects in some of the investigated microstructures • Among the investigated alloys, AlMg5Si2Mn and AlMg6Si2MnZr were more prone to shrinkage porosities

7. Discussion and conclusion

Table 7.1 (continued.)

(b) Comparing between the mechanical testing outcomes of the different HPDC alloys and alloy-heat treatment combinations and correlating these outcomes to the mechanical requirements of the 2020 Ford explorer shock tower	To determine the possibility of producing the 2020 Ford explorer shock tower using the different HPDC alloys and alloy-heat treatment combinations	<ul style="list-style-type: none"> • Among the investigated HPDC alloys and alloy-heat combinations, MYFORD, AlMg4Fe2 and AlSi10MnMg-T7 were the ones able to fulfill the mechanical requirements of the 2020 Ford explorer shock tower
(c) Evaluating the impacts of the different HPDC alloys and alloy-heat treatment combinations on the crash resistance potential of the casting	To determine which of the investigated HPDC alloys and alloy-heat treatment combinations can lead to high crash resistance potentials that can enable their implementation in crash relevant parts, such as the 2020 Ford explorer shock tower	<ul style="list-style-type: none"> • MYFORD, AlMg4Fe2 and AlSi10MnMg-T7 resulted in much higher crash resistance potentials than the rest of the investigated HPDC alloys and alloy-heat treatment combinations • MYFORD led to higher crash resistance potential than AlMg4Fe2
(d) Evaluating the rivetability of the different HPDC alloys and alloy-heat treatment combinations	To determine the rivetability of the investigated HPDC alloys and alloy-heat treatment combinations by detecting the possible rivet-die combinations that can lead to acceptable joints between the aluminium castings and 1.3 mm DP600 steel sheets	<ul style="list-style-type: none"> • In comparison to the other investigated HPDC alloys and alloy-heat treatment combinations, it was possible to produce more acceptable SPR joints for MYFORD, AlMg4Fe2 and AlSi10MnMg-T7 • In comparison to AlMg4Fe2, more acceptable SPR joints were made using the MYFORD alloy

Determining and assessing the microstructural defects was important for a number of purposes, as shown in *Table 7.1*. The findings from this assessment are discussed in the following manner:

- The shrinkage porosities in *Figure 7.1* can be caused, according to *Table 2.2*, by a few factors other than the alloy composition. However, as all the other influencing factors were kept constant throughout the casting trials at supplier 1, the alloy composition is regarded to be the

7. Discussion and conclusion

main reason beyond the large volume of shrinkage porosities in the microstructures of AlMg5Si2Mn (B-(3.5-650)) and AlMg6Si2MnZr (C-(3.5-650)).

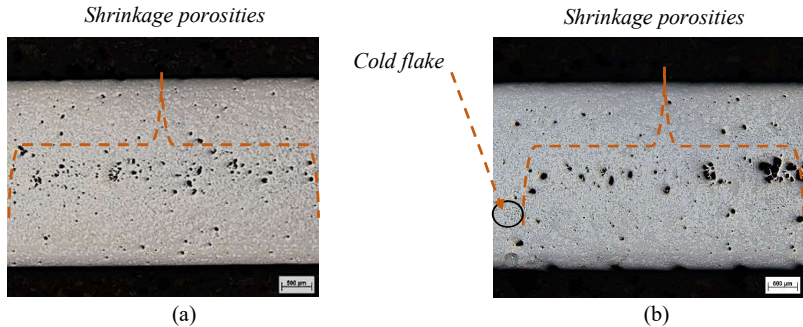


Figure 7.1: The shrinkage porosities in the microstructures of (a) AlMg5Si2Mn (B-(3.5-650)) and (b) AlMg6Si2MnZr (C-(3.5-650)). (Designations from Table 4.3, P54)

Although this common defect in the casting industry, shrinkage porosity, does have a deteriorating effect on the mechanical properties of the casting, it does not exclude the alloys with higher susceptibility to its evolution from being used in the production of structural body castings via the HPDC process. This is because its presence can be still decreased by several ways such as adjusting the process parameters, changing the gate design and by controlling the die temperature.

- From Table 2.2, gas porosities, gas blisters and shrinkage porosities are found to be the three main defects that may develop as a result of inadequately defining the process parameters (melt flow velocity and intensification pressure). The lack of the gas porosities and the gas blisters in the microstructures of the investigated HPDC alloys and alloy-heat treatment combinations, in addition to considering the alloy composition to be the main cause of the shrinkage porosities were the reasons that confirmed the suitability of the derived optimum process parameters in section 5.1 and the defined process parameters by supplier 2.
- Unlike the shrinkage porosities, the cold flakes cannot be linked to the alloy composition. Therefore, the presence of this filling related defect in some of the investigated microstructures implies that either a low shot sleeve temperature, a low filling level of the shot sleeve or a high level of melt's turbulence was occurred at the respective suppliers (1 and 2).

7.1.1 The correlation between the different outcomes

As seen in Table 7.2, the mechanical testing outcomes, the crash resistance potentials and the rivetability of the different HPDC alloys and alloy-heat treatment combinations are in line with

7. Discussion and conclusion

one another. This is because among all the investigated HPDC alloys and alloy-heat treatment combinations, AlSi10MnMg-T7, AlMg4Fe2 and the MYFORD were the ones fulfilling the mechanical requirements of the 2020 Ford explorer shock tower, resulting in the highest crash resistance potentials and having the best rivetability. This later conclusion about the rivetability was based on the exclusive ability of these alloys and alloy-heat treatment combinations to withstand the higher forming limits of the 1.5 mm deep die (EHG13210) during the SPR trials.

Table 7.2: The mechanical testing outcomes, the crash resistance potentials and the rivetability of the different HPDC alloys and alloy-heat treatment combinations. (Designations from Table 4.3 and Table 4.9)

Investigation	Finding			
	AlSi10MnMg-T7	AlMg4Fe2 Plate geometry (D-(3.5-650))	AlMg4Fe2 Part geometry (F-(740))	MYFORD (G-(755))
(a) The mechanical testing outcomes of the different HPDC alloys and alloy-heat treatment combinations				
(b) The crash resistance potentials of the different HPDC alloys and alloy-heat treatment combinations				
(c) The rivetability of the different HPDC alloys and alloy-heat treatment combinations	<p style="text-align: center;">The outcome of using a 1.5 mm deep die (EHG13210) in the SPR trials</p> <div style="display: flex; justify-content: space-around; align-items: center;"> <div style="text-align: center;"> </div> <div style="text-align: center;"> </div> <div style="text-align: center;"> </div> <div style="text-align: center;"> </div> </div>			

7. Discussion and conclusion

The outcomes in *Table 7.2* can be linked to the microstructural architectures of the investigated alloys and alloy-heat treatment combinations. For the three best performing alloys and alloy-heat treatment combinations in *Table 7.2*, a discussion of the microstructural features that contributed towards their enhanced properties, by offering less restriction to the dislocation movement during plastic deformation, is shown below.

- The following changes in the microstructure of the AlSi10MnMg alloy as a result of the T7 heat treatment are what mainly gives it an improved ductility in comparison to the other investigated alloys and alloy-heat treatment combinations (65) :
 - The reduction in the size and the spheroidization of the eutectic silicon, as visually estimated from *Figure 7.2*.

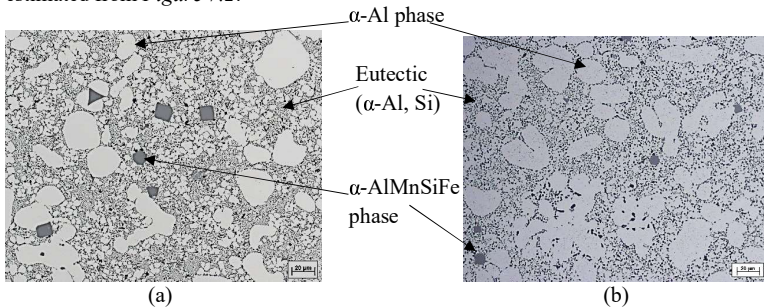


Figure 7.2: The 500x microstructural images of (a) AlSi10MnMg-F and (b) AlSi10MnMg-T7. (Designations from *Table 4.3, P54*)

- The expected increase in the size of the Mg_2Si precipitates in the α -Al phase (solid solution) as a result of overaging. This allows the dislocations to easily overcome them by looping (Orowan mechanism) instead of shearing as shown in *Figure 7.3*.

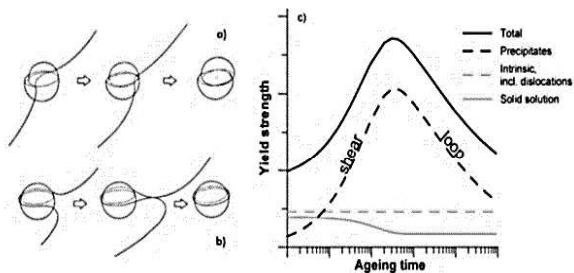


Figure 7.3: Dislocations overcoming a precipitate a) by shearing or b) by looping (Orowan mechanism) and c) the effect of the dislocations passing mechanism on the total yield strength of the alloy (65).

7. Discussion and conclusion

As shown in *Figure 7.3(c)* and as illustrated by the green arrows in *Figure 7.4(a)* and *Figure 7.4(c)*, the improvement in the ductility as a result of the T7 heat treatment is usually accompanied by a reduction in the yield strength value. However, as seen in *Figure 7.4(a)* and *Figure 7.4(b)*, this reduction is not critical, as the AlSi10MnMg-T7 alloy-heat treatment combination was still able to fulfil the yield strength requirement of the 2020 Ford explorer shock tower. The acceptable strength values (Rp0.2 and Rm) of this combination can be contributed to the low interlamellar spacing of its eutectic that restricts the dislocation slip and forces the plastic deformation in the Al-matrix to take place in the form of shear bands (95).

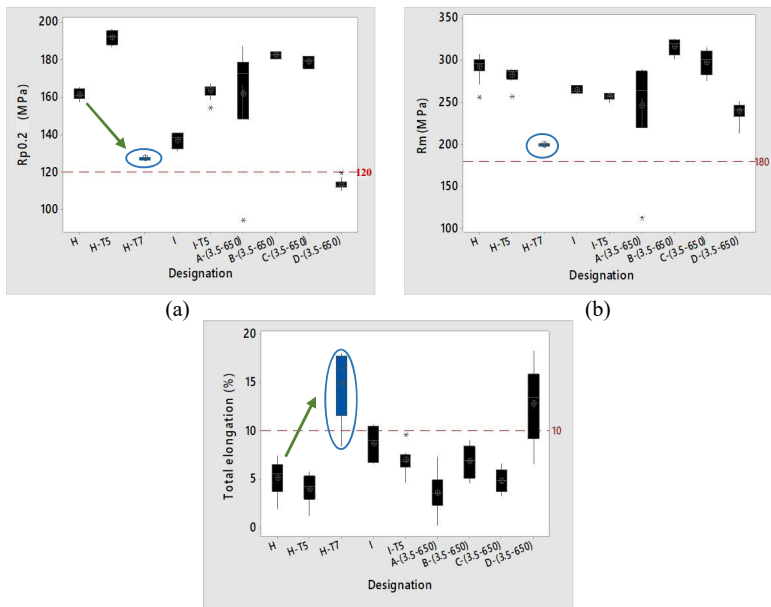


Figure 7.4: (a) The Rp0.2 values (MPa), (b) the Rm values (MPa) and (c) the total elongation values (%) of AlSi10MnMg-T7. (Designations from Table 4.3, P54)

- Unlike the AlSi10MnMg alloy, the AlMg4Fe2 alloy offers enhanced mechanical properties in the as-cast state. This cost-efficient alternative has a microstructure that consists of an α -Al phase, a primary β -Al₁₃Fe₄ intermetallic phase and a eutectic (α -Al, β -Al₁₃Fe₄). From *Figure 7.5*, it is obvious that the volume fraction of the eutectic in this alloy (α -Al, β -Al₁₃Fe₄) is smaller than its counterpart in the AlSi10MnMg alloy (α -Al, Si). This difference in the microstructures can be the reason beyond the higher ductility of the AlMg4Fe2 alloy, as there are less sites for crack initiation (96) and less restriction to the dislocation motion.

7. Discussion and conclusion

However, it should be stated that the long needle shaped morphology of the primary β - $\text{Al}_{13}\text{Fe}_4$ intermetallic phase (25-40 μm), which probably develops as a result of the slow cooling rate in the shot sleeve (59), can have a deteriorating impact on the ductility of the AlMg_4Fe_2 alloy.

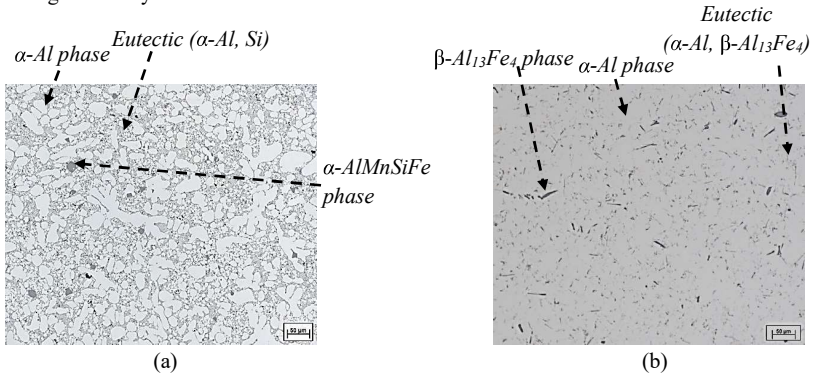


Figure 7.5: The 200x microstructural images of (a) AlSi10MnMg (H) and of (b) AlMg4Fe2 (D-(3-650)). (Designations from Table 4.3, P54)

- Further improvements to the standard AlMg4Fe2 alloy's ductility, impact on the crash resistance behaviour of the casting and rivetability were made possible through the development of the MYFORD alloy in section 4.4.1. The enhanced properties of this alloy, with the chemical composition in Table 4.8, can be mainly attributed to its lower iron content (59), which as seen in Figure 7.6, leads to the evolvement of smaller sized and more compact β - $\text{Al}_{13}\text{Fe}_4$ phase.

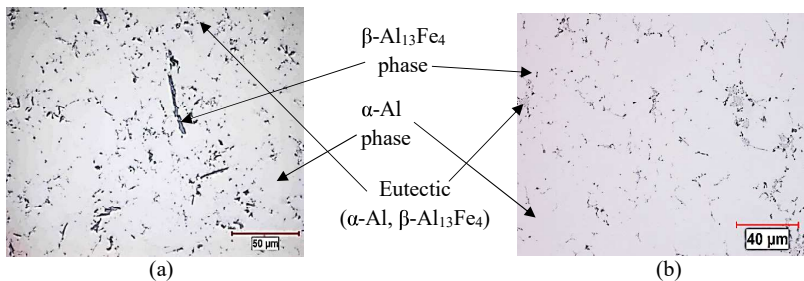


Figure 7.6: The 500x microstructural images of (a) AlMg4Fe2 (F-740C) and of (b) MYFORD (G-755C). (Designations from Table 4.9, P65)

7. Discussion and conclusion

7.2 The RheoMetal™ casting trials

In this section, the main findings of the RheoMetal™ casting trials, which were conducted at supplier 1 and 3, are analyzed and discussed. These findings in *Table 7.3* were derived after conducting the investigations in *Table 7.1* with the different RheoMetal™ alloys. In addition, an overview about the correlation between the different outcomes is illustrated in *section 7.2.1*.

Table 7.3: A summary of the RheoMetal™ casting trials' main investigations, aims and findings.

Investigation and aim from <i>Table 7.1</i>	Findings
(a)	<ul style="list-style-type: none"> • Each of the alloys consisted of an α-Al phase, a eutectic and at least a single intermetallic phase • Either scarce or no defects were detected in the studied microstructures
(b)	<ul style="list-style-type: none"> • The RheoMetal™ trials at supplier 3 were better and more reliable than their counterparts at supplier 1. Therefore, all the conclusions about the RheoMetal™ alloys were based on the outcomes of the trials that were conducted at supplier 3. • AlMg4Fe2 and MYFORD were the only RheoMetal™ alloys able to fulfill the mechanical requirements of the 2020 Ford explorer shock tower
(c)	<ul style="list-style-type: none"> • AlMg4Fe2 and MYFORD led to significantly higher crash resistance potentials than the rest of the investigated RheoMetal™ alloys
(d)	<ul style="list-style-type: none"> • Among the investigated RheoMetal™ alloys, it was only possible to produce acceptable SPR joints for the AlMg4Fe2 and the MYFORD alloys • Unlike for the AlMg4Fe2 alloy, it was possible to produce an acceptable SPR joint for the MYFORD alloy using a 1.5 mm deep die (EHG13210)

The scarcity/lack of the microstructural defects in *Table 6.10* and *Table 6.11* assists in implying that the investigated alloy-process parameters combinations are suitable to the RheoMetal™ casting process. Furthermore, the lack of the gas porosities indicates that the flow of the thixotropic slurries during the different RheoMetal™ casting trials was laminar.

By analyzing the results in *Figure 7.7*, none of the alloys at supplier 1 were found to be able to meet the total elongation requirement of the 2020 Ford explorer shock tower (10%). This includes the AlMg4Fe2 alloy (D-(50-4.63-575-1000)-R), which, as shown later in *Table 7.5(a)*,

7. Discussion and conclusion

was able to deliver a better performance when it was used for the RheoMetal™ casting trials of the parts at supplier 3.

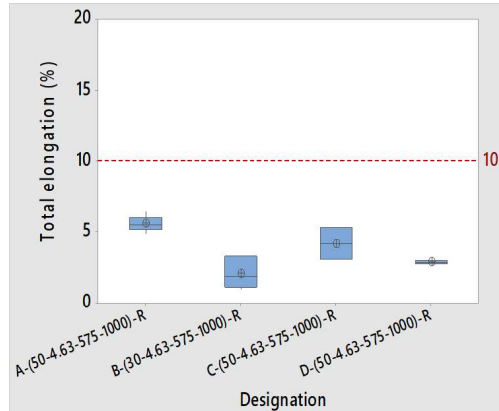


Figure 7.7: The total elongation (%) chart for the investigated RheoMetal™ alloys at supplier 1. (Designation from Table 4.5, P58)

The above finding can be related, as illustrated in Table 7.4, to the increase in the microstructural defects as a result of the low semi-solid slurry's feeding efficiency at supplier 1.

Table 7.4: The 25x microstructural images of the AlMg4Fe2 alloy from the suppliers 1 and 3. (Designations from Table 4.5 and Table 4.9)

Sample location	Supplier 1 (D-(50-4.63-575-1000)-R)	Supplier 3 (F-750R-1100-30C)
Near the gate	<p>Shrinkage porosities</p>	

The reduction in the feeding efficiency at supplier 1 can be contributed to the increase in the solid fraction of the slurry, which in turn can be caused by:

- i. The lower temperatures of the die and the shot sleeve at the beginning of each casting cycle, due to the long cycle time (46 seconds longer cycle time than at supplier 3).
- ii. The faster heat dissipation to the ladle walls, as a result of the small shot's volume.

7. Discussion and conclusion

7.2.1 The correlation between the different outcomes

Similar to *section 7.1.1* and as seen in *Table 7.5*, the mechanical testing outcomes, the crash resistance potentials and the rivetability of the different RheoMetal™ alloys are in line with one another. This is because among all the investigated RheoMetal™ alloys, MYFORD and AlMg4Fe2 were the ones fulfilling the mechanical requirements of the 2020 Ford explorer shock tower, resulting in the highest crash resistance potentials and having the best rivetability.

Table 7.5: The mechanical testing outcomes, the crash resistance potentials and the rivetability of the different RheoMetal™ alloys. (*Designations from Table 4.9*)

Investigations	Finding	
	AlMg4Fe2 F-(750-30-1100)-R	MYFORD G-(755-30-1100)-R
(a) The mechanical testing outcomes of the different RheoMetal™ alloys	<p>Box plot showing Total elongation (%) for three RheoMetal alloys. The y-axis ranges from 0 to 20%. A red dashed line indicates a 10% requirement. Alloy E-(730-1100-30)-R (black) has a median around 3.5%. Alloy F-(750-1100-30)-R (orange) has a median around 10%. Alloy G-(755-1100-30)-R (green) has a median around 12.5%.</p>	
(b) The crash resistance potentials of the different RheoMetal™ alloys	<p>Line graph showing Energy (J) vs Displacement (mm) for three RheoMetal alloys. The y-axis ranges from 0 to 18 J, and the x-axis ranges from 0 to 8 mm. Alloy E-(730-30-1100)-R (black dashed line) shows the lowest energy absorption. Alloy F-(750-30-1100)-R (orange dashed line) shows intermediate energy absorption. Alloy G-(755-30-1100)-R (green solid line) shows the highest energy absorption.</p>	
(c) The rivetability of the different RheoMetal™ alloys	<p>The outcome of using a 1.5 mm deep die (EHG13210) in the SPR trials</p> <div style="display: flex; justify-content: space-around;"> <div style="text-align: center;"> <p>X</p> </div> <div style="text-align: center;"> <p>✓</p> </div> </div>	

7. Discussion and conclusion

The positive investigations' outcomes in *Table 7.5* for the AlMg4Fe2 alloy and the MYFORD alloy can be linked to their as-cast microstructures. These microstructures, with low combined volume fractions of the eutectic and the β -Al₁₃Fe₄ intermetallic phase, assist in offering higher total elongation values than the standard RheoMetal™ alloy at supplier 3 (EN AB-42000) by minimizing the restrictions to the dislocation movement.

Both alloys (AlMg4Fe2 and MYFORD) had similar impacts on the crash resistance potential of the casting. However, MYFORD had a better rivetability. This later outcome can be traced back to the lower iron content of the MYFORD alloy, which, as shown in *Figure 7.8*, results in the development of smaller sized and more compact β -Al₁₃Fe₄ phase.

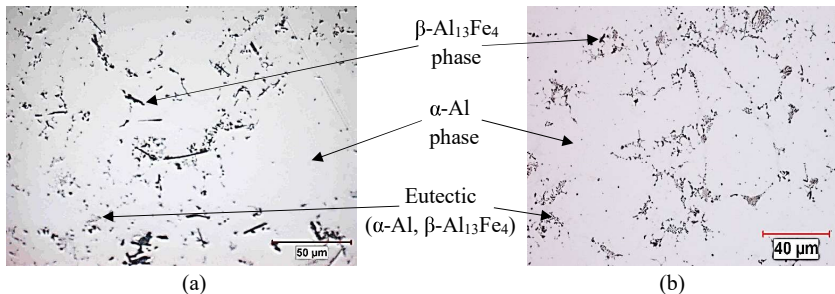


Figure 7.8: The 500x microstructural images of (a) the AlMg4Fe2 alloy (F-750R-1100-30C) and of (b) the MYFORD alloy (G-755R-1100-30C). (*Designations from Table 4.9, P65*)

7.3 The comparison between the outcomes of the HPDC and the RheoMetal™ casting trials

Choosing the RheoMetal™ process as a possible candidate for the cost-efficient mass production of the structural body parts was based, as discussed earlier in *section 2.4*, on its positive influence on the mechanical properties and, as illustrated in *section 3.2*, on its cost reduction potential in comparison to the standard HPDC process.

By analyzing the findings in *Table 7.1* and *Table 7.3*, MYFORD and, to a lesser extent, AlMg4Fe2 were found to be the best performing cost-efficient alloys .

Although the above alloys were successfully implemented in the RheoMetal™ process as well as in the HPDC process, it was still important to compare between their outcomes in both casting processes for the sake of determining which casting process better serves the purpose of this thesis. Due to reduced efficiency of the RheoMetal™ casting trials at supplier 1, this comparison between the casting processes only involved the results of the investigations that were performed on the supplier 3 parts.

7. Discussion and conclusion

The main findings of this comparison were that the parts produced by the RheoMetal™ process had similar mechanical properties to their HPDC-produced counterparts. In addition, they were similarly rivetable. However, by comparing between the findings in *Figure 7.9*, it is obvious that the RheoMetal™ parts, showed either similar or lower crash resistance potentials than their HPDC counterparts, as in the case of the MYFORD alloy ((G-(755-30-1100)-R) & (G-(755)).

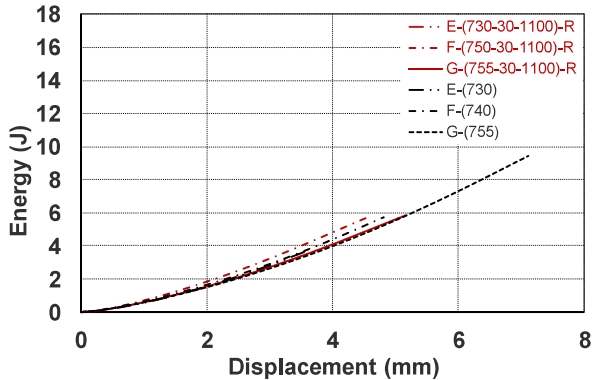


Figure 7.9: The crash resistance potentials of the RheoMetal™ parts (red) and the parts produced by HPDC (black).

These finding contradict the initial assumption in *section 2.4*, which states that the RheoMetal™ process can lead to better mechanical properties than the HPDC process due to the laminar flow of its thixotropic slurry and due to the smaller size and globular morphology of its primary α -Al phase. This contradiction can be associated with the chosen process parameters for the RheoMetal™ casting trials at supplier 3.

As stated earlier in *sections 6.5.1*, *6.5.2* and *6.5.3*, the implementation of the derived optimum process parameters instead of the values provided by supplier 3 is expected to improve the quality and the mechanical properties of the RheoMetal™-casted parts through the reduction in the size of the primary globular α -Al phase.

7.4 Conclusion

As mentioned earlier at the beginning of *chapter 7*, analyzing and discussing the testing outcomes of the investigated alloys, alloy-heat treatment combinations and casting processes were important steps toward reaching a conclusion about the cost-efficient process route for the mass production of the 2020 Ford explorer shock tower, which is the considered thin walled structural aluminium body casting in this thesis.

7. Discussion and conclusion

The general outcome of this thesis was the ability of a number of different alloys and alloy heat treatment combinations to meet the mechanical, SPR joining and crash resistance requirements of the investigated 2020 Ford explorer shock tower.

Upon all the considered HPDC alloys and alloy-heat treatment combinations, AlMg4Fe2 and MYFORD, together with the currently implemented AlSi10MnMg-T7, were the ones able to fulfill the above-mentioned requirements of the shock tower. By comparing between their testing outcomes, AlSi10MnMg-T7 and MYFORD were found to be better performing than the AlMg4Fe2 alloy. However, by comparing between them in terms of their impact on the cost efficiency of the cast part, AlMg4Fe2 and MYFORD were found to be the more cost-efficient alloys due to their excellent as-cast properties that enables their use for the 2020 Ford explorer shock tower without the need for a further heat treatment process. On the other hand, and in respect to their suitability to the RheoMetal™ casting process, the MYFORD alloy was found to be the most suitable.

From the above analysis, it can be concluded that among all the investigated alloys, the MYFORD alloy is regarded to be the most suitable choice for fulfilling the aim of mass producing the 2020 Ford explorer shock tower in a cost-efficient way. This conclusion is based on its ability, when used in conjunction with the HPDC process, to deliver a comparable performance to that of the currently implemented AlSi10MnMg-T7, in terms of the mechanical properties, rivetability and crash resistance potential of the casting, but without the need for a further heat treatment process. In addition, and unlike the AlSi10MnMg alloy, it can be also implemented in the RheoMetal™ process, which can lead to a further reduction in the cost of the part due to its positive impact on the die life.

As it was possible to produce the supplier 3 parts using both casting processes and using the MYFORD alloy, the following additional conclusions could be drawn:

- Due to its better influence on the crash resistance potential, the HPDC process is currently considered to be more suitable than the RheoMetal™ process for the cost-efficient mass production of crash resistant thin walled structural body parts, such as the 2020 Ford explorer shock tower.
- If the crash resistance potential of the structural body castings, which are produced by the RheoMetal™ process, could be improved to reach the level provided by the HPDC process, then it would be acceptable to consider the RheoMetal™ process as the cost-efficient alternative for the mass production of the castings.
- The outcome of the RheoMetal™ process can be improved if it is implemented in the production of thicker and smaller parts, as these parts offer less restriction to the flow of the thixotropic slurry.

8 Summary and outlook

8.1 Summary

The urge for a continuous reduction in the CO₂ emissions was and still is a driving force towards developing lighter vehicles with better fuel economy.

One of the suggested solutions to facilitate the reduction in the weight of the vehicles was the production of its thin walled structural body parts from aluminium castings instead of the heavier steel sheets. A disadvantage of this functionally integrated suggestion was the resultant higher structural body part's cost, which mainly stems from the more expensive raw material price of the chosen aluminium alloy. Therefore, the aim of this thesis was to investigate the possibility to cost-efficiently mass-produce a thin walled aluminium structural body casting, such as the 2020 Ford explorer shock tower.

The first step towards achieving the thesis' aim involved conducting a detailed cost calculation study to investigate the effects of the HPDC machine's type, the alloy and its heat treatment requirement, the vacuum condition and the die life on the cost of the 2020 Ford explorer shock tower. The outcomes from this study revealed that finding a suitable alloy or alloys, which is/are capable of delivering the mechanical and joining requirements of the structural body casting in the as-cast state, would play a major role in reducing the structural body casting's cost. In addition, determining a suitable mean for improving the die life (e.g. the RheoMetal™ process) was considered to positively influence the cost reduction.

Based on the above observations, different aluminium alloys that do not require heat treatment such as AlMg5Si2Mn, AlMg6Si2MnZr and AlMg4Fe2 were used at different suppliers to produce plates and or parts via the HPDC and the RheoMetal™ processes. The testing outcomes from these casted plates and parts, which in most cases were produced using the optimum derived process parameters, were then compared to the respective outcomes of the T7 heat treated AlSi10MnMg alloy, which is the currently implemented HPDC alloy-heat treatment combination for the 2020 Ford explorer shock tower.

Due to its solidification sequence, where the β -Al₁₃Fe₄ phase develops prior to the α -Al phase, the AlMg4Fe2 alloy was expected to have a low feeding efficiency and a low suitability to the RheoMetal™ casting process. Therefore, a new alloy (MYFORD), with the same chemical composition as that of the standard AlMg4Fe2 alloy but with lower iron and higher aluminium contents, had to be developed to help tackle these negative issues by changing the solidification sequence and by resulting in smaller sized and more compact β -Al₁₃Fe₄ phase. Like most of the other investigated alloys, this MYFORD alloy was implemented for the HPDC and the RheoMetal™ casting trials and its outcomes were compared to that of the currently implemented alloy-heat treatment combination (AlSi10MnMg-T7).

8. Summary and outlook

In addition to the mechanical testing results, determining the impacts of the alloy-heat treatment-casting process combinations on the crash resistance potential and the rivetability of the cast part were additional criteria for accurately evaluating the different alloys and the casting processes.

The above investigations had revealed that among all the considered alloys, the MYFORD alloy is regarded to be the most suitable choice for fulfilling the aim of the cost-efficient mass production of the 2020 Ford explorer shock tower. This conclusion is based on its ability, when used in conjunction with the HPDC process, to deliver a comparable performance to that of the currently implemented AlSi10MnMg-T7 in terms of the mechanical properties, rivetability and crash resistance potential of the casting, but without the need for a further heat treatment process. In addition, and unlike the AlSi10MnMg alloy, the MYFORD alloy can be also implemented in the RheoMetal™ process, which can cause an additional reduction in the cost of the part due to its positive impact on the die life.

Furthermore, and as it led to a better crash resistance potential of the casting when it was used in conjunction with the MYFORD alloy, the HPDC process is found to be more suitable than the RheoMetal™ process for the production of the thin walled structural body parts. This outcome can be contributed to the less restricted flow of the liquid melt in comparison to the RheoMetal™ process' thixotropic slurry. Moreover, due to the previous finding, the RheoMetal™ process can be expected to fulfill its full range of advantages if used in the production of thicker and smaller parts.

8.2 Outlook

This section will be concerned about highlighting the different approaches that could be considered in the future to:

- a. Further improve the resultant testing outcomes of the MYFORD alloy.

Although MYFORD was the best performing alloy in this thesis, its performance can still be further enhanced via:

- i. The addition of grain refiners such as Al-5Ti-1B to the melt before casting. This approach can lead to an additional enhancement in the properties of the alloy by reducing its α -Al phase's size and increasing the scattering of the intermetallic phases and the micro porosities (37).
- ii. The increase in the cooling rate of the melt, which can improve the mechanical properties by favoring the development of smaller sized α -Al phase, smaller dendritic arm spacing (DAS) and smaller intermetallic phases (97).
- iii. The Elimination or the change in the morphology of the β -Al₁₃Fe₄ intermetallic phase to a less detrimental α morphology through the addition of Manganese, such that the Mn/Fe ratio is ≥ 0.5 (59).

8. Summary and outlook

- b. Further reduce the cost of the structural body part.

From the outcome of the cost study in *section 3.1*, it is concluded that extending the die life could lead to supplementary cost reduction. Among the different suggestions that can influence the die life positively are:

- i. The application of the minimal quantity lubrication technology on the HPDC steel dies. This approach, which requires a much smaller volume of lubricants, can extend the die life by decreasing the thermal shock (98).
 - ii. The reinforcement of the HPDC steel dies by e.g. Fe(TiMo)C master-alloy, to improve their resistance against the thermal fatigue cracking (99).
- c. Improve the evaluation criteria of the different alloy-heat treatment-casting process combinations.

As the chemical composition of the aluminium alloys and the morphology of their phases can influence their susceptibility to corrosion (100), it is important to subject the different alloy-heat treatment-casting process combinations to corrosion testing. This critical step, which was not carried out in this thesis, can increase the accuracy of defining the suitable alloys and casting processes for the cost-efficient mass production of the thin walled structural aluminium body castings.

9. List of symbols

9 List of symbols

A.....	Total elongation
Rp0.2.....	Yield strength
Rm.....	Ultimate tensile strength
F.....	As-Cast
α_1 -Al phase.....	Primary globular α -Al phase
α_2 -Al phase.....	Fine dendritic α -Al phase
SPR.....	Self-piercing riveting
HPDC.....	High pressure die casting
EEM.....	Enthalpy exchange material
%EEM.....	Added EEM amount
h _{EEM}	Height of the EEM
Supplier 1.....	The Foundry Institute (GI) of the RWTH Aachen University
Supplier 2.....	Magna BDW technologies Soest GmbH
Supplier 3.....	Comptech AB
e.g.....	For example

The different alloy designations are defined in *Table 4.3*, *Table 4.5* and *Table 4.9*.

10 References

1. **Rio Tinto.** Aluminium: Your guide to automotive innovation. [Online] 2019. [Cited: November 11, 2019.] https://www.riotinto.com/documents/Aluminium_Automotive_innovation_brochure.pdf.
2. **Aluminium Rheinfelden GmbH.** Handbook- Primary aluminum casting alloys. [Online] 2017. [Cited: September 12, 2019.] http://rheinfelden-alloys.eu/wp-content/uploads/2017/12/LeporelloCastingAlloys_12-2017_Singular_pages.pdf.
3. **Stena Aluminium.** Aluminium alloy EN AB-42000. [Online] [Cited: October 30, 2019.] <https://www.stenaaluminium.com/siteassets/document/product-sheets/eng-en-ab-42000.pdf>.
4. **Verband der Automobilindustrie (VDA).** *VDA 238-100 : Plate bending test for metallic materials.* Berlin : VDA, 2010.
5. **International Organization for Standardization (ISO).** *ISO 6892-1. METALLIC MATERIALS - TENSILE TESTING - Part 1: Method of test at room temperature.* Geneva : ISO, 2016.
6. **Deutsches Institut für Normung (DIN).** *DIN 50125: Prüfung metallischer Werkstoffe-Zugproben.* Berlin : Beuth Verlag, 2016.
7. **Hoegh-Guldberg, O., et al.** Impacts of 1.5°C Global Warming on Natural and Human Systems. [book auth.] V. Masson-Delmotte, et al. *Global Warming of 1.5°C. An IPCC Special Report on the impacts of global warming of 1.5°C above pre-industrial levels and related global greenhouse gas emission pathways, in the context of strengthening the global response to the threat of climate change.* Geneva : The intergovernmental panel on climate change (ipcc), 2018.
8. **Yang, Z. and Bandivadekar, A.** 2017 Global update: Light-duty vehicle greenhouse gas and fuel economy standards. [Online] [Cited: May 29, 2018.] https://www.theicct.org/sites/default/files/publications/2017-Global-LDV-Standards-Update_ICCT-Report_23062017_vF.pdf.
9. **Ducker Worldwide LLC.** 2015 North American Light Vehicle Aluminum Content Study. [Online] 2014. [Cited: November 7, 2019.] <https://www.autonews.com/assets/PDF/CA95065611.PDF>.
10. **Goede, M., et al.** Super Light Car—lightweight construction thanks to a multi-material design and function integration. *European Transport Research Review.* 2009, Vol. 1, 1, pp. 5-10.
11. **NADCA Design.** Die Casting vs Metal Extrusion. [Online] NADCA Design. [Cited: November 11, 2019.] <https://www.diecastingdesign.org/metal-extrusions>.

10. References

12. **Yuksel, G., et al.** MMLV: NVH Sound Package Development and Full Vehicle testing, SAE Technical Paper 2015-01-1615. *SAE International*. 2015.
13. **European Aluminum Association.** The Aluminum Automotive manual, Manufacturing-casting methods. [Online] 2002. [Cited: May 23, 2019.] <https://www.european-aluminium.eu/media/1526/aam-manufacturing-1-casting-methods.pdf>.
14. **The American Foundry Society Technical Dept.** Aluminium Alloys. *Engineered casting solutions*. 2006, Vol. 8, 4, pp. 30-34.
15. **AZoM.** Aluminium Casting Techniques - Sand Casting and Die Casting Processes. [Online] 2002. [Cited: July 4, 2018.] <https://www.azom.com/article.aspx?ArticleID=1392>.
16. **Foundry Lexicon.** [Online] Foundry Lexicon. [Cited: April 24, 2019.] <https://www.giessereilexikon.com/en/foundry-lexicon/Encyclopedia>.
17. **Karban, Robert.** *The effects of intensification pressure, gate velocity, and intermediate shot velocity on the internal quality of aluminum die castings*. s.l. : Purdue University, PHD thesis, 2000.
18. **D. R. Gunasegaram, B. R. Finnin, F. B. Polivka.** Melt flow velocity in high pressure die casting: its effect of microstructure and mechanical properties in an Al-Si alloy. *Materials Science and Technology*. 2007, Vol. 23, 7, pp. 847-856.
19. **Herman, E.A.** *Gating Die Casting Dies*. Rosemont,IL : NADCA, 1996.
20. **Fiorese, E, et al.** Influence of injection parameters on the porosity and tensile properties of high-pressure die cast Al-Si alloys: A review. *International Journal of metalcasting*. 2015, Vol. 1, 9, pp. 43-53.
21. **Otarawanna, S., et al.** Feeding mechanisms in High-pressure die castings. *Metallurgical and Materials Transactions A*. 2010, Vol. 41, 7, pp. 1836-1846.
22. **Niu, X.P., et al.** Vacuum assisted high pressure die casting of aluminium alloys. *Journal of Materials Processing Technology*. 2000, Vol. 105, 1-2, pp. 119-127.
23. **SUN, S., Yuan, B. and Liu, M.** Effects of moulding sands and wall thickness on microstructure and mechanical properties of Sr-modified A356 Aluminum casting alloy. *Transactions of Nonferrous Metals Society of China*. 2012, Vol. 22, 8, pp. 1884-1890.
24. **Djurdjevic, M.B. and Grzincic, M.** The Effect of Major Alloying Elements on the size of secondary dendrite arm spacing in the As-cast Al-Si-Cu Alloys. *ARCHIVES of FOUNDARY ENGINEERING*. 2012, Vol. 12, 1, pp. 19-24.
25. **K. Radhakrishna and S. Seshan.** Dendritic arm spacing and mechanical properties of Aluminium Alloy castings. *Cast Metals*. 1989, Vol. 2, 1, pp. 34-38.

10. References

26. **Hartlieb, M.** High Integrity Die Casting: A Holistic Approach To Improved Die Casting Quality. [Online] [Cited: November 7, 2019.] <http://www.visi-trak.com/pdf/High%20Integrity%20Die%20Casting%20-%20iMdc%20Dec%202013.pdf>.
27. **Pasligh, Niels.** *Hybride formschlüssige Strukturverbindungen in Leichtbaustrukturen aus Stahlblech und Aluminiumdruckguss.* s.l. : Giesserei-Institut der RWTH Aachen, Dissertation, 2011.
28. **Ahamed, A. and Kato, H.** Influence of Casting Defects on Tensile properties of ADC12 Aluminum Alloy Die-Castings. *Materials Transactions.* 2008, Vol. 49, 7, pp. 1621-1628.
29. **Cao, X. and Campbell, J.** Oxide inclusion defects in Al-Si-Mg cast alloys. *Canadian Metallurgical Quarterly.* 2005, Vol. 44, 4, pp. 435-448.
30. **C.M.Gourlay and A.K.Dahle.** Dilatant shear bands in solidifying metals. *Nature.* 2007, Vol. 445, 7123, pp. 70-73.
31. **Ghosh, A.** Segregation in cast products. *SADHANA.* 2001, Vol. 26, 1-2, pp. 5-24.
32. **Midson, S.P. and Jackson, A.** A comparison of Thixocasting and Rheocasting. *67th World Foundry Congress (wfc06): Casting the Future.* Harrogate, UK : Institute of Cast Metals Engineers, 2006, pp. 1081-1090.
33. **Midson, S.P., Thornhill, L.E. and Young, K.** *Proc.5th Int. Conf. On Semi-Solid Processing of Alloys & Composites.* Golden, Colorado : Colorado School of Mines, 1998. p 181.
34. **Jolly, M.** Prof. John Campbell's Ten Rules for Making Reliable Castings. *JOM.* 2005, Vol. 57, 5, pp. 19-28.
35. **Nafisi, Shahrooz and Ghomashchi, Reza.** *Grain refining of conventional and semi-solid A356 Al-Si alloy.* s.l. : Journal of Materials Processing Technology, 2006. Vol 174 pp 371-383.
36. **Flemings, M.C.** Behaviour of metal alloys in the semi-solid state. *Metallurgical Transactions A.* 1991, Vol. 22, 5, pp. 957-981.
37. **McCartney, D.G.** Grain refining of aluminium and its alloys using inoculants. *International Material Reviews.* 1989, Vol. 13, 5, pp. 247-260.
38. **Pola, A, Toci, M and Kapronas, P.** Microstructure and properties of Semi-Solid Aluminum Alloys: A literature review. 2018, Vol. 8, 3, p. 181.
39. **Gerhard, H., et al.** Semi-solid Forming of Aluminium and Steel-Introduction and overview. [book auth.] H. Gerhard and R Kopp. *Thixoforming: Semi-Solid Metal Processing.* Weinheim : WILEY-VCH Verlag GmbH & Co. KGaA, 2009.

10. References

40. **Czerwinski, F.** The basics of modern semi-solid metal processing. *JOM*. 2006, Vol. 58, 6, pp. 17-20.
41. **Yurko, James A, Martinez, Raul A. and C.Flemmings, Merton.** The use of Semi Solid Rheocasting (SSR) for Aluminum automotive castings. s.l. : SAE paper 2003-01-0433., 2003.
42. **Fan, Z.** Semisolid metal processing. *International Materials Reviews*. 2002, Vol. 47, 2, pp. 49-85.
43. **Kirkwood, D. H., et al.** *Semi-Solid Processing of Alloys*. Berlin, Heidelberg : Springer, 2010.
44. **Modigell, M., Annalisa, P. and Marialaura, T.** Rheological Characterization of Semi-Solid Metals: A Review. *Metals*. 2018, Vol. 8, 4, pp. 245-268.
45. **Basner, T.** Rheocasting of semi solid A357 Aluminum, SAE paper :2000-01-0059. *SAE International*. 2000.
46. **Midson, S.P.** Rheocasting processes for Semi-Solid Casting of Aluminium Alloys. *Die Casting Engineer*. 2006, Vol. 1, pp. 48-51.
47. **C.P, Hong, and J.M, Kim.** Development of Advanced Rheocasting Process and its applications. *Solid State Phenomena*. 2006, Vols. 116-117, pp. 44-53.
48. **Patent: WO/2006/062, 482.** *A method of and a device for producing a liquid-solid metal composition*. Filing date: 2006, Inventors: Wessen, M; Cao, H.
49. **Payandeh, Mostafa.** *Rheocasting of Aluminium Alloys, Process and components characteristics*. Jönköping university, PhD thesis, 2016.
50. **H.Cao, M.Wessén & O.Granath.** Effect of injection velocity on porosity formation in Al rheocast component using Rheometal process. *International Journal of Cast Metals Research*. 2010, Vol. 23, 3, pp. 158-163.
51. **Lee, J., Seok, H. and Lee, H.** Effect of the Gate Geometry and the Injection Speed on the Flow. *Metals and Materials International*. 2003, Vol. 9, 4, pp. 351-357.
52. **O.Granath, M.Wessen and H.Cao.** Determining the effect of the slurry process parameters on semisolid A356 alloy microstructures produced by Rheometal process. *International Journal of Cast Metals Research*. 2008, Vol. 21, 5, pp. 349-356.
53. **Bladh, M., Wessen, M. and Dahle, A.K.** Shear band formation in shaped Rheocast Aluminium component at various plunger velocities. *Trans.Nonferrous Met. Soc. China*. 2010, Vol. 20, 9, pp. 1749-1755.

10. References

54. **Payandeh, M., Jarfors, A. and Wessen, M.** Influence of microstructural inhomogeneity on fracture behaviour in SSM-HPDC Al-Si-Cu-Fe component with low Si content. *Solid state phenomena*. Vols. 216-217, pp. 67-74.
55. **Zhu, Baiwei.** *On the influence of Si on Anodising and Mechanical properties of Cast Aluminium Alloys*. Jönköping University, Licentiate thesis, 2017.
56. **Hegde, S. and Prabhu, K.N.** Modification of eutectic silicon in Al-Si alloys. *Journal of Materials science*. 2008, Vol. 43, 9, pp. 3009-3027.
57. **Zhu, X., et al.** The effects of varying Mg and Si levels on the microstructural inhomogeneity and eutectic Mg₂Si morphology in die-cast Al-Mg-Si alloys. *Journal of Materials Science*. 2019, Vol. 54, 7, pp. 5773–5787.
58. **Yuan, W. and Liang, Z.** Effect of Zr addition on properties of Al-Mg-Si aluminum alloy used for all aluminium alloy conductor. *Materials and Design*. 2011, Vol. 32, 8, pp. 4195-4200.
59. **Ji, S., et al.** Effect of iron on the microstructure and mechanical property of Al-Mg-Si-Mn and Al-Mg-Si diecast alloys. *Materials Science and Engineering A*. 2013, Vol. 564, pp. 130-139.
60. **Hwang, J.Y., Doty, H.W. and Kaufman, M.J.** The effects of Mn additions on the microstructure and mechanical properties of Al-Si-Cu casting alloys. *Materials Science and Engineering A*. 2008, Vol. 488, 1-2, pp. 496-504.
61. **Murray, J.L. and McAlister, A.J.** Bulletin of Alloy Phase Diagrams. 1984, Vol. 5, 1, pp. 86-112.
62. **Zeru, G.T., Mose, B.R. and Mutuli, S.M.** The fluidity of a Model Recycle-Friendly Al-Si Casts Alloy for Automotive Engine Cylinder Head Application. *International Journal of Engineering Research & Technology (IJERT)*. 2014, Vol. 3, 8.
63. **Timelli, G. and Bonollo, F.** Fluidity of aluminium die casting alloys. *International Journal Of Cast Metals Research*. 2007, Vol. 20, 6, pp. 304-311.
64. **Gwózdź, M and Kwapisz, K.** *Influence of ageing process on the microstructure and mechanical properties of aluminium-silicon cast alloys - Al-9%Si-3%Cu and Al-9%Si-0.4%Mg*. s.l. : Jönköping University, Bachelor thesis, 2008.
65. **Mohamed, A.M.A. and Samuel, F.H.** A Review on the Heat Treatment of Al-Si-Cu/Mg Casting Alloys. *Heat treatment - Conventional and novel applications*. s.l. : IntechOpen, 2012, pp. 55-72.

10. References

66. **Katgerman, L and Eskin, D.** Hardening, annealing and aging. [book auth.] G.E Totten and D.S Mackenzie. *Handbook of Aluminum: Vol. 1: Physical Metallurgy and Processes*. New York : Marcel Dekker, Inc, 2003, pp. 269-271.
67. **Bühler AG.** Carat. The solution with highest value creation for sophisticated parts. [Online] 2018. [Cited: May 24, 2019.] http://www.buhlergroup.com/northamerica/en/downloads/Brochure_Carat_EN_2018.pdf.
68. **Tecnopres.** Hydraulic 4 columns Trimming presses. [Online] 2018. [Cited: May 24, 2019.] <https://www.tecnopres.it/wp-content/uploads/2018/06/caratteristiche-tecniche-presse-KZP.pdf>.
69. **KMA Umwelttechnik GmbH.** KMA press release GIFA 2007. [Online] 2007. [Cited: November 8, 2019.] <https://www.foundry-planet.com/fileadmin/redakteur/Material/KMAforGIFA2007.pdf>.
70. **STØTEK Inc.** Holding Furnace (STE) / (STET). [Online] STØTEK Inc. [Cited: July 27, 2018.] <http://stotek.com/our-products/ste-stet-holding-furnace/>.
71. **The London Metal Exchange.** LME Aluminum alloy. [Online] The London Metal Exchange, 2019. [Cited: January 24, 2019.] <https://www.lme.com/Metals/Non-ferrous/Aluminium-Alloy#tabIndex=2>.
72. **Kaufmann, H. and Uggowitzer, P.J.** *Metallurgy and Processing of High Integrity Light Metal Pressure Castings*. Berlin : SCHIELE & SCHÖN, 2014.
73. **Han, Q., Kenik, E.A. and Viswanathan, S.** Die soldering in aluminium die casting. *Office of Scientific & Technical Information Technical Reports*. 2000.
74. **Abdulhadi, H.A., et al.** Thermal Fatigue of Die-Casting Dies: An Overview. *MATEC Web of Conferences, ICMER 2015*. 2016, Vols. 74, 00032.
75. **Visi-trak worldwide, LLC.** High-Q-Cast. [Online] [Cited: July 23, 2018.] <http://www.visi-trak.com/Media/High-Q-Cast-NADCA-2011.pdf>.
76. **Midson, S.P., Minkler, R.B. and Brucher, H.G.** Gating of Semi-Solid Aluminum Castings. *Proc 6th Inter. Conf. on Semi-Solid Processing of Alloys and Composites*. Turin, Italy : s.n., 2000, pp. 67-71.
77. **Aluminium Rheinfelden GmbH.** Primary aluminum- HPDC alloys for Structural Casts in Vehicle Construction. [Online] 2017. [Cited: November 8, 2019.] http://rheinfelden-alloys.eu/wp-content/uploads/2018/01/Handbook-AI-HPDC-Alloys-for-Structural-Casts_RHEINFELDEN-ALLOYS_2017_EN.pdf.
78. **Gulliver, G.H.** The quantitative effect of rapid cooling upon the constitution of binary alloys. *J.Inst.Met.* 1909, Vol. 9, pp. 120-157.

10. References

79. **Scheil, E.** Comments on the layer crystal formation. *Z.Metallkd.* 1942, Vol. 34, pp. 70-72.
80. **ESAB.** ESAB knowledge center. [Online] ESAB. [Cited: May 24, 2019.] <http://www.esabna.com/us/en/education/blog/waterjet-cutting-process-basics.cfm>.
81. **Techni waterjet.** Waterjet advantages. [Online] Techni waterjet, 2018. [Cited: May 24, 2019.] <http://www.techniwaterjet.com/waterjet-advantages/>.
82. **SMU department of physics.** Mechanics laboratory manual - Archimedes' Principle and Buoyancy. [Online] SMU department of physics, 2002. [Cited: March 8, 2019.] <http://www.physics.smu.edu/~scalise/mechmanual/archimedes/lab.html>.
83. **Abbas, M., St.Pierre, G.R. and Mobley, C.E.** Microporosity of Air Cast and Vacuum Cast Aluminium Alloys. *AFS Transactions.* 1986, Vol. 49, pp. 47-56.
84. **He, X., Pearson, I. and Young, K.** Self-pierce riveting for sheet materials: State of the art. *Journal of Materials Processing Technology.* 2008, Vol. 199, 1-3, pp. 27-36.
85. **Li, D., et al.** Self-piercing riveting- a review. *The International Journal of Advanced Manufacturing Technology.* 2017, Vol. 92, 5-8, pp. 1777-1824.
86. **Atlas Copco Group.** Henrob self-pierce riveting. [Online] [Cited: August 6, 2019.] <https://www.atlascopco.com/content/dam/atlas-copco/industrial-technique/general/documents/brochures-leaflets/joining-solutions/henrob-self-pierce-riveting-intro-presentation.pdf>.
87. —. Henrob BG-Rivet. [Online] [Cited: August 7, 2019.] <https://www.atlascopco.com/content/dam/atlas-copco/industrial-technique/general/documents/brochures-leaflets/joining-solutions/bg-rivet-pdf.pdf>.
88. —. Henrob die catalogue. [Online] [Cited: November 8, 2019.] <https://www.atlascopco.com/content/dam/atlas-copco/industrial-technique/general/documents/brochures-leaflets/joining-solutions/henrob-die-catalog.pdf>.
89. **Stephens, E.V.** Mechanical strength of self-piercing riveting. [book auth.] A Chrysanthou and X Sun. *Self-Piercing Riveting: Properties, Processes and Applications.* s.l. : Woodhead Publishing Limited, 2014.
90. **Li, D, et al.** Influence of Die Profiles and Cracks on Joint Quality and Mechanical Strengths of High Strength Aluminium Alloy Joint. *Advanced Materials Research.* 2012, Vol. 548, pp. 398-405.
91. **SCG polymer solutions incorporated.** SEM Analysis | SEM-EDS Analysis. [Online] SCG polymer solutions incorporated. [Cited: March 20, 2019.] <https://www.polymersolutions.com/capabilities/scanning-electron-microscopy-with-energy-dispersive-spectroscopy/>.

10. References

92. **Encyclopaedia Britannica**. Spectrochemical analysis. [Online] Encyclopaedia Britannica. [Cited: January 22, 2019.] <https://www.britannica.com/science/spectrochemical-analysis>.
93. **OTARAWANNA, S. and DAHLE, A.K.** Casting of aluminium alloys. [book auth.] Roger Lumely. *Fundamentals of Aluminium Metallurgy: Production, Processing and Applications*. s.l. : Woodhead Publishing Limited, 2011.
94. **Porcaro, R., et al.** The behaviour of a self-piercing riveted connection under quasi-static loading conditions. *International Journal of solids and structures*. 2006, Vol. 43, 17, pp. 5110-5131.
95. **Park, J.M., et al.** High-strength bulk Al-based bimodal ultrafine eutectic composite with enhanced plasticity. *Journal of Materials Research*. 2009, Vol. 24, 8, pp. 2605-2609.
96. **Wang, Q.G., Caceres, C.H. and Griffiths, J.R.** Damage by Eutectic Particle Cracking in Aluminum Casting Alloys A356/357. *Metallurgical and Materials Transactions A*. 2003, Vol. 34, 12, pp. 2901-2912.
97. **Verma, A., et al.** Influence of cooling rate on the Fe intermetallic formation in an AA6063 Al alloy. *Journal of Alloys and Compounds*. 2013, Vol. 555, pp. 274-282.
98. **Bielomatik**. Minimal Quantity Lubrication (MQL) Systems in Metal Cutting. [Online] [Cited: October 25, 2019.] https://www.bielomatik.com/fileadmin/Dokumente/EN/Schmiersysteme/Brochure_MQL_EN_0316KL.pdf.
99. **Vicario, I., et al.** Development of high pressure die casting dies with internal refrigeration and sensors with reinforced cast steels. *International Journal of Manufacturing Engineering*. 2014, Vol. 2015, Article ID 287986, pp. 1-10.
100. **Kucharikova, L., et al.** Role of Chemical Composition in Corrosion of Aluminum Alloys. *Metals*. 2018, Vol. 8, 8, pp. 581-593.

11. Curriculum Vitae

11 Curriculum Vitae

Personal information

Name: Mohamed Youssef
Birth date/-place: 03.07.1990 in Cairo, Egypt
Nationality: Egyptian
Marital status: Single

Education

2011 – 2014 **RWTH Aachen university**, Master of Science in Metallurgical Engineering.
2006 – 2011 **German University in Cairo (GUC)**, Bachelor of Science in Material science and Engineering.
2004 – 2006 **IGCSE** (Cambridge International General Certificate of Secondary Education).

Work experience

10/2016–09/2019 **Ford Werke GmbH, Ford Research Centre Aachen**
Research Engineer in the Advanced Material and Processes Department and a PhD candidate at the Foundry Institute (GI) in Aachen.
11/2014-09/2016 **RLE Engineering and Services GmbH**
Material Engineer in the Metallic Materials Department, Product Development Europe, Ford Werke GmbH, Cologne, Germany
08/2013-04/2014 **SMS Meer GmbH, Mönchengladbach, Germany.**
Master thesis student.
05/2012-07/2013 **Institute of Physical Metallurgy and Metal Physics (IMM), RWTH Aachen university.**
Student assistant in the magnesium group.

Aachen, March 2021

12. Patent applications

12 Patent applications

[Patapp1] Patentanmeldung (DE): Amtliches Aktenzeichen 10 2019 125 679.8: *Verfahren zum Herstellen eines Bauteils*. Anmeldung: 2019, Erfinder: Youssef, M; Warkentin, M.

[Patapp2] Patentanmeldung (DE): Amtliches Aktenzeichen 10 2019 125 680.1: *Verfahren zum Herstellen eines Bauteils*. Anmeldung: 2019, Erfinder: Youssef, M; Warkentin, M.

Due to the harmful environmental and health impacts of the CO₂ emissions, new approaches have been suggested and implemented in the recent years to decrease their levels. One of these approaches is the reduction in the weight of the vehicles by replacing the thin walled structural body parts that are made up from steel sheets with ones made up from aluminium castings. This functionally integrated approach is regarded as being less economical due to the resultant higher part's cost, which in turn can be mainly linked to the more expensive aluminium alloy's price. Therefore, an aim for this thesis was set to try and look for ways that can facilitate the mass implementation of this approach in a cost-efficient way.

For this purpose, a cost calculation study was first conducted to determine the main influencing factors on the cost of a thin walled structural aluminium body part, such as the 2020 Ford explorer shock tower. These factors, mainly heat treatment and die life, were the reason beyond focusing the investigations on alloys with no heat treatment requirement, such as the Al-Mg-Si alloys and the Al-Mg-Fe alloys, and on casting processes that can prolong the die life, such as the RheoMetal™ process.

The evaluation criteria of the studied alloying systems and casting processes involved a series of mechanical testing, the determination of the cast parts' crash resistance potentials and a rivetability assessment using the self-piercing riveting method.

Among the investigated alloys, MYFORD, which was developed during the framework of this thesis to improve the feeding efficiency and the rheocastability of the standard AlMg4Fe2 alloy, appears to be the most suitable cost-efficient alloy to produce the thin walled structural body castings. In addition, the high pressure die casting process seems to be a more suitable candidate than the RheoMetal™ process to produce these castings. Furthermore, the outcomes from the RheoMetal™ process are expected to improve if it is implemented in the production of thicker and smaller parts.

Aufgrund der umwelt- und gesundheitsschädlichen Auswirkungen der CO₂ Emissionen wurden in den letzten Jahren neue Ansätze vorgeschlagen und umgesetzt, um deren Werte zu senken. Einer dieser Ansätze ist die Gewichtsreduzierung der Fahrzeuge durch die Substitution dünnwandiger Karosseriestrukturteile aus Stahlblechen durch solche aus Aluminiumguss. Dieser funktionell integrierte Ansatz, gilt aufgrund der daraus resultierenden höheren Bauteilkosten, die vor allem auf den teureren Rohstoffpreis der gewählten Aluminiumlegierung zurückzuführen sind, als weniger wirtschaftlich. Ziel dieser Arbeit war es daher, nach Möglichkeiten zu suchen, die eine kosteneffiziente Umsetzung dieses Ansatzes für die Großserie ermöglicht.

Zu diesem Zweck wurde zunächst eine Kostenstudie erstellt, um die Haupteinflussfaktoren auf die Gesamtbauteilkosten eines dünnwandigen Karosseriestrukturteils aus Aluminium, wie z. B. des 2020 Ford Explorer 2020 Federbeindoms, zu ermitteln. Diese Faktoren, u.a. die Wärmebehandlung und der Lebensdauer der Druckgussform, waren der Grund dafür, dass die Untersuchungen nicht nur auf Legierungen konzentrierte, die keine Wärmebehandlung erfordern, wie die Al-Mg-Si Legierungen und die Al-Mg-Fe Legierungen, sondern auch auf Gießverfahren, die der Lebensdauer der Druckgussform verlängern können, wie das RheoMetal™ Verfahren.

Die Bewertungskriterien der untersuchten Legierungssysteme und Gießverfahren umfassten eine Reihe von mechanischen Prüfungen, die Bestimmung des Crash-Widerstandspotenzials der Gussteile und eine Bewertung der Nietbarkeit mit dem Stanzniet Verfahren.

Unter den untersuchten Legierungen scheint die MYFORD Legierung, die im Rahmen dieser Arbeit entwickelt wurde, um die nachspeisung und die Gießbarkeit im Rheoverfahren der Standardlegierung AlMg4Fe2 zu verbessern, die am besten geeignete Legierung zu sein, um die dünnwandigen Strukturkörpergussteile kostengünstig herzustellen. Darüber hinaus scheint das Druckgussverfahren ein geeigneterer Kandidat als das RheoMetal™ Verfahren zu sein, um diese Gussteile herzustellen. Darüber hinaus kann aufgrund der bisherigen Erkenntnisse davon ausgegangen werden, dass das RheoMetal™ Verfahren bei der Herstellung von dickeren und kleineren Teilen seine volle Bandbreite an Vorteilen entfalten kann.